The Institution of Engineers of Kenya

In partnership with

ENGINEERS BOARD OF KENYA
—— *Enhancing Professionalism* ——

AJERI

African Journal of Engineering in Research and Innovation

IEK

CONTENTS   Pages

Recent Advances in Stress Analysis of Pressure Vessels: Enhancing Safety, Efficiency, and Reliability in Key Engineering Systems.

L. Masu[1], N. Kiplagat[2], and P. Nziu[3]

[1] Technical University of Kenya, Faculty of engineering and the built environment, School of Mechanical and manufacturing engineering, Department of Mechanical and Mechatronic Engineering, Haile Selassie Avenue, P.O. Box 52428, Nairobi, 00200, Tel +254(020) 343672, 2249974, 2251300, 341639, Nairobi, Kenya. ORCID: 0000-0002-8544-6321

[2] South Eastern Kenya University, School of Engineering, Mechanical and Manufacturing. P.O Box 170-90200, Kitui, KENYA. ORCID: 0000-0003-1203-645X

[3] Walter Sisulu University, Faculty of Engineering, Built Environment and Information Technology, Department of Mechanical Engineering. P. O. Box 1421, East London, 5200, South Africa. ORCID: 0000-0002-5899-0700

Abstract

Pressure vessels are critical components in various industrial applications, including power generation, petrochemical processing, and water systems, where structural integrity and safety are paramount. This paper presented a comprehensive review of stress analysis techniques applied to pressure vessels, examining the evolution from classical analytical methods to advanced numerical and data-driven approaches. Classical techniques, such as, simple stress calculations of thin cylinders and Lame's theory on thick cylinder stress analysis, laid the groundwork for early design and analysis but often fall short in addressing complex geometries and loading conditions. The advent of Finite Element Analysis (FEA) has significantly enhanced the ability to predict stress distributions accurately, particularly in geometrically complex regions such as nozzles and cross-bores. FEA has deployed computational tools like ANSYS, ABAQUS and other software for stress distribution analysis. The paper further explored experimental methods, including photelasticity, Digital Image Correlation (DIC) and strain measurement, which serve as critical tools for validating numerical models. In recent years, Artificial Intelligence (AI), Deep Learning (DL) and Machine Learning (ML) have emerged as transformative tools in fatigue life prediction, stress estimation, and condition monitoring of pressure vessels. Techniques such as Artificial Neural Networks (ANNs), Physics-Informed Neural Networks (PINNs), Bayesean framework, multistage crystal plasticity, and hybrid models integrating FEA and ML are increasingly being used to improve design optimization and predictive maintenance. The paper also highlighted the potential of Digital Twins (DTs), probabilistic modeling, and uncertainty quantification as future research directions. Emphasis is placed on the need for validation, standardization, and integration of AI-

driven predictive models with traditional methods. This review aimed to provide a foundational understanding of current capabilities and outline promising paths forward in the stress analysis and design of pressure vessels.

Keywords: Stress Analysis, Finite Element Analysis (FEA), Pressure Vessels, Artificial Intelligence (AI), Machine Learning (ML).

1. Introduction

Structures such as tanks, pipelines, and vessels that are designed to hold, transport, or receive fluids under pressure are known as pressure vessels (Khobragade & Hiwase, 2017). Moreover, these components are specifically engineered to contain gases or liquids at pressures higher than that of the surrounding atmosphere (Kadam et al., 2018). These vessels are tightly sealed and capable of storing significant amounts of energy due to the high temperatures and pressures of the contained fluids (Nziu & Masu, 2019a, 2019b). Therefore, it is essential to design pressure vessels to operate within safe working limits while withstanding the high pressures and temperatures they are subjected to (Digvijay & Jewargis, 2015). In the design of pressure vessels, a range of geometrical configurations may be used, with cylindrical and spherical shapes being the most common (Thattil & Pany, 2017). Cylindrical vessels, in particular, can be further categorized based on wall thickness as either thin-walled or thick-walled (Bahoum et al., 2017). A cylinder is typically classified as thick-walled when the internal pressure exceeds one-sixth of the material's allowable stress or when the wall thickness is greater than one-tenth of the vessel's internal radius (Phalguna, 2017). According to (Hyder & Asif, 2008), pressure vessels are essential components in engineering systems, designed to store or transport fluids under high pressure, and are widely utilized across various industries such as power generation, chemical processing, and fluid handling systems due to their ability to safely contain gases or liquids at pressures significantly higher than atmospheric levels.

Stress analysis in pressure vessels is the process of evaluating how various forces act on a vessel, particularly under conditions of high temperature, pressure, and external loads. Recent studies have demonstrated significant progress in the stress analysis of pressure vessels, particularly in enhancing safety, failure prevention, operational efficiency, and cost-effectiveness. Hazizi & Ghaleeh (2023) integrated ASME code-based calculations with Finite Element Analysis (FEA) to analyze vertical pressure vessels, confirming that such hybrid approaches ensure structural safety while optimizing design for material efficiency and reduced fabrication costs. Similarly, Che et al. (2023) developed a simulation-based method to assess strength and fatigue life in prestressed ultra-high-pressure vessels, highlighting how advanced modeling can extend service life and lower

maintenance demands. Asif Shaikh et al. (2024) provided a comprehensive review of ANSYS-based stress simulations, emphasizing their effectiveness in identifying high-stress regions and guiding design modifications that mitigate failure risks and improve reliability. Mutava et al. (2016) applied elastic and plastic stress analysis in thick-walled pressure vessels, showing how FEA can be used to define safety margins more accurately and support cost-effective material use. Further advancing this field, Jacobs et al. (2023) employed machine learning to predict steel embrittlement in reactor pressure vessels, allowing for improved lifecycle management and condition-based maintenance, which reduces the potential for unexpected failures and cuts long-term operational costs. Collectively, these studies underscore the critical role of modern stress analysis techniques in the design and maintenance of pressure vessels, ensuring that they meet the demanding requirements of contemporary engineering systems.

The purpose of this paper was to present recent advancements in stress analysis of pressure vessels, with a focus on enhancing safety, improving failure prevention, increasing operational efficiency, and minimizing design and maintenance costs. Through a review of current analytical, computational, and material innovations, this study aimed to demonstrate how modern stress analysis techniques contribute to the structural integrity and reliability of pressure vessels used across critical engineering systems such as power generation, chemical processing, and fluid transport. By consolidating these developments, the paper provided insight into how engineers can design more robust, cost-effective, and dependable pressure vessels for today's demanding applications.

2. Fundamentals of Stress Analysis in Pressure Vessels

As mentioned in the preceding section, there are two types of cylinders, mainly thin and thick cylinders. To be able to perform stress analysis in these cylinders it is important to understand some fundamental parameters and concepts. When a thin-walled cylindrical vessel is exposed to internal pressure, it experiences three orthogonal principal stresses within its material: circumferential (hoop) stress, longitudinal (axial) stress, and radial stress. Due to the thinness of the wall, it is generally acceptable to assume that both hoop and longitudinal stresses remain uniform throughout the thickness. In contrast, the radial stress is significantly lower in magnitude compared to the other two and is often considered negligible for analysis purposes (Hearn, 1997). Therefore, only two stresses are considered as shown in Figure 2.1.
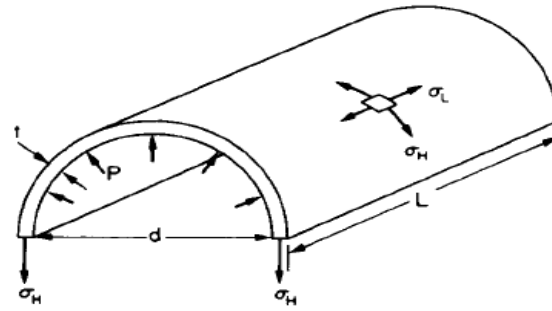
Figure 2.1 Stresses in thin cylindrical pressure vessel (Hearn, 1997)

According to Tawade (2019) the stress elements acting on the wall of a pressure vessel have faces that are oriented both perpendicular and parallel to the vessel's longitudinal axis. The normal stresses, denoted as σ_H and σ_L, act perpendicular and parallel to this axis, respectively. Due to the symmetrical geometry of the pressure vessel and the uniform internal pressure loading, shear stresses are absent on these faces. Consequently, σ_H and σ_L are classified as primary stresses. Specifically, σ_H is referred to as the hoop or circumferential stress, while σ_L is known as the axial or longitudinal stress (Hearn, 1997; Tawade, 2019). Therefore the formulas presented by Hearn (1997) are used:

Hoop stress $$\sigma_H = \frac{pd}{2t} \qquad (2.1)$$

Longitudinal stress $$\sigma_L = \frac{pd}{4t}$$

Where p is the internal pressure, d is the internal diameter of the cylinder and t is the thickness of the cylinder. Theses equations represent the simple stress analysis of thin cylinders.

In the theoretical analysis of thin-walled cylinders, it is typically assumed that the hoop stress remains uniform across the wall thickness and that the internal pressure does not vary through the thickness of the material. However, these assumptions are not applicable to thick-walled cylinders, where both hoop and radial stresses vary significantly throughout the wall, as shown in Figure 2.2.

Figure 2.2 Thick cylinder subjected to internal pressure (Hearn, 1997)

This variation is described mathematically using the Lame equations, which provide expressions for the distribution of these stresses in thick-walled pressure vessels.
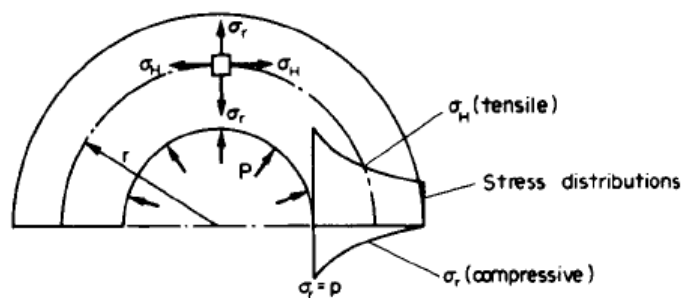
$$\sigma_H = A + \frac{B}{r^2} \tag{2.2}$$

$$\sigma_r = A - \frac{B}{r^2} \tag{2.3}$$

As presented by Hearn (1997) the radial and hoop stresses at any point within the wall of a thick-walled cylinder can be expressed in terms of two constants, A and B, using the derived equations. These constants are determined by applying two known boundary conditions—typically involving the radial stress at the internal and external surfaces of the cylinder. Once A and B are known, the stresses at any radius r within the wall can be calculated. For example, in the case of a thick cylinder subjected to internal pressure P with no external pressure, Hearn (1997) provides specific formulations to evaluate these stress components, as illustrated in Figure 2.3.
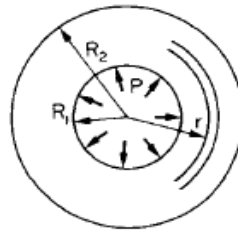
Figure 2.3 Cylinder cross-section

Bansal (2015) provides expressions for determining the hoop and radial stresses in thick-walled cylinders subjected to internal pressure. The hoop stress σ_H and radial stress σ_r at any radius r are given by:

$$Hoop\ stress, \sigma_H = \frac{PR_1{}^2}{R_2{}^2 - R_1{}^2}\left[1 + \frac{R_2{}^2}{r^2}\right] \tag{2.4}$$

$$Radial\ stress, \sigma_r = \frac{PR_1{}^2}{R_2{}^2 - R_1{}^2}\left[1 - \frac{R_2{}^2}{r^2}\right] \tag{2.5}$$

Here, R_1 and R_2 represent the internal and external radii of the cylinder, respectively. These equations describe how the hoop and radial stresses vary across the wall thickness, with both reaching their maximum values at the inner surface. The theory assumes that internal pressure is applied symmetrically, eliminating shear stresses on transverse planes. As a result, the hoop and radial stresses are treated as principal stresses under this loading condition.

Zhao et al. (2018) highlighted that the stress distribution within thick-walled cylinders and their ability to withstand elevated internal pressures can be substantially improved by introducing beneficial compressive residual stresses at the inner surface. This is often achieved through

autofrettage or by employing compound cylinder techniques, both of which are designed to increase the cylinder's load-bearing capacity. According to Das et al. (2024), autofrettage involves subjecting the cylinder to an internal pressure high enough to cause plastic deformation in its inner layers. When the pressure is removed, residual stresses are retained due to the permanent deformation, resulting in a compressive stress field near the internal radius and a tensile field in the outer regions. These residual stresses are beneficial, particularly in resisting fatigue failure under cyclic pressure loading. Supporting this, Ramy Abdelsalam & Sedaghati (2013) explain that the residual stress profile generated through autofrettage plays a crucial role in improving the fatigue life and overall structural integrity of pressure vessels. The mathematical representation of the tangential residual stress induced by autofrettage is provided by Koh (2000) in equation 2.6.

$$\sigma_\theta = \sigma_{ys} \left(1 + \frac{b^2}{r^2}\right) \left[\frac{\rho^2}{2b^2} + \frac{a^2}{b^2 - a^2} \left\{\frac{\rho^2 - b^2}{2b^2} - ln\, ln\, \frac{\rho}{a}\right\}\right], for\ \rho \leq r \leq b$$

$$(2.6)$$

Where a and b are inside radius and outside radius of the pressure vessel, while σ_{ys} is the yield stress of the pressure vessel and r, ρ are radius and elastic-plastic boundary of the autofrettaged pressure vessel respectively.

Compound cylinders are constructed by assembling two or more concentric cylindrical components, and their fabrication can be accomplished through various established techniques. As noted by Bahoum et al. (2017), common manufacturing methods include hydraulic expansion, thermo-hydraulic expansion, and forming using welded plates. An additional widely used approach is shrink-fitting, where one cylinder is inserted into another using a precisely controlled diametrical interference fit (Aydin et al., 2020; Özel et al., 2005). In this process, the outer cylinder is typically heated to expand its diameter, allowing it to be fitted over the inner cylinder. According to Das et al. (2024), as the outer cylinder cools and contracts, it applies compressive forces onto the inner cylinder, inducing a compressive stress state in the inner wall, while the outer cylinder experiences tensile stresses. When the compound cylinder is later subjected to internal pressure, the resulting tangential or hoop stresses are more evenly distributed across the entire wall thickness. This improved distribution is achieved through the algebraic superposition of the residual stresses introduced during shrink-fitting and the operational stresses caused by the internal pressure, as illustrated in Figure 2.4.

a) Tangential stress due to p_i b) Residual stress   c) Resultant tangential stress
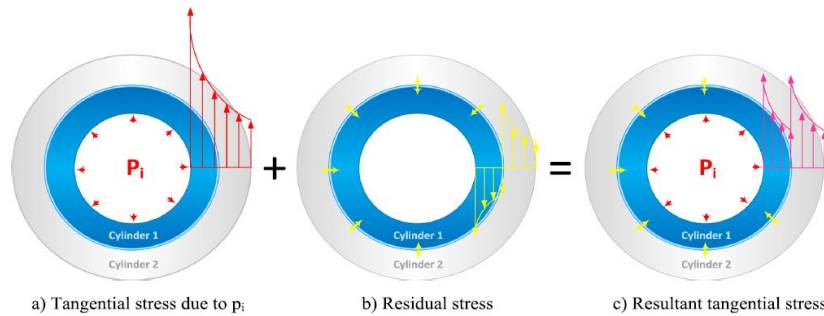
Figure 2.3 Two-layer compound cylinders (Es-saheb et al., 2024)

One of the widely adopted approaches in the stress analysis and design of pressure vessels is the use of established design codes. Design codes such as the ASME Boiler and Pressure Vessel Code play a critical role in ensuring the safe construction and operation of pressure vessels, as poorly constructed vessels that cannot handle high pressure pose serious safety risks, including explosions and leakage. These codes provide standardized rules and regulations that dictate how pressure vessels and pressure cylinders should be designed, manufactured, and certified, thereby minimizing hazards and ensuring consistent safety across the industry (Hazizi & Ghaleeh, 2023). By establishing clear guidelines for safe design and manufacturing, these codes help to prevent accidents and promote uniform safety standards (J. Kihiu & Masu, 1995). Typically, they offer predefined combinations of wall thickness and corresponding hoop stresses, ensuring that these stresses remain below the allowable working limits. However, as J. M. Kihiu (2002) point out, such codes often lack comprehensive analytical treatment of stress distributions within the vessel walls. As a result, to ensure safety, engineers frequently apply high safety factors, leading to over-design (Masu, 1997). While this approach enhances reliability, it also significantly increases material usage and manufacturing costs. In response to these limitations, alternative techniques such as shakedown analysis, autofrettage, composite overwrapping, thick cylinder modeling, and compound cylinder construction have been developed to improve structural strength and optimize material efficiency in pressure vessel design.

3. Recent Computational Advancements

Finite Element Analysis (FEA) is a powerful numerical simulation technique used to solve complex engineering problems by discretizing a structure into smaller, manageable finite elements. As described by Mutava et al. (2016), FEA enables engineers to model and analyze the stress behavior of pressure vessels—especially thick-walled vessels—under various loading conditions. Using software different techniques, computational FEA allows for detailed examination of stress fields (hoop, radial, axial), strain distributions, and deformations within both elastic and plastic

regimes. This is particularly valuable when dealing with non-uniform geometries, stress concentrations (e.g., around nozzles), or material nonlinearities where analytical methods are insufficient. By applying boundary conditions, material properties, and pressure loads in a simulated environment, FEA supports the design and safety validation of pressure components, making it an indispensable tool in modern structural mechanics and pressure vessel engineering.

Evans & Miller (2015) explored the use of nonlinear Finite Element Analysis (FEA) in predicting failure pressure and failure location in pressure vessels. Using ANSYS Mechanical software, they analyzed two components—a puncture disk and a non-uniform toroidal pressure vessel—by applying internal pressure loads and comparing the resulting total mechanical strain to the actual elongation limits of the materials. The puncture disk was modeled as a 2D axisymmetric geometry using Plane 183 elements, while the toroidal vessel was modeled in full 3D with 10-node tetrahedral elements due to its complex shape. The analysis employed isotropic hardening models for titanium alloys to simulate elastic-plastic behavior. Their FEA predictions of failure pressure were validated through physical testing, showing strong correlation, particularly for the symmetric geometry. The study demonstrated that nonlinear FEA is an effective tool in assessing failure risks, especially when analytical methods are insufficient due to geometric complexity or material behavior under high stress.

In a study by Biradar (2022), Finite Element Analysis (FEA) was applied to evaluate the structural integrity of a cylindrical pressure vessel using ANSYS Workbench 14.5, with geometric modeling carried out in SolidWorks. The vessel, made of structural steel, was subjected to an internal pressure of 3 MPa with fixed support at the base, and the analysis aimed to compute hoop stress, longitudinal stress, maximum shear stress, and equivalent Von Mises stress. The model was meshed using quadrilateral elements, and the boundary conditions were implemented based on standard dimensions (cylinder diameter 670 mm, height 1030 mm, thickness 10 mm). Results showed a strong correlation between FEA and theoretical values, particularly for hoop and shear stresses, with minimal percentage errors. The study concluded that the design was structurally safe, as all stress values remained within the yield strength limits of the material. This work demonstrated the effectiveness of FEA in validating pressure vessel designs and minimizing over-conservatism in engineering practice.

GEZGİNCİ et al. (2022) conducted a detailed Finite Element Analysis (FEA) using ANSYS ACP (Pre), Static Structural, and ACP (Post) modules to evaluate the stress and deformation behavior of composite oil separator pressure vessels used in screw-type compressor systems. The separator

tank featured a 0.5 mm structural steel liner wrapped with 3.5 mm of composite materials, namely carbon fiber/epoxy, glass fiber/epoxy, and Kevlar fiber/epoxy. Models were exposed to internal pressures of 11.25, 15, and 19.5 bar at a maximum temperature of 110°C. FEA simulations were used to assess the influence of various winding angles (35°, 45°, 55°, 65°) on first-ply equivalent stress (FPES) and total deformation. Results showed that glass fiber/epoxy offered the lowest FPES at specific winding angles depending on pressure, while Kevlar fiber/epoxy consistently minimized deformation, especially at 45° orientation. The study demonstrates how composite layering and orientation optimization through FEA can enhance pressure vessel performance under high-pressure thermal conditions.

Świt & Szczecina (2025) emphasized the critical role of finite element analysis (FEA) in optimizing pressure vessel design, particularly for evaluating complex stress interactions that are difficult to capture through analytical methods. Utilizing ABAQUS software, the researchers conducted a nonlinear elastic-plastic simulation to assess the impact of elliptical reinforcing pad geometry on the structural performance of a steel pressure vessel. The analysis, which included temperature-dependent material properties and coupled thermal-stress conditions at an operating temperature of 150 °C, was performed under both design (2.5 MPa) and test (3.9 MPa) internal pressures. Through FEA, they demonstrated that elliptical pads significantly reduce stress concentrations at the nozzle-shell junction, enabling a 36% decrease in shell thickness—from 28 mm to 18 mm—and about a 30% reduction in total vessel mass. The study show how FEA serves as a powerful tool for structural validation and optimization, offering engineers the capability to refine geometries and material usage while maintaining safety and performance.

Tamrat (2017)conducted a comprehensive design and analysis of a Type IV composite pressure vessel intended for liquefied petroleum gas (LPG) storage, emphasizing the use of finite element analysis (FEA) to optimize structural integrity and weight reduction. Using ABAQUS software, the team modeled a high-density polyethylene (HDPE) liner reinforced with E-glass/epoxy composite layers wound through a filament winding process. The study applied Classical Lamination Theory (CLT) and Netting Analysis to determine the optimal ply angle, identified as 54.65°, for maximum stress resistance. FEA simulations, performed under a working pressure of 2 MPa, incorporated the Hashin Damage criteria to assess fiber and matrix failures. Results indicated that the vessel design remained within safe stress limits and achieved a weight reduction of 61.5% compared to steel cylinders. The research highlighted the importance of FEA in evaluating the structural behavior, validating analytical models, and supporting design decisions for lightweight, high-strength composite pressure vessels.

10

Bouhala et al. (2024) emphasized the critical role of Finite Element Analysis (FEA) in the structural assessment and optimization of composite pressure vessels. In their study, they designed a Type IV LPG cylinder using a high-density polyethylene (HDPE) liner reinforced with E-glass/epoxy composite, applying ABAQUS software for simulation. The research integrated analytical techniques like Classical Lamination Theory (CLT) and Netting Analysis to determine the optimal ply angle of 54.65°, enhancing the vessel's load-bearing capacity. FEA simulations evaluated longitudinal and transverse stresses and implemented the Hashin damage criterion to analyze fiber and matrix failure modes. The simulation results closely matched the analytical findings, confirming the design's reliability. Notably, the vessel withstood a working pressure of 2 MPa and demonstrated a burst pressure of 15 MPa, with an overall weight reduction of 61.5% compared to conventional steel cylinders. This study describes FEA's importance in enabling safer, lighter, and more efficient composite pressure vessel designs.

Wang et al. (2025) proposed an intelligent stress prediction framework for metal pressure-bearing components in thermal power plants by integrating Finite Element Analysis (FEA) with machine learning techniques. The study employed ANSYS software to simulate complex stress fields under operational conditions and used the resulting dataset to train various machine learning models, including decision trees, support vector machines (SVM), and neural networks. Their goal was to accurately predict equivalent stress distribution in key regions of pressure-bearing components, such as elbows and junctions, based on multiple influencing parameters like temperature, pressure, and geometry. By comparing the performance of different models, the authors found that ensemble learning and deep neural networks achieved superior prediction accuracy. This approach significantly reduced computational time while maintaining high fidelity, demonstrating the viability of combining FEA with Machine Learning (ML) for real-time stress analysis. The study highlights the growing importance of intelligent modeling in enhancing the safety, reliability, and efficiency of pressure vessels in power generation system.

Fan & Hu (2023) developed an innovative approach to predicting local stresses in pressure vessel nozzle connections by integrating FEA with ML techniques. Recognizing the complexity and computational demands of traditional FEA methods, particularly for localized stress regions, the authors created a software plugin for ABAQUS that automates dataset generation and trains a machine learning model using Python and libraries like Scikit-learn. The resulting predictive model was incorporated into a user-friendly graphical interface, enabling rapid and accurate stress estimations. The software achieved a prediction accuracy exceeding 0.999 and a mean squared error of just 1.639, making it a highly efficient alternative to full-scale FEA simulations. By

minimizing analysis time and complexity, this hybrid tool offers a practical solution for design optimization and safety assessment of pressure vessels. The study shows the potential of AI-enhanced FEA tools in advancing engineering analysis workflows, particularly for applications requiring fast, accurate, and scalable stress evaluation.

Fazle et al. (2023) proposed a real-time predictive failure analysis framework for pressure vessels by integrating Finite Element Analysis (FEA) with advanced machine learning techniques. The study utilized sensor-fused datasets and employed Convolutional Neural Networks (CNN) and Long Short-Term Memory (LSTM) models to accurately detect and predict structural faults. This fusion of AI and sensor data allowed for dynamic analysis of stress behaviors and anomalies under varying operating conditions. By training on time-series sensor data, the models provided early warning indicators of failure, significantly enhancing reliability and safety in pressure vessel operations. The methodology's strength lies in its adaptability and ability to process real-time data, making it highly applicable to industrial monitoring systems. The research highlights the importance of combining FEA-derived insights with deep learning architectures for continuous, intelligent evaluation of pressure vessel integrity, offering a practical path toward predictive maintenance and minimizing catastrophic failures in critical systems.

Vardhan & Sztipanovits (2022) developed a deep learning-based surrogate model to replace traditional finite element analysis (FEA) in the stress analysis of sub-sea pressure vessels, which are critical for housing electronic components in autonomous underwater vehicles. Given the computational intensity of running FEA simulations for iterative design optimization, their study aimed to create a more efficient method using machine learning. A deep neural network (DNN) architecture with nine layers was trained on FEA-generated data to predict maximum Von-Mises stress under varying design parameters, such as vessel thickness and sub-sea depth. The model significantly outperformed other machine learning regressors, including Random Forest and Gradient Boosting, achieving 92% prediction accuracy on sparse datasets. This approach accelerates the evaluation of design alternatives and supports optimization by bypassing repetitive FEA simulations. The integration of deep learning and FEA demonstrated a powerful methodology for reducing computational cost while maintaining high accuracy in structural integrity assessments of pressure vessels under deep-sea conditions

Zolfaghari & Izadi (2020) proposed an Artificial Neural Network (ANN)-based model to predict the burst pressure of steel cylindrical pressure vessels, addressing the limitations of traditional empirical, theoretical, and finite element analysis (FEA) methods. Accurate prediction of burst

pressure is vital for the safe design and cost-effective operation of pressure vessels, particularly under high-pressure or hazardous conditions. The researchers used 90 experimental data points with parameters including vessel dimensions and material strengths to train the ANN. The model employed a two-hidden-layer architecture and achieved a high correlation between predicted and observed values, with a maximum relative error of only 8.89%. Compared to five classical prediction criteria—including those by Faupel (2022), Svensson (2021), and Christopher et al. (2002)—the ANN model consistently demonstrated superior accuracy and generalizability. This study exemplifies the effective integration of machine learning into structural integrity assessment, offering a robust alternative to traditional FEA for burst pressure prediction across a wider range of vessel geometries and materials.

4. Fatigue and Failure Prediction

Classical fatigue assessment and failure prediction is based on the following two main relationship curves (Fricke, 2013), herein referred to as classical fatigue life prediction approaches and are used in designing against fatigue failures. Firstly, S-N approach, describing the relationship between fatigue life in cycles (N) and applied stress parameter (S). Examples of stress parameters include nominal stress, maximum stress or stress amplitude. Secondly, the fracture-mechanics approach which treats growing of cracks using developed using crack propagation laws (e.g. Paris Law) based on fracture mechanics, and assuming an initial crack length. Another approach is the strain-based approach, which involves more detailed analysis of the localized yield that may occur at stress raisers during cyclic loading (Dowling, 2013). However, new approaches to fatigue life assessment have been proposed.

Physics-Informed Neural Networks (PINNs) are an emerging class of machine learning algorithms that integrate physical laws—typically formulated as partial differential equations (PDEs)—directly into the learning process, offering enhanced accuracy and physical consistency in engineering simulations. Zhou et al. (2025) developed a general PINN framework for fatigue life prediction in metallic materials by embedding partial differential inequalities, derived from experimental and theoretical observations, into the neural architecture. Their model was validated using fatigue data from LZ50 and SLM 316L steels as well as nine additional metals, and demonstrated improved predictive accuracy and generalization over conventional neural networks, particularly in high-cycle fatigue scenarios relevant to pressure vessels. Complementing this, Goswami et al. (2020) proposed a PINN approach specifically for brittle fracture analysis, reformulating the training objective to minimize variational energy rather than equation residuals.

This energy-based method simplifies boundary condition enforcement and reduces computational load. The study also introduced transfer learning and NURBS-based geometric modeling to enhance performance in complex domains. Together, these contributions emphasizes the growing utility of PINNs in fatigue life prediction and stress analysis, especially for complex, safety-critical structures like pressure vessels, where combining data-driven learning with physical fidelity is essential.

Bayesian Inference has emerged as a powerful methodology for addressing uncertainty in fatigue life prediction and stress analysis of structural components such as pressure vessels. Karandikar et al. (2012) employed a Bayesian framework to estimate the Remaining Useful Life (RUL) of an aircraft fuselage panel subjected to cyclic pressurization. By modeling key parameters in Paris' law—such as the crack growth constants m and C, and the initial crack size a_0—as random variables, the study generated probabilistic fatigue crack growth curves using a random walk method. These predictions were iteratively refined using simulated data, capturing both model and sensor uncertainties to enhance RUL estimation accuracy. Building on this direction Zhuang et al. (2024) applied Bayesian inference to estimate the Equivalent Initial Flaw Size Distribution (EIFSD) in shallow shell structures and pressure vessels. Their method combined Bayesian networks with surrogate modeling via Co-Kriging and crack growth simulations using the Dual Boundary Element Method (DBEM). This hybrid strategy lowered computational demands while preserving high accuracy, supporting effective inspection and maintenance planning. Together, these studies outline the expanding role of Bayesian methods in fatigue life prediction, providing robust and efficient tools for uncertainty quantification in critical engineering systems.

Ou & Guo (2025)present a data-driven deep learning framework for predicting fatigue life in additively manufactured metallic materials, with relevance to stress analysis in pressure vessels where fatigue failure is critical. Their approach combines Gated Recurrent Unit (GRU) and Transformer models in a parallel architecture to effectively capture both local and global dependencies within fatigue data. This hybrid structure enables robust feature extraction across varying load conditions, essential for assessing structural health in complex systems like pressure vessels. The model's performance is further enhanced through Hybrid Leader-Based Optimization (HLBO), which efficiently tunes hyperparameters to improve prediction accuracy and generalization. Validated on the FatigueData-AM2022 dataset, the framework demonstrates superior accuracy compared to traditional deep learning models, especially in handling high-dimensional, multi-modal fatigue data. This research highlights the potential of advanced deep learning techniques in improving fatigue life prediction, contributing to more reliable condition

14

monitoring and maintenance planning of critical components in safety-sensitive engineering applications.

Guo et al. (2025) and Li et al. (2017) both present advanced multiscale modeling frameworks using crystal plasticity (CP) to enhance the prediction of low-cycle fatigue (LCF) in pressure vessel materials by accounting for microstructural effects. Guo et al. introduced a coupled CP and multistage fatigue (MSF) model to predict the LCF life of laser-directed energy deposited (LP-DED) TC11 titanium alloys used in aerospace pressure vessels. Their model integrates crystal orientation, α-lath morphology, and evolving micromechanical damage, achieving a high prediction accuracy with a mean error of 4.6%. Experimental validation showed that features like basketweave microstructures significantly enhance fatigue resistance. Similarly, Li et al. developed a CP-based multiscale finite element model for P91 steel under high-temperature conditions, incorporating realistic grain and precipitate geometries, strain gradient effects, and dislocation-based cyclic softening mechanisms. Their model accurately predicted crack initiation cycles and demonstrated the detrimental impact of precipitate coarsening on fatigue life. Both studies highlight the critical role of microstructure-sensitive modeling in capturing anisotropic deformation, dislocation dynamics, and multiscale damage progression, thereby advancing fatigue life prediction and structural integrity assessment of pressure vessel materials under complex loading and environmental conditions.

In recent advancements in structural health monitoring, Digital Twins (DTs) have emerged as transformative tools for real-time fatigue life prediction and stress analysis in pressure vessels. For instance, Khaled et al. (2025) developed a DT framework that integrates Internet of Things (IoT), simulation, and fatigue modeling to monitor damage in pressure vessels subjected to cyclic loading. The system is built upon a 3D finite element (FE) model of a reduced-scale physical twin, continuously updated using experimental pressure data. The DT incorporates both uniaxial and multiaxial fatigue criteria, selecting the maximum principal stress-based S/N curve approach for damage prediction. Various approaches, S/N-based, incremental, and continuous damage—were evaluated to enhance prediction reliability. Hybrid modeling techniques, combining physical models with machine learning algorithms like Bayesian neural networks and Gaussian process regression, were explored to improve accuracy and responsiveness. This digital twin enables predictive maintenance, mitigating costly inspections and unplanned downtimes. The research highlights the utility of DTs in identifying critical zones, quantifying progressive damage, and optimizing inspection schedules, particularly in safety-critical applications like chemical reactors and hydrogen storage vessels.

Probabilistic methods have become indispensable in the fatigue life assessment of pressure vessels, particularly where failures are initiated by inherent material defects such as pores or inclusions. Todinov (1998) presented a foundational probabilistic framework that models the initiation of dominant cracks from categorized defect types and sizes using Monte Carlo simulations. The research revealed that scatter in fatigue life arises more from the statistical variation in defect characteristics than from differences in crack propagation, and that reducing pore sizes below a critical threshold (≈15 μm) yields minimal benefits. This finding points out the importance of defect characterization in enhancing fatigue life predictions. Building on this, Cronemyr & Eriksson (2024)introduced a practical tool integrating probabilistic fatigue analysis with robust design principles. Their method combines finite element analysis (via ANSYS) and quality management tools (e.g., Excel and Minitab) to generate regression models and response surfaces, allowing designers to address variability in loads, materials, and environmental conditions early in the design cycle. This approach enables the creation of robust S-N curves under variable amplitude loading, thus improving early-stage decision-making. Complementing these contributions, Faghihi et al. (2017) developed a comprehensive probabilistic framework incorporating fatigue testing of Ti6Al4V alloys, continuum damage mechanics (CDM), and Bayesian model calibration. Their methodology accounts for uncertainties in model inputs and experimental data through global sensitivity analysis and Monte Carlo simulations, supporting predictive reliability under high-cycle fatigue. Collectively, these studies highlight the evolving role of probabilistic fatigue modeling in delivering more accurate, robust, and cost-effective life predictions for critical pressure vessel components.

In the pursuit of accurate fatigue life prediction for complex pressure vessel structures, Song et al. (2018) developed a novel reliability-based methodology utilizing a time-varying surrogate modeling approach. Recognizing the limitations of traditional deterministic models in accounting for uncertainties such as material variability, fluctuating loads, and model imperfections, the study introduces a Time-Varying Particle Swarm Optimization-based General Regression Neural Network (TV/PSO-GRNN) model. This surrogate model is designed to address the computational challenges of Monte Carlo simulations by combining efficient sampling techniques, like Latin Hypercube Sampling, with the robust nonlinear mapping capabilities of GRNN, optimized via dynamic PSO. The proposed framework significantly improves computational efficiency while maintaining high prediction accuracy for fatigue life under multiphysics interactions. Validation was carried out on an aircraft turbine blisk, where the model successfully captured reliability distributions and failure sensitivities. This study draws to our attention the importance of

integrating machine learning-based surrogate models with probabilistic design methods to manage uncertainties in fatigue analysis, offering a powerful tool for enhancing reliability and supporting design optimization of critical structural components such as pressure vessels.

5. Experimental Techniques and Validation

Experimental techniques and validation methods play a crucial role in the stress analysis of pressure vessels, providing reliable data to verify analytical and numerical models, assess structural integrity under operational conditions, and ensure compliance with safety standards across various industries.

Therefore, experimental validation is essential for improving the accuracy and reliability of stress analysis models in pressure vessel design. Zhu (2025) focused on validating the Zhu–Leis exact flow solution from the work done by Zhu & Leis (2006) for thick-walled cylindrical pressure vessels through a series of full-scale burst pressure tests. Unlike the traditional Barlow formula $(P_o = (\frac{2t}{D})\sigma_{uts})$—which assumes thin-walled geometry and neglects plastic flow—the Zhu–Leis solution incorporates multiaxial plastic deformation, extending its applicability to both thin- and thick-walled configurations. Six full-scale burst tests on Grade B carbon steel pipes with varying D/t ratios confirmed the solution's predictive accuracy, highlighting the importance of empirical data in verifying advanced theoretical models. Similarly, Dilip & Kumar (2014) performed experimental tests on cylindrical vessels with 45° oblique nozzles to validate nonlinear elastic-plastic finite element analysis (FEA) predictions. Using hydrostatic testing and distortion measurements, along with methods such as the Twice Elastic Slope and Tangent Intersection, their results closely matched FEA outputs. Together, these studies emphasize the indispensable role of experimental testing in verifying both analytical and numerical models, thereby ensuring robust and safe pressure vessel design under complex stress states and geometric configurations.

Digital Image Correlation (DIC) is a non-contact, full-field optical technique that has emerged as a vital tool for stress and strain analysis in pressure vessels. Rodrigues et al. (2014) demonstrated DIC's effectiveness by applying it to thin-walled cylindrical vessels with corrosion defects, showing that it could accurately measure both elastic and plastic surface strains. Their results correlated well with strain gauge data and highlighted discrepancies in traditional burst pressure prediction models, where DIC measurements confirmed the conservativeness of the DNV RP-F101 method. Similarly, Xu et al. (2016) used 3D DIC to evaluate strain fields around pit defects under varying internal pressures. Their study emphasized that maximum strain occurs at the deepest point of a pit and decreases radially, offering key insights into stress concentration

behaviors. Complementing these experimental studies, Lava et al. (2020) focused on integrating DIC with Finite Element Analysis (FEA) through a novel "DIC-levelling" method. By simulating DIC images from FEA outputs, they ensured accurate full-field comparison, overcoming limitations such as resolution and coordinate mismatches. This fusion of DIC and FEA provides robust model validation and enhances confidence in simulation-based assessments. Collectively, these studies underscore DIC's critical role in both experimental and computational validation of pressure vessel behavior. Its non-intrusive nature, real-time capabilities, and ability to resolve complex stress patterns around defects make it indispensable for improving structural integrity assessments and advancing safety in industrial applications.

Photoelasticity is an established experimental technique used in stress analysis to visualize and quantify stress distribution, particularly around discontinuities in mechanical structures such as pressure vessels. In a study by Pástor et al. (2015), photoelasticity was applied alongside Digital Image Correlation (DIC) to assess stress fields in a model with stress concentrators under bending loads. The photoelastic method utilizes polarized light and birefringent materials to produce isochromatic fringe patterns, where each fringe represents a constant difference in principal stresses. The researchers employed a polariscope and optical compensator to obtain full-field stress distributions and identify areas of stress concentration, including those near holes, notches, and other geometric features. Their study demonstrated that photoelasticity enables real-time observation of stress redistribution and elastic-plastic transitions under varying loads. The method allows optimization of structural components by identifying high-stress regions and suggesting modifications to improve reliability and reduce weight. The results also served to validate numerical simulations, highlighting photoelasticity's role in structural safety evaluations and design optimization of pressure-bearing components.

Strain gauges have long served as an effective and economical tool for experimental stress analysis, particularly in validating Finite Element Analysis (FEA) models of pressure vessels. Sulwinski & Johnston (2023) presented a comprehensive methodology for comparing FEA predictions with strain gauge measurements using a pressurized cylindrical vessel. The study employed 45° three-axis strain gauge rosettes to capture normal strains at critical locations identified through preliminary FEA. These strain readings were converted into principal strains and stresses, von Mises equivalent stress, and maximum shear values using analytical equations grounded in plane stress assumptions. Visualization tools like the 3D Mohr's circle were used to compare the stress states obtained experimentally and numerically. The results demonstrated a strong correlation between FEA and strain gauge data, with percentage differences mostly within

5%, affirming the reliability of both the modeling assumptions and the measurement techniques. This work underscores the critical role of strain gauge validation in refining numerical simulations and supporting structural integrity assessments of pressure vessels.

6. Future Trends and Research Directions

The future of stress analysis in pressure vessels is increasingly being shaped by the integration of advanced digital technologies. Artificial Intelligence (AI) and Machine Learning (ML) are anticipated to revolutionize real-time stress monitoring and predictive maintenance, enhancing operational reliability. Emerging methods like Physics-Informed Neural Networks (PINNs) and multiscale crystal plasticity models offer improved fatigue life prediction by embedding physical laws and microstructural behavior into data-driven models. Digital Twin technology, coupled with Internet of Things (IoT) systems, enables real-time simulation updates and condition-based maintenance strategies. Bayesian inference and probabilistic approaches are gaining traction for uncertainty quantification and lifecycle predictions. Despite these advancements, challenges remain in standardization, validation, and regulatory acceptance of these novel techniques. Future research should focus on hybrid frameworks that combine physics-based and AI models, multiscale material behavior simulation, and robust experimental validation to ensure the safe, efficient, and cost-effective design of next-generation pressure vessels.

7. Conclusion

In conclusion, this review has highlighted the progression from classical stress analysis techniques—such as analytical methods based on Lame's equations and experimental approaches like photoelasticity and strain gauge measurements—to modern computational and AI-enhanced methods in pressure vessel design. While traditional techniques provided essential insights into stress behavior, they are limited in addressing complex geometries, multi-physics interactions, and real-time monitoring needs. Advanced tools like Finite Element Analysis (FEA) and AI-driven predictive models, including machine learning algorithms and digital twin frameworks, now enable accurate stress estimation, fatigue life prediction, and condition-based maintenance. Integrating classical principles with these innovative technologies is crucial for developing safe, reliable, and efficient next-generation pressure vessels.

References

Asif Shaikh, Prof. Surwase S. S., Prof. Doijode S. N., & Prof.Ovarikar G. P. (2024). REVIEW ON STRUCTURAL INTEGRITY OF A PRESSURE VESSEL VIA ANSYS-BASED STRESS ANALYSIS. *JournalNX - A Multidisciplinary Peer Reviewed Journal*, *10*(5), 209–216. https://repo.journalnx.com/index.php/nx/article/view/5377

Aydin, M., Yapan, Y., & Türköz, M. (2020). *Investigation on Effect of Shrinkage Allowance to the Fatigue Life of Compound Cylinders Operating at High Pressure*.

Bahoum, K., Diany, M., & Mabrouki, M. (2017). Stress analysis of compound cylinders subjected to thermo-mechanical loads. *Journal of Mechanical Science and Technology*, *31*(4), 1805–1811. https://doi.org/10.1007/s12206-017-0328-5

Bansal, R. K. (2015). *Strength of Materials (Mechanics of Solids)* (6th ed.). Laxmi Publications (P) Ltd.

Biradar, Rohitkumar. S. (2022). Finite Element Modelling and Analysis of Pressure Vessel. *International Journal for Research in Applied Science and Engineering Technology*, *10*(9), 910–914. https://doi.org/10.22214/ijraset.2022.46770

Bouhala, L., Koutsawa, Y., Karatrantos, A., & Bayreuther, C. (2024). Design of Type-IV Composite Pressure Vessel Based on Comparative Analysis of Numerical Methods for Modeling Type-III Vessels. *Journal of Composites Science*, *8*(2), 40. https://doi.org/10.3390/jcs8020040

Che, L., Wang, P., Ma, L., Feng, Y., Zhao, J., & Li, X. (2023). A simulation analysis method for strength and fatigue design of prestressed wound ultra-high pressure vessels. *Advances in Mechanical Engineering*, *15*(11). https://doi.org/10.1177/16878132231209640

Christopher, T., Rama Sarma, B. S. V, Govindan Potti, P. K., Nageswara Rao, B., & Sankarnarayanasamy, K. (2002). A comparative study on failure pressure estimations of unflawed cylindrical vessels. *International Journal of Pressure Vessels and Piping*, *79*(1), 53–66. https://doi.org/https://doi.org/10.1016/S0308-0161(01)00126-0

Cronemyr, P., & Eriksson, R. (2024). *An Approach to Robust Fatigue Life Prediction to Be Used in Early Design Stages*. https://doi.org/10.32388/BG6QWB

Das, P., Islam, M. A., & Mondal, D. (2024). Analysis of thermomechanical stresses in dual compound thick cylinders under asymmetric loads: An analytical and numerical method. *Heliyon*, *10*(3). https://doi.org/10.1016/j.heliyon.2024.e24938

Digvijay, K., & Jewargis, S. (2015). Stress Analysis of Pressure Vessel with Different Type of End Connections by FEA. *International Journal of Innovative Research in Science, Engineering and Technology*, *4*(5), 2769–2775. https://doi.org/10.15680/ijirset.2015.0405016

Dilip, M. P., & Kumar, B. (2014). Experimental Analysis of Pressure Vessel. *INTERNATIONAL JOURNAL OF ENGINEERING RESEARCH & TECHNOLOGY (IJERT)*, *03*(09).

Dowling, E. N. (2013). *Mechanical Behavior of Materials: Engineering Methods for Deformation, Fracture, and Fatigue* (4th ed.). Pearson.

Es-saheb, M. H., Alsubaie, A., & Fouad, Y. (2024). Advance optimum design of multi-layer compound cylinders. *AIP Advances*, *14*(3), 035129. https://doi.org/10.1063/5.0188930

Evans, C. J., & Miller, T. F. (2015). Failure Prediction of Pressure Vessels Using Finite Element Analysis. *Journal of Pressure Vessel Technology*, *137*(5). https://doi.org/10.1115/1.4029192

Faghihi, D., Sarkar, S., Naderi, M., Rankin, J. E., Hackel, L., & Iyyer, N. (2017). A Probabilistic Design Method for Fatigue Life of Metallic Component. *ASCE-ASME J Risk and Uncert in Engrg Sys Part B Mech Engrg*, *4*(3). https://doi.org/10.1115/1.4038372

Fan, H., & Hu, L. (2023). Pressure vessel nozzle local stress prediction software based on ABAQUS- machine learning. *SoftwareX*, *24*, 101550. https://doi.org/10.1016/j.softx.2023.101550

Faupel, J. H. (2022). Yield and Bursting Characteristics of Heavy-Wall Cylinders. *Transactions of the American Society of Mechanical Engineers*, *78*(5), 1031–1061. https://doi.org/10.1115/1.4013916

Fazle, A. Bin, Prodhan, R. K., & Islam, M. M. (2023). AI-POWERED PREDICTIVE FAILURE ANALYSIS IN PRESSURE VESSELS USING REAL-TIME SENSOR FUSION : ENHANCING INDUSTRIAL SAFETY AND INFRASTRUCTURE RELIABILITY. *American Journal of Scholarly Research and Innovation*, *02*(02), 102–134. https://doi.org/10.63125/wk278c34

Fricke, W. (2013). IIW guideline for the assessment of weld root fatigue. *Welding in the World*, *57*, 753–791. https://doi.org/10.1007/s40194-013-0066-y

GEZGİNCİ, V., BOĞA, C., & SEYEDZAVVAR, M. (2022). Finite Element Analyses of Stresses Developed in Oil Separator Composite Tank Used in Screw Type Compressor Systems. *Bitlis Eren Üniversitesi Fen Bilimleri Dergisi*, *11*(4), 1093–1101. https://doi.org/10.17798/bitlisfen.1176937

Goswami, S., Anitescu, C., Chakraborty, S., & Rabczuk, T. (2020). Transfer learning enhanced physics informed neural network for phase-field modeling of fracture. *Theoretical and Applied Fracture Mechanics*, *106*, 102447. https://doi.org/https://doi.org/10.1016/j.tafmec.2019.102447

Guo, N., Yu, J., Zhou, Q., Wang, J., Xiao, G., Tang, B., & Zhang, Z. (2025). A multiscale crystal plasticity-multistage fatigue coupling framework for prediction of low-cycle fatigue life in laser additively manufactured titanium alloy. *Virtual and Physical Prototyping*, *20*(1), e2521103. https://doi.org/10.1080/17452759.2025.2521103

Hazizi, K., & Ghaleeh, M. (2023). Design and Analysis of a Typical Vertical Pressure Vessel Using ASME Code and FEA Technique. *Designs*, *7*(3), 78. https://doi.org/10.3390/designs7030078

Hearn, E. (1997). *MECHANICS OF MATERIALS 1* (E. J. B. T.-M. of M. 1 (Third E. HEARN, Ed.; 3rd ed.). Butterworth-Heinemann. https://doi.org/https://doi.org/10.1016/B978-0-7506-3265-2.50024-4

Hyder, M. J., & Asif, M. (2008). Optimization of location and size of opening in a pressure vessel cylinder using ANSYS. *Engineering Failure Analysis*, *15*(1), 1–19. https://doi.org/https://doi.org/10.1016/j.engfailanal.2007.01.002

Jacobs, R., Yamamoto, T., Odette, G. R., & Morgan, D. (2023). Predictions and uncertainty estimates of reactor pressure vessel steel embrittlement using Machine learning. *Materials & Design*, *236*, 112491. https://doi.org/10.1016/j.matdes.2023.112491

Kadam, R., Jagadale, S., & Karande, R. (2018). a Review on Stress Concentration Factor of Composite Pressure Vessel. *International Journal of Advance Research in Science and Enginerring*, *7*(1), 969–974.

Karandikar, J. M., Kim, N. H., & Schmitz, T. L. (2012). Prediction of remaining useful life for fatigue-damaged structures using Bayesian inference. *Engineering Fracture Mechanics*, *96*, 588–605. https://doi.org/https://doi.org/10.1016/j.engfracmech.2012.09.013

Khaled, Izat, Bennebach, Mohamed, Vasiukov, Dmytro, Shakoor, Modesar, & Chaki, Salim. (2025). Digital twin for real-time pressure vessels fatigue life prediction. *Advances in Mechanical Engineering*, *17*(5), 16878132251327666. https://doi.org/10.1177/16878132251327666

Khobragade, R. R., & Hiwase, V. (2017). Design & Analysis of Pressure Vessel with Hemispherical & Flat Circular End. *IJIRST-International Journal for Innovative Research in Science & Technology/*, *4*(1). www.ijirst.org

Kihiu, J. M. (2002). *Numerical Stress characterization in cross bored thick walled cylinders under internal pressure*. The University of Nairobi.

Kihiu, J., & Masu, L. (1995). The effect of chamfer and size on the stress distributions in a thick-walled cylinder with a cross bore under internal pressure. *Jomo Kenyatta University of Agriculture and Technology. Digital Repository*, *2*(February), 73–78. https://pdfs.semanticscholar.org/f331/cdd29dd745314cce340a31ddf0dfb643fe5a.pdf?_ga=2.127949516.1117804996.1588129569-1546471541.1581496640%0D

Koh, S.-K. (2000). Elastic-plastic stress analysis and fatigue lifetime prediction of cross-bores in autofrettaged pressure vessels. *KSME International Journal*, *14*(9), 935–946. https://doi.org/10.1007/BF03185796

Lava, P., Jones, E. M. C., Wittevrongel, L., & Pierron, F. (2020). Validation of finite-element models using full-field experimental data: Levelling finite-element analysis data through a digital image correlation engine. *Strain*, *56*(4). https://doi.org/10.1111/str.12350

Li, D.-F., Barrett, R. A., O'Donoghue, P. E., O'Dowd, N. P., & Leen, S. B. (2017). A multi-scale crystal plasticity model for cyclic plasticity and low-cycle fatigue in a precipitate-strengthened steel at elevated temperature. *Journal of the Mechanics and Physics of Solids*, *101*, 44–62. https://doi.org/https://doi.org/10.1016/j.jmps.2016.12.010

Masu, L. M. (1997). Cross bore configuration and size effects on the stress distribution in thick-walled cylinders. *International Journal of Pressure Vessels and Piping*, *72*(2), 171–176. https://doi.org/https://doi.org/10.1016/S0308-0161(97)00026-4

Mutava, J., Muvengei, O., Njoroge, K., & Kihiu, J. (2016, May 4). Finite Element Structural Analysis of a Thick-walled Pressure Vessel. *Proceedings of the 2016 Annual Conference on Sustainable Research and Innovation.*

Nziu, P., & Masu, L. (2019a). An Optimal Location of Elliptical Cross Bore in Elastic Pressurized Thick Cylinders. *International Journal of Mechanical and Production Engineering Research and Development*, *9*, 287–298. https://doi.org/10.24247/ijmperdaug201930

Nziu, P., & Masu, L. (2019b). Configuration of optimal cross bore shape in elastic pressurized high pressure vessels. *International Journal of Mechanical and Production Engineering Research and Development*, *9*(5), 197–210. https://doi.org/10.24247/ijmperdoct201918

Ou, C., & Guo, J. (2025). Data-Driven Prediction of Metal Fatigue Life. *Frontiers in Sustainable Development*, *5*, 405–430. https://doi.org/10.54691/20jg0s64

Özel, A., Temiz, Ş., Aydin, M. D., & Şen, S. (2005). Stress analysis of shrink-fitted joints for various fit forms via finite element method. *Materials & Design*, *26*(4), 281–289. https://doi.org/https://doi.org/10.1016/j.matdes.2004.06.014

Pástor, M., Hagara, M., & Kostka, J. (2015). Stress Analysis Performed by Photoelasticity and Digital Image Correlation. *Applied Mechanics and Materials*, *816*, 474–481. https://doi.org/10.4028/www.scientific.net/AMM.816.474

Phalguna, N. (2017). Stress and Failure Analysis of Thick Walled Cylinder with Oblique Hole. *International Journal of Engineering Research And*, *V6*.

Ramy Abdelsalam, O., & Sedaghati, R. (2013). Design Optimization of Compound Cylinders Subjected to Autofrettage and Shrink-Fitting Processes. *Journal of Pressure Vessel Technology*, *135*, 021209. https://doi.org/10.1115/1.4007960

Rodrigues, L., Freire, J., Vieira, R., & Castro, J. (2014). Strain Analysis of Thin Pipe Pressure Vessels Using Digital Image Correlation. *Journal of Mechanical Engineering and Automation*, *2014*, 63–72. https://doi.org/10.5923/j.jmea.20140402.03

Song, L.-K., Bai, G.-C., Fei, C.-W., & Wen, J. (2018). Reliability-Based Fatigue Life Prediction for Complex Structure with Time-Varying Surrogate Modeling. *Advances in Materials Science and Engineering*, *2018*(1). https://doi.org/10.1155/2018/3469465

Sulwinski, R., & Johnston, R. (2023). *Methodology for Validation of Finite Element Analysis Utilizing Strain Gauge Measurements*. https://doi.org/10.1115/VVUQ2023-108749

Svensson, N. L. (2021). The Bursting Pressure of Cylindrical and Spherical Vessels. *Journal of Applied Mechanics*, *25*(1), 89–96. https://doi.org/10.1115/1.4011694

Świt, G., & Szczecina, M. (2025). Numerical Study of the Reinforcing Pads Geometry of Pressure Vessels. *Materials*, *18*(10), 2318. https://doi.org/10.3390/ma18102318

Tamrat, S. (2017). *Design and Analysis of Pressure Vessel Using Finite Element Method*. *vi*, 1–4.

Tawade, S. (2019). Evaluation of Stresses in a Cylindrical Pressure Vessel with Varying Internal Pressure, Shell Thickness and Shell Diameter. *International Journal of Advanced Research in Science, Communication and Technology*. https://doi.org/10.48175/IJARSCT-446C

Thattil, M., & Pany, C. (2017). Design and Analysis of Pressure Vessel with different end domes. *International Journal of Science, Engineering and Technology Research (IJSETR) Volume 06,, Issue 08 August 2017,, ISSN: 2278 - 7798*.

Todinov, M. T. (1998). A probabilistic method for predicting fatigue life controlled by defects. *Materials Science and Engineering: A*, *255*(1), 117–123. https://doi.org/https://doi.org/10.1016/S0921-5093(98)00772-2

Vardhan, H., & Sztipanovits, J. (2022). *Deep Learning-based FEA surrogate for sub-sea pressure vessel*. https://doi.org/10.48550/arXiv.2206.03322

Wang, S., Shi, R., Wu, J., Ma, Y., Yang, C., & Liu, H. (2025). Stress Prediction Processes of Metal Pressure-Bearing Complex Components in Thermal Power Plants Based on Machine Learning. *Processes*, *13*(2), 358. https://doi.org/10.3390/pr13020358

Xu, W., Feng, X., Li, J., Shi, X., & Bai, T. (2016). *Strain analysis of pressure vessels contained pits based on digital image correlation method*. https://doi.org/10.1117/12.2211507

Zhao, M., Wu, Z., & Cai, H. (2018). Stress analyses of compound cylinders with interlayer pressure after autofrettage. *International Journal of Pressure Vessels and Piping*, *163*, 63–67. https://doi.org/https://doi.org/10.1016/j.ijpvp.2018.03.002

Zhou, S., Henrich, M., Wei, Z., Feng, F., Yang, B., & Münstermann, S. (2025). A general physics-informed neural network framework for fatigue life prediction of metallic materials. *Engineering Fracture Mechanics*, *322*, 111136. https://doi.org/https://doi.org/10.1016/j.engfracmech.2025.111136

Zhu, X.-K., & Leis, B. N. (2006). Average shear stress yield criterion and its application to plastic collapse analysis of pipelines. *International Journal of Pressure Vessels and Piping*, *83*(9), 663–671. https://doi.org/https://doi.org/10.1016/j.ijpvp.2006.06.001

Zhuang, M., Morse, L., Sharif Khodaei, Z., & Aliabadi, M. H. (2024). Bayesian-informed fatigue life prediction in shallow shell structures with the dual boundary element method. *Engineering Fracture Mechanics*, *308*, 110348. https://doi.org/https://doi.org/10.1016/j.engfracmech.2024.110348

Zolfaghari, A., & Izadi, M. (2020). Burst Pressure Prediction of Cylindrical Vessels Using Artificial Neural Network. *Journal of Pressure Vessel Technology*, *142*(3). https://doi.org/10.1115/1.4045729

Identification of Narrowband Noise Interference and Characterization of Impulsive Noise in Low-Voltage Broadband Power Line Communication Networks in Kenyan Urban Environment

E. O. Odipo[1*], S. O. Awino[2], M. N. Ahuna[1]

[1]Department of Electrical and Electronics Engineering, the Technical University Kenya.
[2]Department of Physics, Pwani University.

*Corresponding author: Elly.Odipo@tukenya.ac.ke

Abstract

Power Line Communication (PLC) has emerged as a promising technology for broadband access, home networking, and smart grid applications due to the availability of existing power infrastructure. However, its performance is significantly affected by noise, particularly narrowband interference and impulsive noise, which degrade data transmission reliability. Unlike Gaussian noise, impulsive noise in PLC is irregular and complex, originating from both natural and man-made sources, making it difficult to model using conventional techniques. This study investigates narrowband noise interference and characterizes impulsive noise in low-voltage broadband PLC networks within an urban Kenyan environment. Measurement-based analysis was conducted using data from diverse locations, capturing the time-varying and frequency-selective properties of PLC noise. Various noise models, including Middleton Class A, Bernoulli Gaussian, and Symmetric Alpha Stable distributions, were applied to evaluate their suitability for modeling impulsive noise. Additionally, time series approaches such as ARMA, ARIMA, and SARIMA were employed to capture the stochastic and seasonal behaviors of noise. Findings reveal that impulsive noise exhibits significant amplitude variability, strong burst characteristics, and frequency-dependent attenuation, consistent with prior studies but influenced by local network structures. The results contribute to improved noise characterization, offering insights for developing robust algorithms to enhance reliable PLC communication in hostile environments.

Keywords: - Alpha Stable distribution, Bernoulli Gaussian distribution, Impulsive Noise, Middleton Class A distribution.

1. Introduction

In the 50–60 Hz frequency range, power lines are made to carry electricity from a few sources, such generators, to a large number of users. Protecting specific areas of the power distribution network in the case of a malfunction was the main goal of the initial data transmissions across power lines. Power line communications (PLC) are primarily used for power line protection. To reduce the impact of a failure, power plants, substations, and distribution centers must quickly transmit information when one is discovered. Towers used for power transmission are sturdy constructions. Therefore, any protective signaling mechanism would operate best on the networks from a reliability perspective. The telephone networks do not adequately serve many remote regions. It was found that using the current power lines for signaling and information exchange is an effective way to secure the power system [1].

Analogue telephone systems are used to send the highest amounts of data concurrently with voice data for telemetering and security purposes. Automatic telemetering and remote status parameter monitoring without humans are becoming more and more helpful these days. Digital communications across electricity lines have a somewhat more important role than telephone systems these days. Given the length of time that data transmission over electrical lines has existed, it is currently gaining increased attention.

Only a few Kbits per second is the data rate needed for telemetering and security. The Mbits per second of data utilized for multimedia applications cannot be compared to it. A confluence of events that occurred in the mid-to-late 1990s is the answer. An illustration of this is the internet's emergence and rapid expansion in the 1990s. The technological developments of digital signal processing (DSP) and very large-scale integration (VLSI) were the cause of this expansion. The global liberalization of the telecommunications industry has made the last tendency worse [2].

Power line communications are now a feasible technology for high-speed home networking and could be a solution to the "last mile" issue as a result of the previously listed events. Power line communications (PLC) can be either in-premises (also known as "last inch") or to-premises (also known as "last mile") access. Other last-mile access methods including cable, wireless, and Home PNA are inferior to power line communications. The guidelines created by the Home Phone Networking Alliance serve as the foundation for phone-line networking, often known as Home PNA. Figure 1.1 illustrates the concept of in-premises networking, while Fig. 1.2 illustrates the "last mile" concept[3].
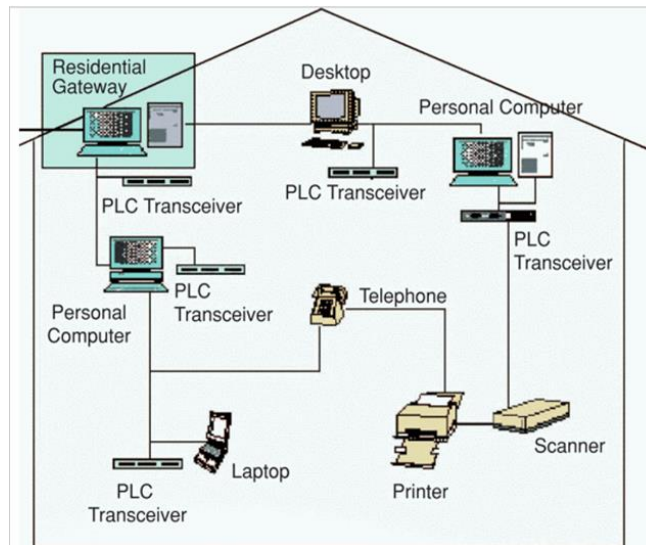
Figure 1.1: The in-home networking
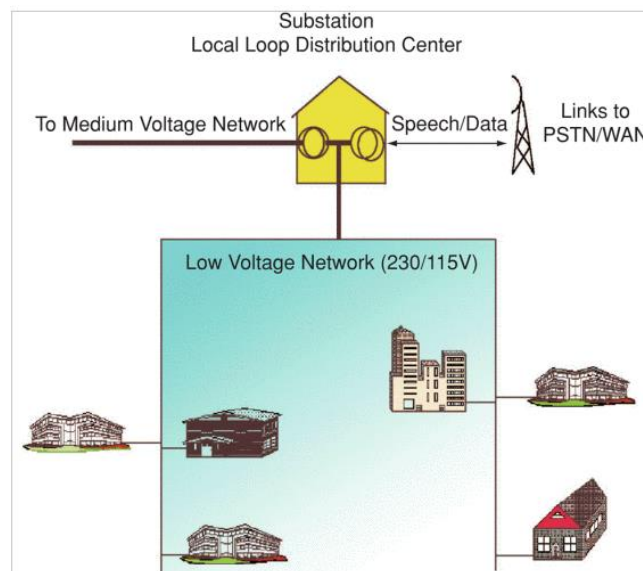
Figure 1.2: The "last mile" broadband access to homes from the local distribution center

PLC is one of numerous potential technologies that are made available by the "last mile" access, which also includes broadband wireless, cable modems, and various forms of Digital Subscriber Lines (xDSL). Is PLC not seen as superior to other technologies, or are the other technologies flawless or superior to PLC in every way?

The primary advantage of PLC is that power lines are already in place, making it the ideal medium for delivering broadband connections to urban areas where data and phone infrastructure are common. Hence, saving on additional cabling. PLC improves energy use, enhances communication, and most importantly, allows for the use of renewable energy sources [4]. The result is that it has become one of the key components of modern communication. Some of the resulting benefits include:

a) Cost effectiveness

PLC uses existing power lines infrastructure, which brings down the cost of initial implementation to a minimum compared to the use of separate copper or fiber optics networks or standalone communication wireless methods [4].

b) Enhanced Reliability

The main observation in the use of wireless systems is that there are data transmission difficulties resulting from interference. PLC minimizes these issues and provides stable data transmission [4].

c) Scalability

PLC system can be modified with new devices and technologies without large changes to the infrastructure [4].

d) PLC improves energy management.

The implementation of the PLC system for energy management is important because it minimizes energy consumption. Transmission of information in real time makes it possible for utilities to understand consumption patterns and use demand response measures. This capability is a prerequisite to modernization of the in-house power network and results in energy being distributed according to the needs at the time of distribution [5].

e) PLC and renewable energy sources

The complexity of incorporating such resources into the power lines increases with the corresponding increase in the share of renewable energy sources. PLC is easily integrated with renewable energy sources as an efficient way to supervise the distribution of energy resources within the power line structure [5].

f) Emerging trends and market drivers

According to Coherent Market Insights, the use of PLC systems has projected values of the global PLC market between 2024 and 2031, ranging from USD 18.87billion to USD23.5billion respectively. This implies a compounded annual growth of 5.1% between 2024 and 2031. This growth is driven by increasing adoption of PLC technology and global initiatives directed towards enhancing efficiency in power distribution networks [6].

1.1. Motivation In Researching On Impulsive Noise Characterization In Broadband PLC

Utility service providers, who are leading the charge in its deployment, are paying close attention to PLC because of the advantages it can offer [7]. A large geographic region is already covered by PLC-based metering devices to create a comprehensive Automatic Meter Reading (AMR) infrastructure, and the deployment of PLC devices to collect energy consumption data from customer locations is growing quickly. In addition to demonstrating utility service providers'

interest in this technology, the widespread usage of PLC-based technologies in recent AMR installations also demonstrates an effective strategy for achieving the objective of developing an Advanced Metering Infrastructure (AMI). A fully functional system will be achieved by utilizing the existing AMR infrastructure and turning it into a strong AMI by adding new, creative methods to identify power outages, creating consumer information systems, improving distributed automation, and being able to identify fraud and demand response management by taking advantage of PLC. It can be difficult to extend the use of PLC-based technology to serve crucial applications, though. PLC must comply with stricter standards than AMR due to the frequency-selective attenuation of communication signals transmitted over power lines, along with the effects of random impulsive noise (IN) and narrowband interference (NBI) present in the power line environment. Consequently, reliable and efficient data transmission requires the use of robust and precise signal processing algorithms designed to address the challenges of such a hostile medium.

This has prompted us to focus on the transmission channel and the characteristics of the interferences affecting its efficient use, with a focus particularly on Impulsive Noise as our main area of research [8].

1.2. PLC Standards and Regulations

For universal applications of PLC, there is a need for proper standardization to enhance the quality of communications. The bit-error-rate (BER) and signal-to-noise ratio (SNR) are two examples of the parameters that need constant and regular monitoring. Because PLC technology is developing so quickly, researchers and non-governmental organizations are establishing guidelines and standards to enhance its quality and interoperability. Making electrical power lines more secure and suitable for the transmission of voice, video, and data information a s the rationale behind this.

The bodies charged with developing and regulating standards in the global telecommunications sector are the International Telecommunication Union (ITU), the European Committee for Electrotechnical Standardisation (CENELEC), the Institute of Electrical and Electronics Engineers (IEEE), the International Electrotechnical Commission (IEC), the International Organization for Standardization (ISO), and the Federal Communications Commission (FCC).

Standards for both broadband and narrowband PLC have been established by all of these organisations. However, for low-speed transmission, the ITU recommends the latter be used in the frequency range of 3–490 kHz. CENELEC is supported by several internal bodies that undertake specialized functions to ensure effective operation. For example, EN50065-1 addresses electromagnetic disturbances, frequency ranges, and general requirements for signaling over low-

voltage electrical networks. The EN55022 standard focuses on high-speed PLC within the 150–500 kHz range, whereas EN50065-1 subgroups primarily deal with narrowband PLC. On the other hand, the IEEE 1901.1 standard targets access communication systems under IEEE patents and is designed for smart grid applications requiring control transmissions below 15 MHz. These standards also define modulation techniques and signal coding schemes. An updated version, IEEE 1901.2, recommends convolutional codes (CC) and Reed-Solomon (RS) coding, and is fully compatible with Internet Protocol version 6 (IPv6). Furthermore, both the ITU and IEC have played major roles in shaping several of these narrowband PLC standards [9].

1.3. Challenges in Powerline Communications

Power line systems face the challenge of not being originally designed for low-frequency data transmission. Unlike dedicated data wiring, their routing is predetermined for power delivery and not known in advance, as the infrastructure was primarily built for electricity transmission.

This means that the system may at times emit significant amounts of energy, either due to external signals or radio frequency interference. A key limitation is that shortwave frequencies are shared by both high-power broadcast services and low-power long-range telemetry. To mitigate interference and frequency-dependent path losses, the HomePlug standard mandates that each node continuously update its "tone maps" during operation.

This enables the device to "learn" which frequencies are problematic and to assign more data to those experiencing minimal loss. While this approach reduces intrusion, it does not provide a straightforward means of instructing a HomePlug device to lower its transmitted interference when sensitive receiving equipment is nearby.

Signal levels in a powerline system are relatively high compared to those received in radio communication devices. Each carrier occupies a 24 kHz channel, with a typical power density of −50 dBm/Hz. Carriers are injected at approximately −6.6 dBm (220 microwatts), giving a total channel power of about 24 dBm (250 milliwatts). In contrast, short-wave radio receivers have sensitivities around −100 dBm (fractions of a picowatt). Consequently, in some regions, proposals have been made to impose legal action on users of power line equipment that interferes with government radio systems [10].

1.3.1. The Power Line Channel as a Transmission Medium

Since the power line carrier was not constructed with data transmission in mind, it offers a hostile environment. The main obstacles are high amounts of frequency-dependent attenuation, a

significant amount of non-white noise, and variation in impedance. The transfer function of a very complex line network is present in the channel that connects any two outlets within a building. Transmission loads of various impedances are present in the several stubs that are utilized. The amplitude and phase response of such a transmission medium typically exhibit significant frequency-dependent variations. On some frequencies, the signal may reach the receiver with very little loss, while on other frequencies, it may be totally distorted. Because network parameters change when devices connected to the network are plugged in or turned off, the channel transfer function itself is time changing [11].

The location of the transmitter or receiver for instance, a power outlet can negatively impact transmission error rates. A receiver positioned near a noise source will have a lower signal-to-noise ratio (SNR) than one placed farther away. In many cases, such noise originates from devices connected to the network. Unlike wireless channels, signal propagation in power lines does not follow a direct line-of-sight path between the transmitter and receiver. The result is that more echoes need to be taken into account. There are some propagation pathways between the transmitter and the receiver, which is why these echoes happen. In the electric circuit network, the signal is reflected due to impedance mismatches along the line [12].

Each multipath component has an associated weighting factor, as it accounts for both transmission and reflection losses. In power line channels, the transmission and reflection parameters are generally assumed to be less than one. Because additional multipath components are generally too weak to contribute significantly, the number of dominant paths considered (N) is usually limited to around five or six. As a result, a path's weighting factor decreases with the number of reflections and transmissions it undergoes. Channel measurements further show that attenuation increases with frequency. Thus, the channel can be described as random and time-varying, with its signal-to-noise ratio (SNR) changing across the transmission bandwidth depending on frequency. Figure 1.3 presents a general channel model of the power line physical layer, spanning the frequency range from 200 kHz to 22 MHz   As frequency rises, the channel demonstrates increased attenuation [13].
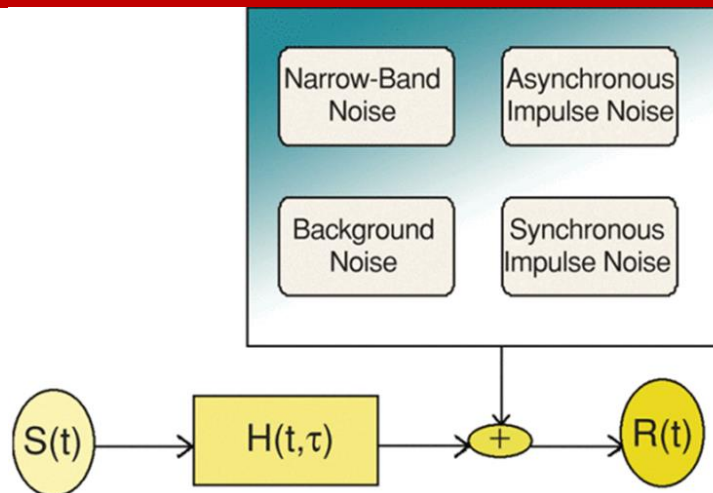
Figure 1.3: The generalized channel model

1.3.2. Classes of Impulsive Noise

To examine the subclasses, pulses and bursts are analyzed sequentially, with the pseudo-frequency of each received signal determined from the peak of its Fourier transform [14], [15], [16].

a) Single pulses

Plotting the pulse's duration and harmonic frequency on the same graph provides an intriguing depiction. The successive pulses, numbered 1 through 1200, are displayed in ascending harmonic frequency sequence in Fig. 1.4. Two kinds of pulses can be distinguished: 1 and 2.
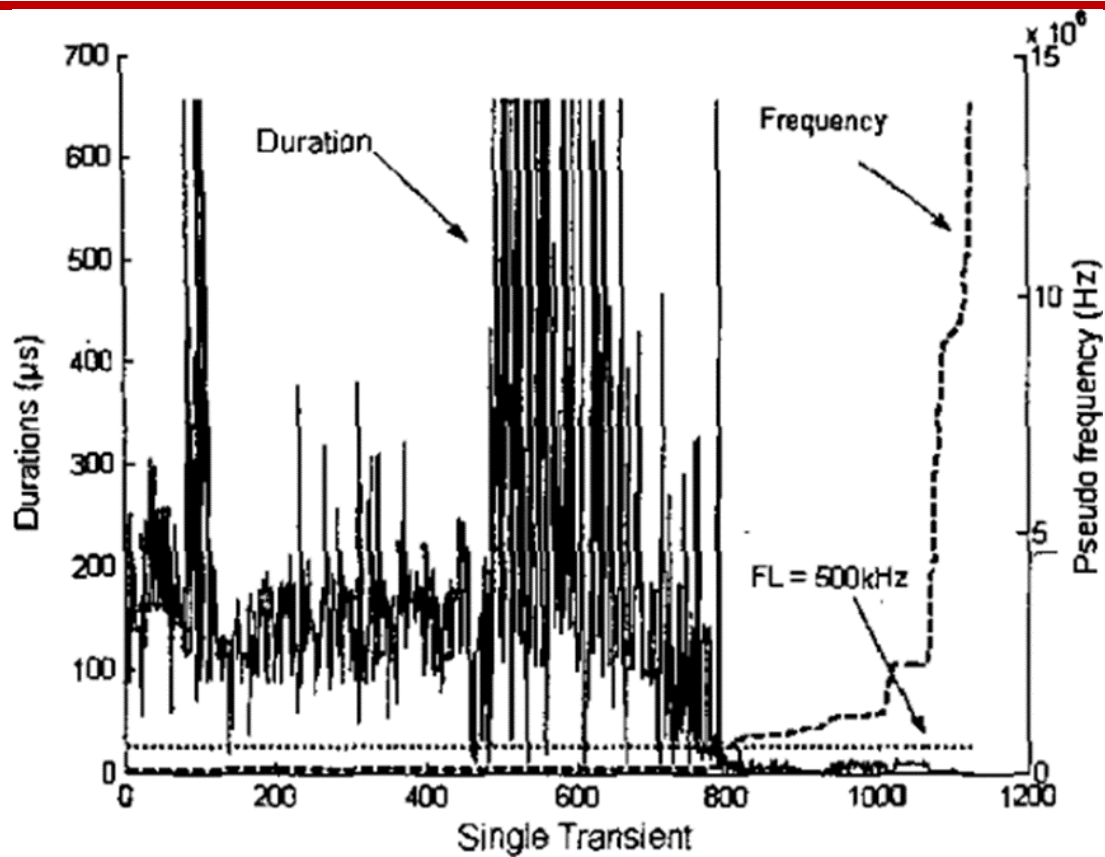
Figure 1.4: Duration and pseudo frequency of single pulses.

In fact, there is a strong correlation between low harmonic frequency values and extended pulse durations; these events will be classified as class 1 (pulses 1 to 800). However, class 2 is associated with short periods and high harmonic frequencies.

Therefore, in order to categorise each event into one of these two types, quantitative criteria must be introduced. It is possible to demonstrate that the harmonic frequency transition between these classes is abrupt by looking at the curves in Fig. 1.4. It seems that determining whether a single pulse's harmonic frequency (f0) is less than or larger than 500 kHz is the simplest method of classifying it as either 1 or 2.

b) Bursts

The 517 events that were categorized as bursts were subjected to the same methodology as before. The findings are shown in Fig. 1.5.
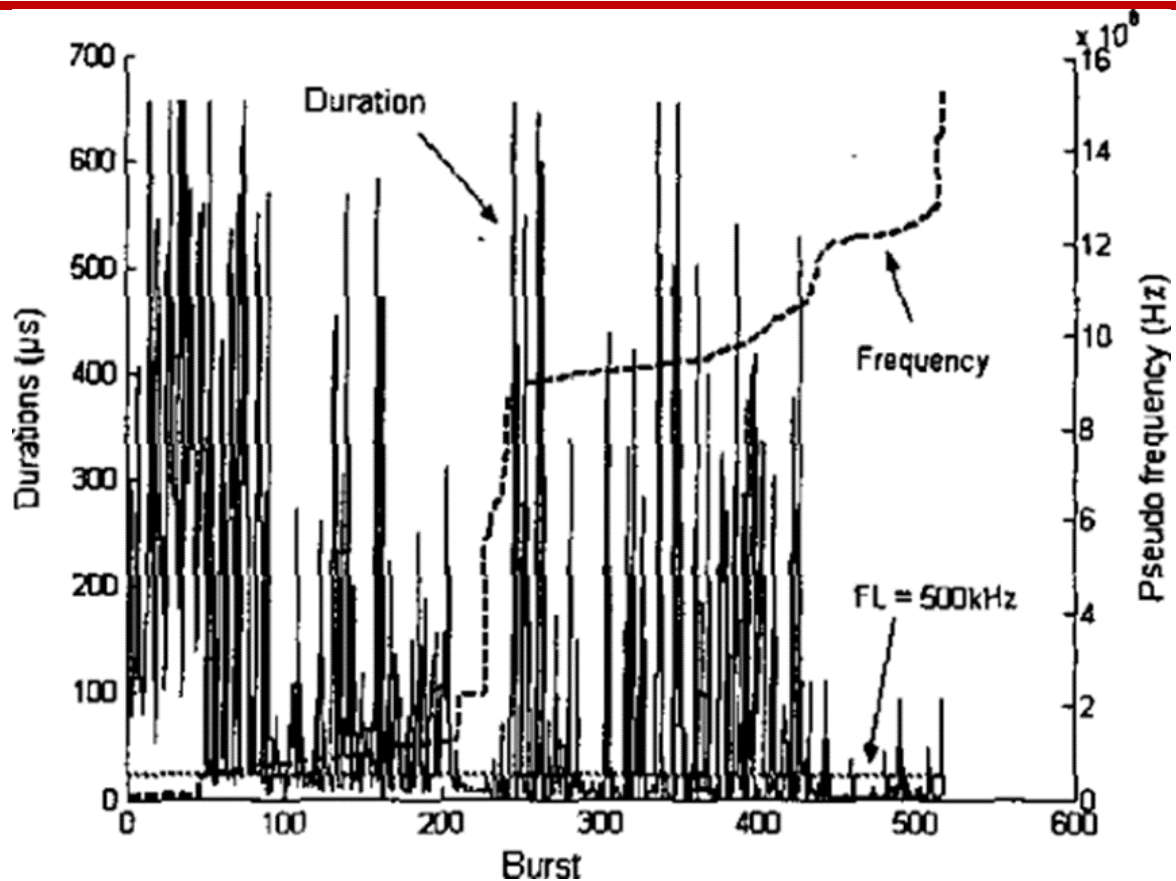
Figure 1.5: Duration and pseudo frequency of the bursts

Initially, it is observed that bursts 1 to 50 display very low harmonic frequencies, centered around 130 kHz, and are characterized by long durations exceeding 50 μs, with an average duration of 310 μs. However, for the remaining events, the correlation between duration and harmonic frequency is not evident. Hence, a more appropriate representation is needed to relate the harmonic frequency f_0 to the number of observed harmonic periods. As illustrated in Fig. 1.6, three separate classes can be distinguished according to the three-step variation of the harmonic frequency f_0.
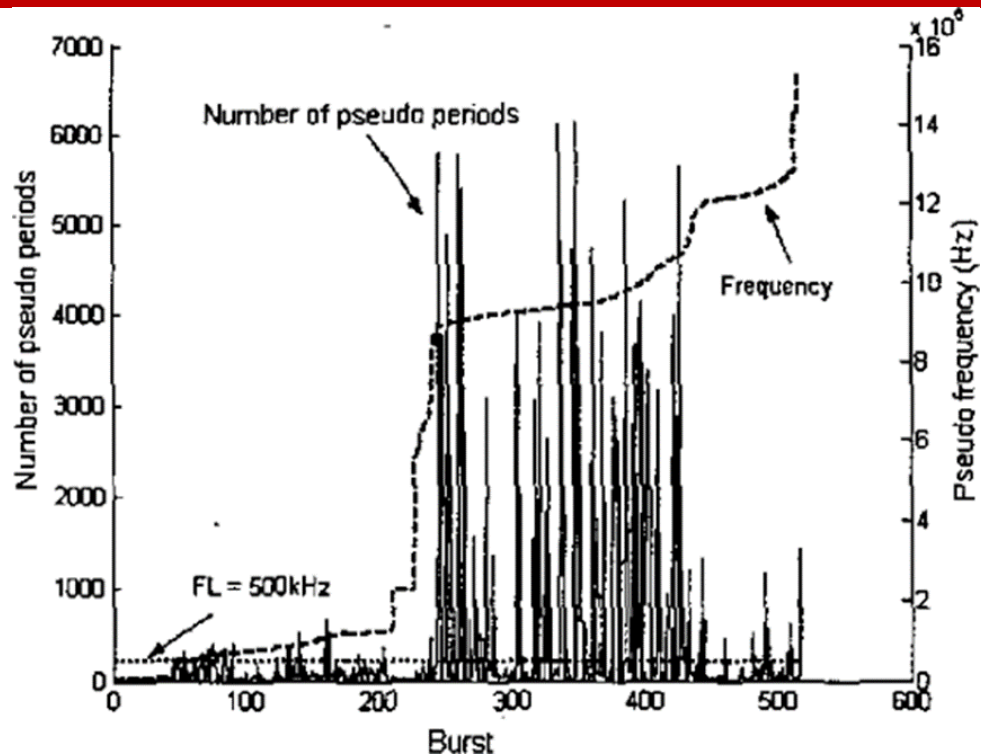
Figure 1.6: Relationship between pseudo-frequency f_0 and number of pseudo-periods per burst

Class 3 refers to bursts with f0<500kHz, characterized by long durations but a small number of harmonic periods, as previously described. Class 4 corresponds to bursts within the range 500 kHz<f0<3 MHz, where the duration decreases while the number of harmonic periods increases. Finally, Class 5 represents bursts with f0>3 MHz, which exhibit a high-frequency content (with a mean value of about 10 MHz) and variable durations or numbers of harmonic periods. Table 1 presents a summary of the different impulsive noise types along with their probabilities of occurrence

Single pulse		
Class 1	Class 2	
$f_0 < 500$ kHz	$f_0 > 500$ kHz	
Pb = 48 %	Pb = 20%	
Burst		
Class 3	Class 4	Class 5
$f_0 < 500$ kHz	500 kHz<f_0<3MHz	$f_0 > 3$MHz
Pb = 3 %	Pb = 11%	Pb = 18 %

Table 1: Classification of impulsive noise types and their occurrence probability (Pb)

The analysis is therefore restricted to impulsive noise with an average frequency content above 500 kHz, as this range falls within the transmission bandwidth of the useful signal. Consequently, the statistical evaluation in Section 1.3 concentrates on Classes 2, 4, and 5.[17].

1.3.3. Impulsive Noise Models

There are two groups of impulsive noise: Natural impulsive noise originates from atmospheric phenomena and solar activity, whereas artificial impulsive noise arises from factors such as switching operations, signal dropouts, or data degradation. Trains of non-overlapping pulses make up artificial impulsive noise, whereas the random superposition of pulses caused by atmospheric influence produces natural impulsive noise. A non-stationary, two-state series of impulses with random amplitudes and positions is how Middleton's model depicts impulsive noise [18], [19], [20].

Middleton provided the first comprehensive model of impulsive noise, characterizing it as a sequence of impulsive or pulsed events that happen at random and change in strength and length over time. Impulsive noise, according to Middleton's model, is a non-stationary, binary-state series of impulses with arbitrary amplitudes and positions [18], [19], [20].

The Symmetric Alpha Stable and Bernoulli Gaussian models are among the most widely applied in studies seeking to match first-order noise statistics with recognized distribution. The following are the most often used models that show up more commonly for impulsive noise modelling:

a) Gaussian Mixture Model

It is possible to observe distinct regions in complex data, some of which have higher probabilities than others. This kind of data complexity is represented by a combination of multiple components, each of which has a straightforward parametric form, like Gaussian. In this instance, it is assumed that every data point is a part of one of the components, and each component's distribution is allocated separately.

The data is thought to come from a mixture of a finite number of Gaussian distributions with unknown parameters in a Gaussian Mixture Model. Within this probabilistic framework, the probability density function (pdf) of the random variable n_k is represented as a weighted sum of several Gaussian distributions.

$$P(n_k) = \sum_{m=0}^{K} P_m \, \aleph(n_k : \mu_m, \sigma_m^2) \qquad (1.1)$$

$\aleph\eta(n_k; \mu_m, \sigma_{m2})$-denotes a Gaussian pdf with mean μ_m, variance, and P_m is the mixing probability of the m-th Gaussian component, which sums to 1, i.e.,

$$\sum_{m=0}^{K} P_m = 1, \qquad 0 < P_m < 1 \qquad (1.2)$$

Various distributions are based on the Gaussian mixture; Middleton Class A and Bernoulli Gaussian models are among these.

b) Middleton Class A Model

For impulsive noise, Middleton put out three statistical models that were characterized by the noise bandwidth in relation to the receiver. These models have been frequently used to solve communication and electromagnetic challenges.

Class C noise is a combination of Class A and Class B noise, with Class A noise having a smaller bandwidth than the receiver and Class B noise having a wider bandwidth. Among these, the "Middleton Class A" model is most frequently employed in communication systems such as PLCs. The number of impulses in an observation period T0, denoted by L in the Middleton Class A model, is thought to follow a Poisson distribution. In other words, this model incorporates the impulse width, making it a variation of the Poison model.

$$PT_0(L) = \frac{(\eta.T_0)^m.e^{-(\eta T_0)}}{L!}$$

$$(1.3)$$

where η is the average number of impulses per second ($T\eta$ is the average number of impulses in the period To). Then, the pdf of a Middleton Class A noise sample n_k is given as below:

$$P(n_k)=\sum_{m=0}^{K} P_m \, \aleph(n_k:\mu_m,\sigma_m^2)$$

$$(1.4)$$

$$P_m = \frac{A^m.e^{-A}}{m!}$$

$$(1.5)$$

The parameter A measures how non-Gaussian the noise is. Index of Impulsivity (non-structure index) The impulse density during the observation time, denoted by A, falls within the range A (0,). Fewer events indicate lower A values, where the instantaneous noise qualities are dominated by the individual events. According to the Central Limit Theorem, the statistics approach the Gaussian distribution as A increases and the noise becomes less organized.

The Gaussian pdf $\aleph\eta(n_k; \mu_m, \sigma_{m2})$ in (4) are zero mean with variance m_2 which is given by

$$\sigma_m^2 = \sigma_I^2 \frac{m}{A} + \sigma_g^2$$

$$(1.6)$$

I is the variance of the impulse noise and g^2 as the variance of the background Gaussian noise. The m-th variance can be written equivalently as

$$\sigma_m{}^2 = \sigma_g{}^2 \{ \frac{m}{Ar^-} + 1 \} = \sigma^2 \{ \frac{m/A + r}{r+1} \} \tag{1.7}$$

The parameter $r = \sigma_g{}^2 / \sigma_I{}^2$ is called the Gaussian factor and gives Gaussian to impulse noise power ratio. $\sigma2 = \sigma_g{}^2 + \sigma_I{}^2$ is the total power of noise.

By tuning its parameters A and Γ the Middleton Class A distribution can represent a wide range of non-Gaussian noise densities. It is worth noting that, for impulsive noise in PLC, Γ typically falls within the range of $[10^{-\text{p}}, 1]$

and

$$A \epsilon [10^{-2}, 1] \tag{1.8}$$

c) Bernoulli Gaussian Model

Another widely used impulsive noise model is the Bernoulli Gaussian model [21]. In this approach, the overall noise sample n_k can be represented as

$$n_k = w_k + i_k$$

where w_k is the white Gaussian background noise and i_k is the impulsive noise sample given by

$$i_k = b_k . g_k \tag{1.9}$$

Since b_k is the Bernoulli process and g_k is complex white Gaussian noise with mean zero, the likelihood of impulsive noise appearing is

$$P(b_k) = \begin{cases} p, & bk = 1 \\ 1 - p, & bk = 0 \end{cases}$$

$$\tag{1.10}$$

In (10), p represents the impulsive bursts probability of occurrence.

The Bernoulli Gaussian noise model is described by the following:

$$p(n_k) = (1 - p).\aleph(n_k ; 0, \sigma_g{}^2) + p. \aleph(n_k; 0, \sigma_g{}^2 + \sigma_I{}^2) \tag{1.11}$$

Where $\aleph(n; 0, \sigma_m{}^2)$

Gaussian noise model is a Gaussian Mixture with two terms.

d) Alpha Stable Model

The Symmetric Alpha Stable distribution is often utilised in impulsive noise modelling, even though the noise models mentioned above are the most widely employed. According to the Central Limit Theorem, as the number of variables goes to infinity, the normalised sum of independent, identically distributed random variables with finite variance converges to a Gaussian distribution. The Generalised Central Limit Theorem states that the sum converges to an Alpha Stable distribution when the finite variance restriction is lifted, permitting both finite and infinite variance.

Alpha stable distributions are rarely widely used because, with rare exceptions, their pdfs cannot be stated in closed forms. Due to the ability to compute with powerful computers, Alpha Stable distributions are currently being employed more and more in PLC noise models. An Alpha Stable random variable's characteristic function defines it:

$$\Phi(u) = \{ \dashv \ (1 + j.\beta.sign(u).tan(\pi\alpha/2 \dashv)\}$$

$$\phi(u) = \begin{cases} \exp\left\{j.\delta.u - \gamma^{\alpha}|u|^{\alpha}\left(1 + j.\beta.sign(u).tan\left(\frac{\pi\alpha}{2}\right)\right)\right\} & \alpha \neq 1 \\ \exp\left\{j.\delta.u - \gamma|u|\left(1 - j.\beta.\frac{2}{\pi}sign(u)\ln|u|\right)\right\} & \alpha = 1 \end{cases} \quad (1.12)$$

where the sign function is defined as

$$sign(u) = \begin{cases} 1, & u > 0 \\ 0, & u = 0 \\ -1, & u < 0 \end{cases} \quad (1.13)$$

The characteristic exponent that governs the tail decays is the stability index α, which falls between 0 and 2. The values of the skewness parameter β are $-1 \leq \beta \leq 1$; 0 for symmetrical distributions, right-skewed distributions, and left-skewed distributions.

Lastly, the random variable is scaled using the scale parameter $\gamma > 0$, and its location is controlled using the shift parameter $\delta \in R$. The mean of an Alpha Stable distribution is $\mu = \delta - \beta.\gamma.tan(\pi.\alpha/2)$ for $1 > \alpha$, but undefined for $1 \leq \alpha$

Similarly, the variance of the distribution is undefined for values of $2 > \alpha$, but for $2 = \alpha$, the variance is $\sigma^2 = 2.\gamma^2$

When $\alpha = 2$, the Gaussian distribution is a particular instance of Alpha Stable distributions. It is typically stated as $0 = \beta$ even though the value of β has no bearing in this case. The Cauchy

distribution with 1=α, 0=β and the Lévy distribution with α=0.5, β=1 are the other special examples. Alpha Stable distributions are taken into consideration for modelling impulsive noise since their tail decay is slow, with the exception of the Gaussian situation.

1.3.4. Time Series Analysis of Impulsive Noise in Power Line Networks

PLC channel noise, where continuous observations are measured at discrete points in time, is modelled using stochastic models. These models are typically called time series models because they officially represent measurement data that is available across discrete time in the form of a time series. Time series analysis is the process of applying time series phenomena to real data. A time series is a collection of observations organized chronologically, and it is important to note the observations' sequence of occurrence [22], [23].

Ignoring this chronological arrangement of the data would result in the loss of a large portion of the time series' information and make it more difficult to predict future event patterns. The resulting time series is referred to as discrete as the data collected for this study are observations made at distinct times.

There are numerous intrinsic benefits to this. First off, the mathematical theory behind the several kinds of stochastic or time series models that may be created for modelling PLC channel noise time series is significantly simplified by the equispaced discrete time. Second, if the data is in the form of a continuous time series, it must be lumped together over specified time intervals in order to be converted to discrete observations [24].

Drawing conclusions about the fundamental characteristics of the stochastic process from the data in the obtained measurement time series is the primary goal of time series analysis. This is achieved by creating a mathematical model that, when fitted to the provided time series, has the same essential statistical characteristics as the stochastic process's producing mechanism.

Currently, time series models have received much attention on addressing the problem of impulsive noise in PLC. A stationary DARMA time series model is applied to model PLC impulsive noise, after it has been made stationary through a developed algorithm. In the same way, a GARCH model is also employed to address the problem of impulsive noise. This is predicated on the volatility clustering observed in PLC noise. In any event, the seasonal behavior that is common in PLC impulsive noise as a feature that cannot be assumed or diminished is not adequately captured by these two-time series models. Thus, measurements-based analysis is one way to increase our understanding of impulsive noise modelling in PLC.

This is carried out for the fundamental properties of PLC impulsive noise in the frequency range of 1 - 30 MHz using ARMA, ARIMA, and SARIMA time series models. The problem of PLC impulsive noise modelling can be more effectively tackled by utilizing these statistical techniques, which improve the scientific process. Exploratory and confirmatory data analysis methods are used when conducting such scientific data analysis utilizing time series models. Exploratory data analysis uses straightforward graphical techniques (autocorrelation functions) to reveal the fundamental statistical properties of the data. A time series model can then be used to explicitly model these at the confirmatory data analysis step [22], [23].

2. Methodology

2.1. Measurement Set-up and Data Processing

Numerous experimental tasks are necessary to characterize impulsive PLC noise, and these tasks can be carried out at the ports to which the primary noise sources or receiver coupler are connected. With the former method, communication is hampered by the general noise in the power line channel. However, by assessing the amount of disturbance each major source of noise contributes to a specific location within the power line network, the latter method allows for the characterisation of the sources. For this investigation, measurement data was collected at specific locations using the former method [25].

2.2 Measurement Set-up
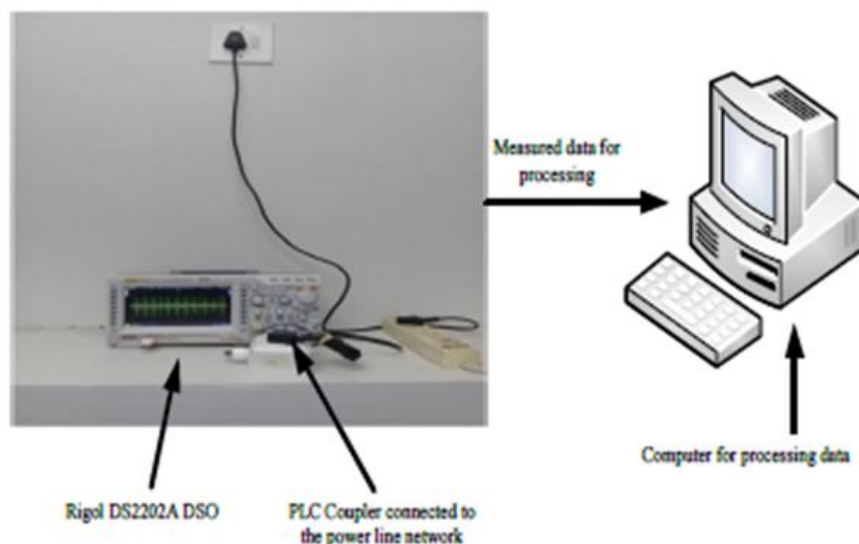
Figure 2.1 PLC noise measurement set up.
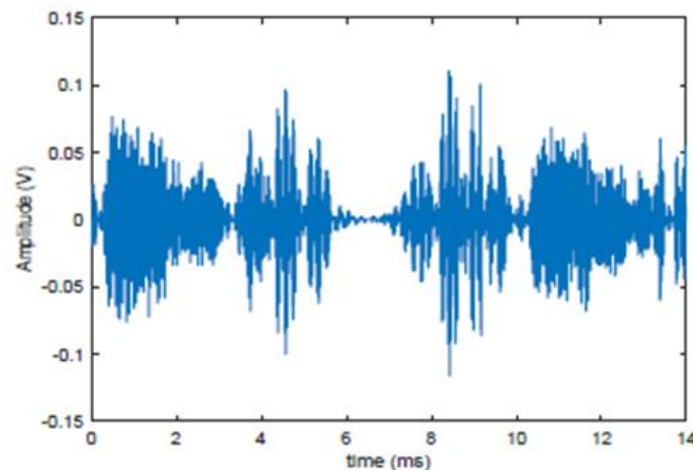
Figure 2.2: A sample measured PLC noise signal

Using the set-up of Figure 2.1, sample measurement data was acquired from diverse locations including residential apartments, offices among other strategic locations. The DSO was set to sample at 50 megasamples per second, resulting in a 0.28-second window length (14 mains cycles). This sampling rate resulted in a window length providing sufficient information on impulsive noise's seasonal behavior.

A lower sampling rate than this value would result in a longer window length, resulting in the loss of the desired seasonality information. On the other hand, to capture adequate information about the seasons in impulsive noise, a higher sampling rate would not provide the desired window length.

According to studies, impulsive noise in PLC systems can originate from a variety of sources, including switched mode power supplies, lightning, thermostats, and other switching phenomena, as well as from the in and out switching of capacitor banks for power-factor correction.

Recent studies have shown that the impulsive noise generated by fluorescent lights can rival the levels of electromagnetic interference. This poses a significant challenge to PLC systems, as the electronic power converters and ballasts within these lights act as noise sources within the 150 kHz to 30 MHz frequency range of the power line channel. Additionally, it has been established that impulsive noise is introduced into the power line network by equipment such as rectifiers in DC power supplies, power switches, power supplies, and other household appliances that employ thyristors or triacs to dim lights. Similar appliances and gadgets are widely present in the measurement contexts that are being studied.

2.3 Differencing Analogy in Processing PLC Noise Data

A non-stationary time series with fluctuating statistical characteristics over brief time intervals is what PLC noise is known as. However, there are situations when assuming that a stationary model can adequately reflect the data is appropriate for shorter sequences. A differencing parameter that corresponds to the integrated component of the model is utilised to handle homogeneous non-stationarity in continuous data; it works similarly to differentiation. For example, consider a continuous time-dependent function given by [25], [26].

$$y_t = \begin{cases} 0 & \text{for } t < T \\ c & \text{for } t \geq T \end{cases}$$

In this case, the constant ccc represents the local level for t > T. When t > T, differentiation removes the local level that the constant ccc introduced, and the derivative dy/dt becomes zero. Consider the second derivative applied to a continuous function of t to see a comparable impact of the differencing operator:

$$y_t = c + bt$$

where b and c are constants. The process yt's linear deterministic trend is formed by the phrase (c + bt). The first derivative value is

$$\frac{dy}{dt} = b \text{ and } \frac{d^2y}{dt^2} = 0.$$

As a result, the first derivative loses the intercept c, while the second derivative gets rid of the linear function. To maintain as much of the data substance as feasible while differencing the data, it is recommended to choose the lowest order of differencing. Error analysis is used to compare the performance of non-differencing, non-seasonal differencing, and seasonal differencing in this paper.

2.4 Theoretical Framework on Time Series Models for PLC Impulsive Noise

PLC noise is a non-stationary time series whose statistical characteristics vary over short intervals. However, for shorter sequences, it may be reasonable to approximate the data using a stationary model. To mitigate homogeneous non-stationarity in continuous data, a differencing parameter associated with the integrated component of the model is applied, functioning in a manner similar to differentiation. In general, impulsive PLC noise has more non-stationary and seasonal features.

As a result, before fitting a stationary ARMA, ARIMA, and SARIMA model, non-seasonal and seasonal non-stationarities must be eliminated using non-seasonal and seasonal differencing operators, respectively [22] [23]

3. Results

Raw data on impulsive noise through a PLC channel for 59 different samples from a secondary source were considered. The samples were analyzed for a period of 14mSeconds each. Each sample resulted in a graphical representation of amplitude in mVolts against time in mSeconds. Below we show impulsive noise characteristics of randomly selected samples (72, 60, 36, 24, and 12), indicating that impulsive noise is intensive in the last mile PLC with extracted bursts of the same.
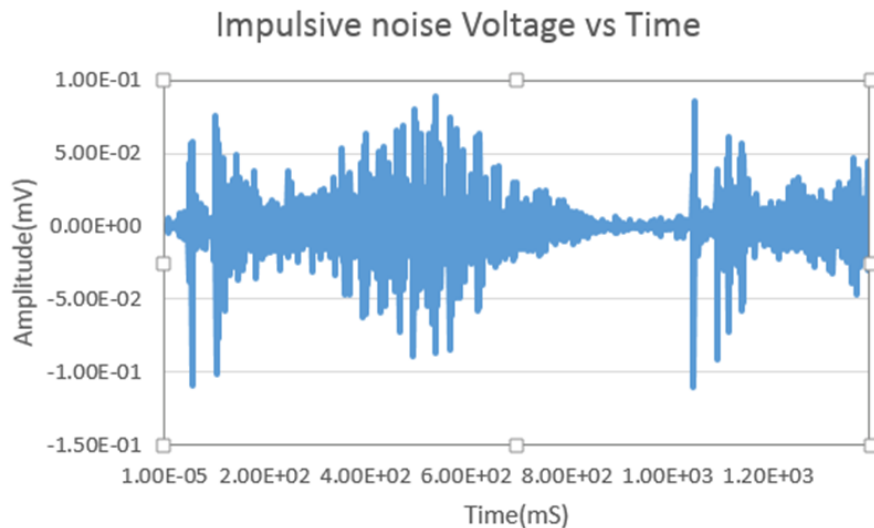
Figure 3.1: sample number 72
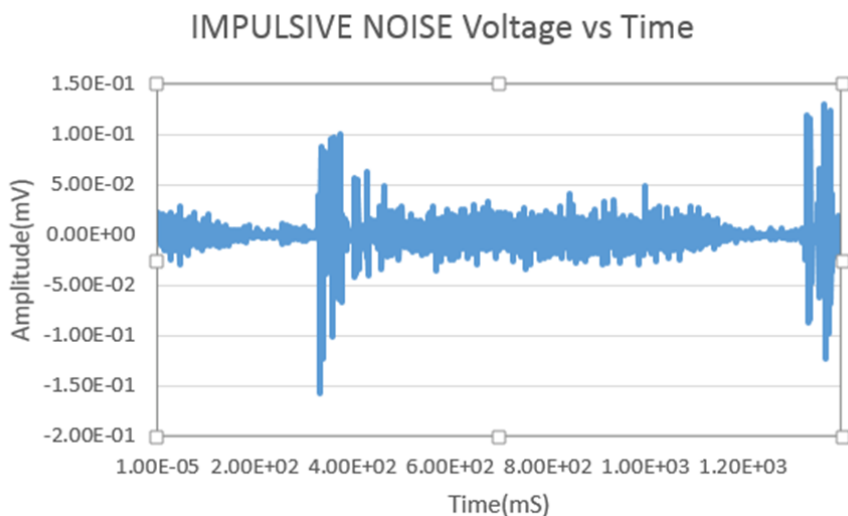
Figure 3.2: Sample number 60
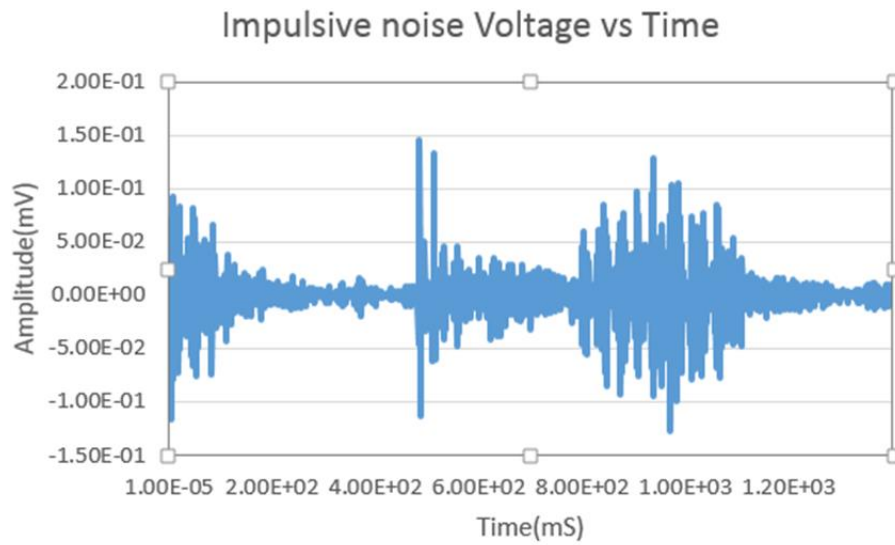
Figure 3.3: Sample number 36
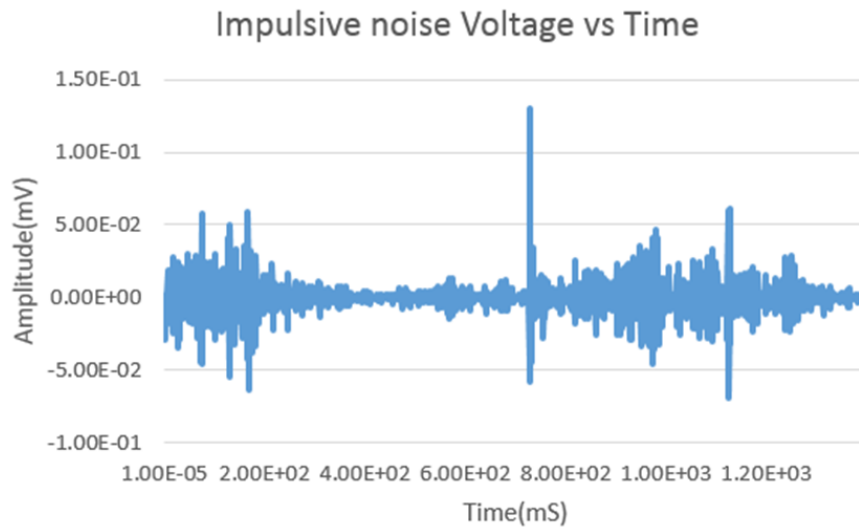
Figure 3.4: Sample number 24
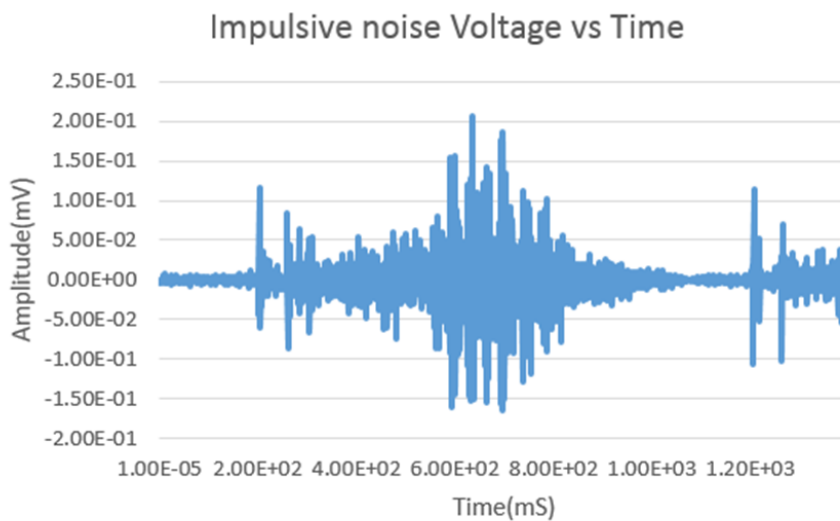
Figure 3.5: Sample number 12

Making deductions about the fundamental characteristics of the stochastic process from the data in the obtained measurements and time series data is the primary goal of time series analysis.

This is done by creating a mathematical model that, when fitted to the provided time series, has the same essential statistical characteristics as the stochastic process's producing mechanism.

In recent years, time series models have gained considerable attention in tackling impulsive noise in PLC. A stationary DARMA time series model has been applied for this purpose, following the development of an algorithm that renders the impulsive noise stationary. Similarly, a GARCH model has been used, based on the principle that PLC noise demonstrates volatility clustering. However, both of these models fail to capture the seasonal behavior inherent in PLC impulsive noise a critical characteristic that cannot be overlooked or simplified. Consequently, this study advances impulsive noise modeling in PLC through a measurement-based analysis approach.

ARMA, ARIMA, and SARIMA time series models are used to analyse the basic characteristics of PLC impulsive noise in the frequency range of 1 to 30 MHz. By improving the scientific approach, these statistical techniques enable the urgent issue of PLC impulsive noise modelling to be resolved more quickly and effectively. Both exploratory and confirmatory data analysis tools are employed when undertaking such scientific data analysis involving time series models.

Exploratory data analysis uses straightforward graphical techniques (autocorrelation functions) to reveal the fundamental statistical properties of the data. Time series models can then be used to explicitly represent these at the confirmatory data analysis step.

4. Discussion

Drawing conclusions about the fundamental characteristics of the stochastic process from the data in the obtained measurement time series is the primary goal of time series analysis. This is achieved by creating a mathematical model that, when fitted to the provided time series, has the same essential statistical characteristics as the stochastic process's producing mechanism.

Time series models have recently attracted significant attention for addressing impulsive noise in PLC. In this context, a stationary DARMA model is applied once an algorithm has been used to render the impulsive noise stationary. Likewise, a GARCH model is employed, leveraging the idea that PLC noise displays volatility clustering. However, both approaches fall short in capturing the seasonal behavior characteristic of PLC impulsive noise a fundamental property that cannot be ignored or simplified.

Therefore, in a real effort to improve our comprehension of impulsive noise modelling in PLC, measurements-based analysis is the method employed in this content. The fundamental properties of PLC impulsive noise in the frequency range of 1 to 30 MHz are analyzed using the ARMA, ARIMA, and SARIMA time series models. These statistical techniques provide a more rapid and efficient resolution of the pressing problem of PLC impulsive noise modelling by enhancing the scientific approach.

Both exploratory and confirmatory data analysis tools are employed when undertaking such scientific data analysis involving time series models.

Exploratory data analysis uses straightforward graphical techniques (autocorrelation functions) to reveal the fundamental statistical properties of the data. Time series models can then be used to explicitly represent these at the confirmatory data analysis step.

5. Conclusion

In order to assess the noise in the time domain for an indoor power line communication system, we put up a measurement system design in our research. Based on its amplitude and the intervals between impulses, the statistics of impulsive noise in PLC were recorded. The findings of this study are consistent with those of earlier research that assessed noise in PLC. These were contrasted with the findings of previous literature reviews. The variations may be due to the fact that electrical networks have quite different physical properties and structures.

The difference between the durations and the mean and standard deviation of the amplitudes is rather substantial.

We came to the conclusion that the noise durations and amplitudes are fairly large. Large transients, equipment voltage spikes, lightning, electromagnetic interference on the network, and unidentified features of the power cables are the causes of the noise signals' extremely high amplitude. It is evident from the noise PSD that the most severe noise disruptions are caused by the generated noise.

The switching instances, which are typically unpredictable, determine these disruptions. Indoor PLC networks suffer greatly as a result of the extremely high and irregular noise in power line networks.

Impulsive noise characteristics are used to compare noise obtained in various places between 30 and 500 kHz based on fundamental features in the frequency and temporal domains. We

demonstrate that the noise level in the entire frequency band, NBI, is higher when measured in the last mile. MCA and the α-stable distribution model are used to further construct impulsive noise models. Given that the α-stable distribution model fits noise better, this can be considered white noise in the frequency range above 50 kHz.

References

[1] M. S. Yousuf, S. Z. Rizvi, and M. El-Shafei, "Power Line Communications: An Overview - Part II," in *2008 3rd International Conference on Information and Communication Technologies: From Theory to Applications*, Apr. 2008, pp. 1–6. doi: 10.1109/ICTTA.2008.4530268.

[2] A. S., S. E., and A. EL-Sayed, "A Survey of Wireless Sensor Network Attacks," *Commun. Appl. Electron.*, vol. 6, no. 10, pp. 10–20, Apr. 2017, doi: 10.5120/cae2017652565.

[3] A. Majumder and Jr. Caffery J, "Power line communications," *IEEE Potentials*, vol. 23, no. 4, pp. 4–8, Oct. 2004, doi: 10.1109/MP.2004.1343222.

[4] "What Is Power Line Communication (PLC)?," Nessum Alliance. Accessed: Jul. 09, 2025. [Online]. Available: https://nessum.org/media/technology-blog/what-is-power-line-communication

[5] M. K. Andari and A. A. Beheshti, "Pilot Based Channel Estimation in Broadband Power Line Communication Networks," *Commun. Netw.*, vol. 4, no. 3, Art. no. 3, Aug. 2012, doi: 10.4236/cn.2012.43028.

[6] A. R. Ndjiongue and H. C. Ferreira, "Power line communications (PLC) technology: More than 20 years of intense research," *Trans. Emerg. Telecommun. Technol.*, vol. 30, no. 7, p. e3575, Jun. 2019, doi: 10.1002/ett.3575.

[7] H. Gassara, F. Rouissi, and A. Ghazel, "Narrowband stationary noise characterization and modelling for power line communication," in *2013 13th International Symposium on Communications and Information Technologies (ISCIT)*, Sep. 2013, pp. 148–153. doi: 10.1109/ISCIT.2013.6645840.

[8] "RECOMMENDATION ITU-R P.1410-5 - Propagation data and prediction methods required for the design of terrestrial broadband radio access systems operating in a frequency range from 3 to 60 GHz".

[9] "(PDF) IEC STANDARDS FOR PLC," ResearchGate. Accessed: Jul. 09, 2025. [Online]. Available: https://www.researchgate.net/publication/271966762_IEC_STANDARDS_FOR_PLC

[10] Y. Hao, C. Zhou, X. Zhang, D. Zhao, F. Li, and H. Wang, "Power Line Communication Challenges in the Energy Internet," *IOP Conf. Ser. Earth Environ. Sci.*, vol. 645, no. 1, p. 012079, Jan. 2021, doi: 10.1088/1755-1315/645/1/012079.

[11] M. Korki, "Power Line Communication Channel Modelling and Performance Evaluation".

[12]   "Data Transmission Media," CoLab. Accessed: Jun. 25, 2025. [Online]. Available: https://colab.ws/articles/10.1016%2FB0-12-227410-5%2F00165-4

[13]   "RECOMMENDATION ITU-R P.1410-5 - Propagation data and prediction methods required for the design of terrestrial broadband radio access systems operating in a frequency range from 3 to 60 GHz".

[14]   V. Degardin, M. Lienard, A. Zeddam, F. Gauthier, and P. Degauquel, "Classification and characterization of impulsive noise on indoor powerline used for data communications," *IEEE Trans. Consum. Electron.*, vol. 48, no. 4, pp. 913–918, Nov. 2002, doi: 10.1109/TCE.2003.1196420.

[15]   O. Karakuş, E. E. Kuruoğlu, and M. A. Altınkaya, "Modelling impulsive noise in indoor powerline communication systems," *Signal Image Video Process.*, vol. 14, no. 8, pp. 1655–1661, Nov. 2020, doi: 10.1007/s11760-020-01708-1.

[16]   F. Chelangat and T. J. O. Afullo, "Modelling of the Powerline Communication Bursty Impulsive Noise," in *2023 Photonics & Electromagnetics Research Symposium (PIERS)*, Prague, Czech Republic: IEEE, Jul. 2023, pp. 1450–1455. doi: 10.1109/PIERS59004.2023.10221275.

[17]   J. A. Roberts, "Solar Radio Bursts of Spectral Type II," *Aust. J. Phys.*, vol. 12, no. 4, pp. 327–356, 1959, doi: 10.1071/ph590327.

[18]   T. Shongwe, A. J. H. Vinck, and H. C. Ferreira, "A Study on Impulse Noise and Its Models," *SAIEE Afr. Res. J.*, vol. 106, no. 3, pp. 119–131, Sep. 2015, doi: 10.23919/SAIEE.2015.8531938.

[19]   S. M. Çürük, "Impulsive Noise Models Used in Power Line Communications," *Balk. J. Electr. Comput. Eng.*, vol. 7, no. 2, pp. 115–122, Apr. 2019, doi: 10.17694/bajece.457393.

[20]   F. H. Juwono, Q. Guo, D. Huang, K. P. Wong, and L. Xu, "Impulsive noise detection in PLC with smoothed L0-norm," in *2015 IEEE International Conference on Acoustics, Speech and Signal Processing (ICASSP)*, South Brisbane, Queensland, Australia: IEEE, Apr. 2015, pp. 3232–3236. doi: 10.1109/ICASSP.2015.7178568.

[21]   W. Finamore, M. Pinho, M. Sharma, and M. Ribeiro, "Modeling Noise as a Bernoulli-Gaussian Process," *J. Commun. Inf. Syst.*, vol. 38, pp. 175–186, Nov. 2023, doi: 10.14209/jcis.2023.20.

[22]   S. O. Awino, T. J. O. Afullo, M. Mosalaosi, and P. O. Akuon, "Time Series Analysis of Impulsive Noise in Power Line Communication (PLC) Networks," *SAIEE Afr. Res. J.*, vol. 109, no. 4, pp. 237–249, Dec. 2018, doi: 10.23919/SAIEE.2018.8538337.

[23]   F. Chelangat and T. J. O. Afullo, "Time Series Modelling of Powerline Communication Impulsive Noise: Queuing Theory Approach," *Prog. Electromagn. Res. C*, vol. 150, pp. 157–168, 2024, doi: 10.2528/PIERC24090401.

[24]   S. Kumaresan, "Stochastic Approaches in Time Series Forecasting," Medium. Accessed: Jun. 25, 2025. [Online]. Available: https://medium.com/@sundharesansk11/stochastic-approaches-in-time-series-forecasting-ea6e2fe41836

[25]   S. O. Awino, T. J. O. Afullo, M. Mosalaosi, and P. O. Akuon, "Measurements and Statistical Modelling for Time Behaviour of Power Line Communication Impulsive Noise," *Int. J. Commun. Antenna Propag. IRECAP*, vol. 9, no. 4, p. 236, Aug. 2019, doi: 10.15866/irecap.v9i4.16094.

[26]   S. P. Affek, "Stationarity in time series analysis," TDS Archive. Accessed: Jun. 25, 2025. [Online]. Available: https://medium.com/data-science/stationarity-in-time-series-analysis-90c94f27322

[27]   P. J. Brockwell and R. A. Davis, *Time Series: Theory and Methods*. Springer Science & Business Media, 1991.

Simulation of Solar PV Systems using Enhanced SPECA Modelling Tool

S. K. Kibaara

Department of Electrical and Electronics Engineering, Technical University of Mombasa, Mombasa, Kenya

Email: samuelkariuki@tum.ac.ke

Abstract

Solar energy is becoming a key contributor to the global transition from conventional energies to non-conventional energy sources. Implementation of energy sources like solar involves a complicated trade-off between technical, economic, environmental and social factors. Modelling tools are therefore required to provide an in-depth set of criteria across the technical, economic, environmental and social dimensions. To provide adequate information for decision makers, solar energy modelling tools are required to provide vital information such as the direct normal irradiation, capacity factor, land slope and topography, grid accessibility and technology maturity and efficiency, the capital investment cost (CAPEX) and the discount rates, the cost of energy produced (Levelised Cost of Electricity - LCOE), operational and maintenance costs (OPEX), the land use impacts which include habitat disruptions, biodiversity and ecosystem impacts, carbon footprint and lifecycle emissions which include manufacturing emissions of carbon dioxide, social acceptance, job creation potential, policy support and the alignment with energy strategies of the country. As a matter of fact, modelling of an energy system should capture externalities, both positive and negative, that will provide a detailed assessment of the actual economic and societal costs and the overall Levelised Cost of Electricity. By incorporating these externalities, an energy modelling system will provide the true cost of energy that will offer incentives to investors and enable policymakers to align countries with the appropriate energy investment strategies which may include provision of subsidies and tax reliefs. This paper will present a review of the techno-economic modelling tools for solar energy, identifying their gaps, and propose modifications to the LCOE calculations that will provide a realistic cost of solar energy by incorporating externalities, in order to understand the capabilities of these solar energy modelling tools. The proposed modification of the LCOE methodology herein referred to as Solar PV based Power and Environmental Costing Assessment tool (SPECA) modelling tool is used to model a PV system and validated against other modelling tool. The LCOE values of HOMER and SAM are 36.85% and 53.98 % lower as compared to that of the SPECA modeling tool.

Key words: Levelised Cost of Electricity, Externalities, Environmental Impacts, Life Cycle Cost

1. Introduction

As the global population and living standards increase, the demand for energy is also rising. Kenya is rapidly developing its Renewable Energy Sources to reduce its over-reliance on fossil fuels[1]. For example, geothermal energy has contributed immensely to the overall electricity capacity, increasing from 13% in 2011 to 26% in 2015, while hydropower and fossil fuel-based power each add 36% to the energy system. Wind energy, cogeneration and solar PV contribute the remaining 2% with an annual growth rate of approximately 2.25% [2]. This increase in energy demand must be met sustainably, without compromising the ecosystems, and also be capable of meeting the energy needs of future generations. The immediate and future challenge has been, and will always be, meeting the energy needs of the ever-growing populations at the lowest possible cost, without impacting the environment and human health. Techno-economic modelling tools are utilised to assess the viability of the energy resources prior to the power plant's construction, in order to estimate the plant's performance, the likely pollutants it will emit, and the overall energy cost,to determine the plant's feasibility. Many of these tools employ the Levelised Cost of Energy (LCOE) as a comparative metric to assess the feasibility of different energy power plants, in relation to their lifetimes, cost structures, and capacity factors, from an economic perspective [3]. LCOE is utilized by power producers as a utility factor to estimate the cost of power produced by any power plant [4]. The calculations to arrive at this factor take into consideration all the expected lifetime costs of the power plant, including but not limited to all taxes, fuel costs for conventional energy power plants, capital expenditure for the project, incentives in the form of grants, inflation rate, operations and maintenance costs, and insurances, divided by the discounted energy production from the power plant [5]. A low LCOE indicates a low unit cost of energy, whilst a high LCOE indicates a higher unit cost of energy. In numerical form, LCOE can be expressed as:

$$LCOE = \frac{C_a}{P_a}$$

Where P_a is the annual power output in kWh.

C_a is the equivalent annual lifecycle cost of the power plant.

$$C_a = \left(C_{cap} + C_{pe}\right)\left[\frac{i(1+i)^N}{(1+i)^N - 1}\right]$$

Where C_{cap} is the cost of the equipment, land, construction and installation, testing and commissioning of the plant and C_{pe} is the cost additional to the capital cost to find out the total present value of cost over the lifetime of the power plant.

2. Materials and Methods

2.1. Included models

A lot of work has gone into the development of Solar PV modelling tools. To ensure that only the most recent and active tools are analysed, a criterion is set that each of the modelling tools will have been used in a publication after 2017 and that the tools must be active. Since the modelling tools are continuously being updated and others are being developed, to ensure that only current information is provided in this paper, the developers' websites will be accessed to note any recent updates to the modelling tools so that the modelling tools can be validated.

2.2. Modelling tools features and properties

The model categorization consists of the capabilities of the modelling tool in conducting technical, economic, environmental and social parameters of Solar PV energy system. This assessment will enable us to determine whether the tool is capable of assessing the solar PV in all the four parameters. Energy modelling tools are developed to solve problems like power system analysis, operation decision support and investment decision support and the investigation of future energy scenarios.

Techno-economic analysis of power generation systems gives great insights into the economic viability of the power system to be designed and constructed. Due to the great importance of these tools in modelling, simulation and techno-economic analysis, there has been a number of studies that have attempted to assess the capability of these tools. These reviews have evaluated the features of the techno-economic tools with each of these tools having unique features tailored to meet specific objectives in techno-economic study of power generation system[5]. [6] has reviewed 68 techno-economic tools based on their capabilities to simulate, create scenarios, create equilibriums, carry out top-down analysis, carry out bottom up analysis, optimize operations and optimize the energy investments and finally analyzed and described in detail and in collaboration with developers 37 of these tools for the renewable energy penetration into the grid. [13] noted that there is no single computer tool that can meet all requirements in an energy system but each tool is only able to meet a specific objective for a specific energy scenario. The main objective of this study was to come up with an ideal tool that could be used to highlight the effects of renewable energy integration into different energy systems through modelling. It was concluded that the wide range of these tools in use differ significantly in terms of the regions they analyse, the technologies they consider, and the objectives they fulfil [6].

Additionally, studies on the capabilities of standalone tools like EFOM, MARKAL, MOREHyS (Based on BALMOREL tool), Invert and UREM were discussed [7], [9] respectively [8] indicated

that although energy system optimization models (ESOMs) have provided direction on how to handle energy policies and effects to the climate, the uncertainties within the model structures and the inputs these models are not adequately addresses or ignored altogether.

Among these tools employed for techno-economic analysis are the Hybrid Optimization for Modeling Electrical Renewables (HOMER) , RETScreen Expert, SAM, Aeolius, EnergyPLAN, EnergyPro, MARKAL/Times, ETEM, Modest, Sifre, LEAP, BCHP Screening Tool, HYDROGEMS, and TRNSYS16 and many more [10]). There are quite a number of software tools that can be used to optimize and simulate energy systems [11]. HOMER and RETScreen are the most popular Techno-Economic tools. HOMER has the capacity of simulating and optimizing renewable power systems in standalone or grid linked configurations the purposes of determining the cost effectiveness of the power plants [20]. This tool can be used to evaluate stand-alone power generation systems as well as grid connected systems in remote areas, islands and buildings to summarize their environmental, technical and economic benefits with a main objective of minimizing Net Present Costs (NPC)(Ma, Xue and Liu, 2018) [13]. Homer optimizes the system components of the power system to provide energy cost but does not look at all the costs associated with civil and structural work, installation and operation [12]. RETScreen is a project analysis and decision support tool developed by Natural Resource Canada. RETScreen does not provide renewable energy system optimization rather it analyses the energy scenario provided that the energy mix input is provided by the user and pro- vides detailed cost analysis, financial analysis and emission analysis [19].

[16] Used, HOMER which can be used for both standalone and grid connected systems to optimize system energy systems and RETScreen that can analyse energy scenarios in an energy system, the two most favorite modeling softwares to model and simulate a hybrid energy system to assess the cost effectiveness of these HES in electrical power production. Salehin et al., 2016 employed Homer to optimize the HES components, LCOE and RE penetration into power systems. In their paper, necessary information was provided for identification of appropriate energy tool for different application in modelling. The following section discusses the development of a SolarPV based Power and Environmental Costing Assessment tool (SPECA) modeling tool. This involves the mathematical derivation of the solar photovoltaic systems, cost modeling of the different solar, quantification and monetization of externalities and finally tying all these components to make the new SPECA modeling tool. Chapter four applies the SPECA modeling tool to perform some case studies of the different regions to show the capability and working principle of the tool.

3. Formulation Of The SPECA Modelling Tool

The central block diagram of the solar PV based Power and Environmental Costing Assessment tool (SPECA) is shown in Figure 1. The inputs to this tool include the location, Direct Normal Irradiation (DNI), load data, environmental and non-environmental data, components, and their respective cost characteristics and the energy model of solar PV. The SPECA tool analyses and computes the input data yielding the total system output which includes the LCOE, Net Present Cost (NPC),IRR, cash inflow, cash outflow and the total energy output.
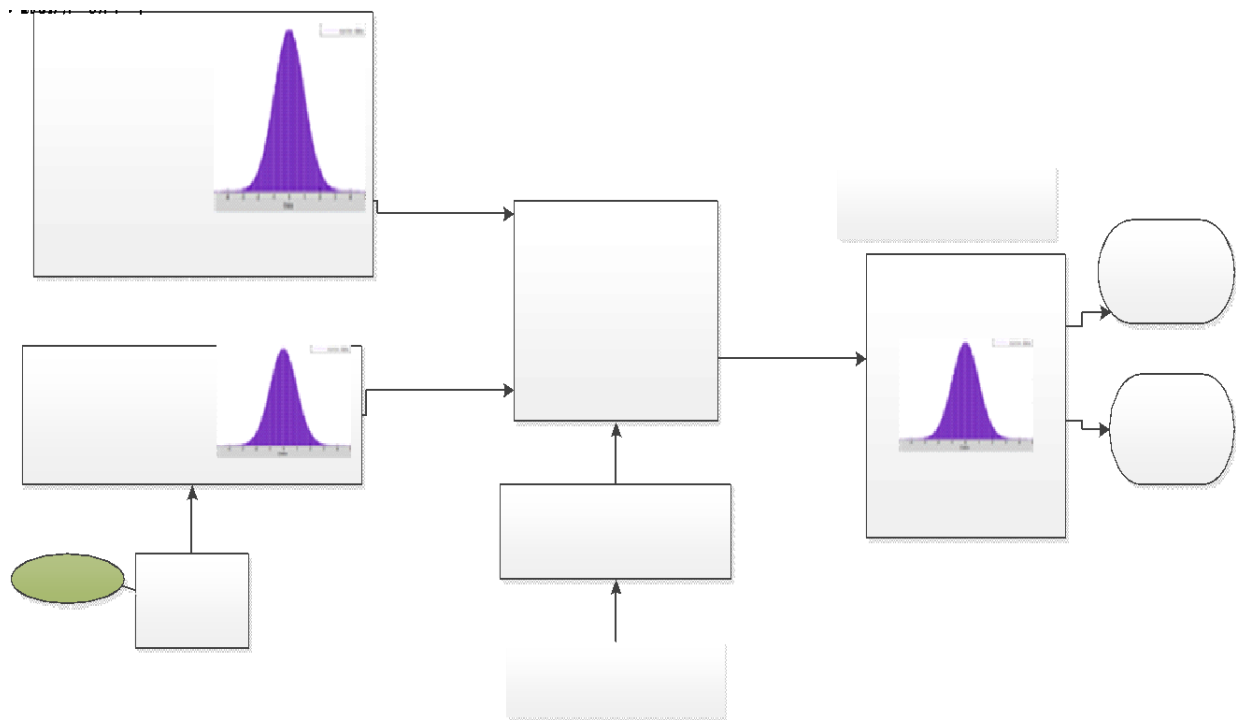
Figure 1: Main Block Diagram of the SPECA Model

As discussed in previous chapters, the tool is developed overcome the failure of other tools to include the environmental impacts of Solar PV in the determination of the system metrics such as annual energy generated in a given region, Energy payback time, Net present value, Levelized cost of electricity, Levelised Externality Cost of Energy (LECOE) and Levelised Total Cost of Energy (LTCOE). LTCOE defines the amount of money paid per kWh of energy when externalities are incorporated while LECOE defines the externalities per kWh of energy generated. The SPECA modeling tool is implemented using basic visual programming. A graphical user interface (GUI) provides an interactive user platform. The Structured Query language (SQL) is used for database development. The SPECA modeling tool, therefore, has the Graphical user interface (GUI) and the database. The GUI is window based and provides functions to manipulate the data according to the requirements. The interface calls stored procedures in the database for data processing and

data retrieval. Finally, the database keeps all system data enhancing data integrity. The database used is a relational database management system, which is a Microsoft SQL Server. The database stores the tabular files of DNI, the cost of equipment used for solar photovoltaic and their types, different environmental aspects of the other regions in Kenya. The process flow diagram of the SPECA model is described by Figure 2.
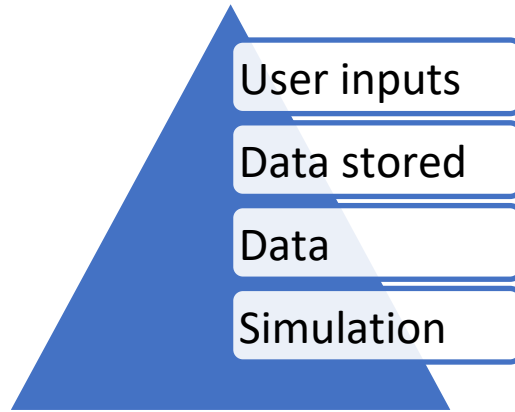
Figure 2: SPECA Model System Architecture

3.1. SPECA Modelling Tool Formulation

The SPECA modeling tool is a mathematical development that utilizes the LCOE methodology. From the first principles, LCOE is expressed as a fraction of the total costs the lifetime energy production as described by Equation (1).

$$LCOE = \frac{Total\ life\ cycle\ \cos t}{life\ time\ energy\ production} \tag{1}$$

To capture the Externality Cost (EC) of solar PV, the LCOE methodology is further restructured to yield the Levelised Total Cost of Energy (LTCOE) as defined by Equation (2). The difference between LTCOE and LCOE in this paper is referred to as Levelised Externality Cost of Energy (LECOE) as defined by Equation (2).

$$LTCOE = \frac{\sum_{t=0}^{T} \frac{C_0 + O\&M_t + RC_t + RV}{(1+r)^t} + \frac{\sum_{i=1}^{k} EC}{(1+r)^t}}{\sum_{t=1}^{T} \frac{E_0(d)^t}{(1+r)^t}} \tag{2}$$

$$LECOE = \frac{\sum_{t=0}^{T}\frac{C_0 + O\&M_t + RC_t + RV}{(1+r)^t} + \frac{\sum_{i=1}^{k}EC}{(1+r)^t}}{\sum_{t=1}^{T}\frac{E_0(1-d)^t}{(1+r)^t}}) - (\frac{\sum_{t=0}^{T}\frac{C_0 + O\&M_t + RC_t + RV}{(1+r)^t}}{\sum_{t=1}^{T}\frac{E_0(1-d)^t}{(1+r)^t}}) \qquad (3)$$

Where $\sum_{i=1}^{k}EC$ represents the aggregated environmental and non-environmental impacts the cost of the USSE and k represents the affected impacts

3.2. Structure of the SPECA Modelling Tool

The SPECA modeling tool developed is used for sizing and determining the economic viability of Solar PV systems in a given location. The input parameters to the SPECA modelling tool includes weather data, load demand, ecosystem goods and services, and the solar photovoltaic component characteristics and costs. After computation, the software results output includes energy generated, LCOE, net present value (NPV), number of panels used, the total area occupied by the plant and the BOP and the number of batteries. The SPECA modeling tool incorporates and synthesizes the externality cost of solar photovoltaics. The SPECA modeling tool most outstanding achievement is its ability to incorporate the externalities (associated environmental costs) in the output metrics herein referred as LECOE and LTCOE. The user guide of the SPECA modeling tool is described in Appendices.

4. Baseline Results

The SPECA modeling tool demonstrated through simulations how monetization and incorporation of externalities of USSE was achieved using the advanced LCOE methodology. The externalities that have been monetized and incorporated in the modeling of Solar PV using the SPECA modeling tool are divided into two major categories, that is, techno-economic indicators and the environmental indicators as shown in Table 1. The Techno-economic indicators measure the performance of the plant, anticipated costs incurred by investors of USSE and the surrounding communities. On the other hand, the environmental indicators reflect the externalities of USSE, which were quantified and monetized in this paper.

Table 1: Techno-Economic and Environmental Indicators

Techno-Economic indicators	Environmental Indicators
● Energy Generated in the whole lifespan	● Water pollution
● Cost of energy production	● Fatalities and morbidity
● Levelised cost of electricity (LCOE)	● Ecosystems service loss

Techno-Economic indicators	Environmental Indicators
- Levelised externality cost of electricity - Net present value - PV externality cost	Total emissions

As earlier explained in Chapter Three, the SPECA modeling tool is a techno-economic assessment of the viability of utilization of solar energy in the different regions of Kenya. Therefore, the software generates results according to the inputs given, including the location, Solar PV components, land use type and the biodiversity type. Accordingly, results from the SPECA modeling tool are achieved through case studies of the different regions incorporated in the tool. Section 0 discusses two case studies done using the SPECA modeling tool for simulating and sizing of Solar PV for Lodwar, Turkana county, and Mahiga; Nyeri County.

4.1. SPECA Modelling Tool Application and Results of Lodwar and Nyeri Kenya

4.1.1. Electricity production

Several factors influence the amount of electricity generated, which includes plant availability hours, load factor, idle capacity, BOP and plant capacity. An increase in the load factor, availability hours, and plant capacity positively affect power generation. On the other hand, an increase in idle capacity and BOP affects electricity generation negatively. In coming up with the SPECA modeling tool, the load factor was assumed to be 25%, while the BOP was considered to be 20% [130], which is mainly applied in many photovoltaic studies. Among other metrics, the SPECA modeling tool calculates for a lifespan of 25 years assumed in this work are the yearly energy generated, LTCOE, LCOE, LECOE, cash flows, area occupied, number of batteries, and the number of solar panels as shown in Table 2. As shown by Figure 3, the yearly energy delivered varies according to the DNI, estimated at an average of 1800kWh/m2/yr. The cumulative energy production in Turkana for the lifespan of 25 years was 790,338.201 MWh. The area required for installation to meet the electricity demand was estimated to be 194594.6 m2 of land that required about 116,944 solar photovoltaic panels and 13350 batteries for an estimated load of 2000 houses.

Table 2: Comparison of Electricity production and land use factor for Mahiga and Lodwar

Location	Cumulative energy delivered (MWh)	No of solar photovoltaics	Number of batteries	The area occupied (m^2)	DNI kWh/m^2/yr
Gatarakwa, Nyeri County	505,617.549	116,944	13350	222,144	1600

Lodwar, Turkana County	790,338.201	70894	20025	194,594	1800
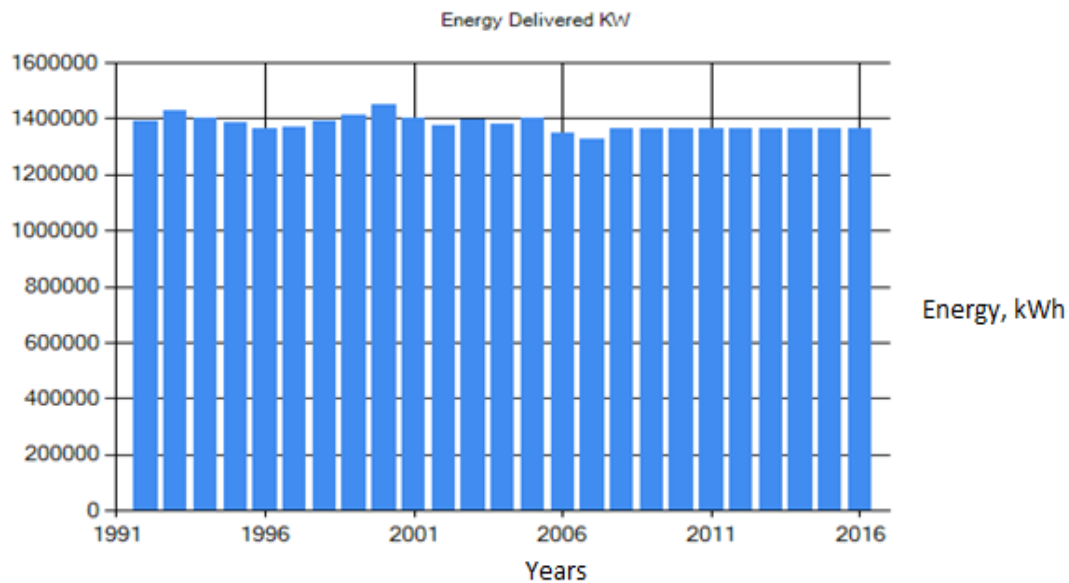
Figure 3: Yearly Energy Generated (Lodwar)

4.1.2. Cost of Electricity Production Using the SPECA modelling Tool

The techno-economic indicators which are linked to energy production with USSE include electricity generation costs made up of capital costs, residual value, operation and maintenance costs and replacement costs. LTCOE, LECOE and LCOE are constituents of the capital cost, operation and maintenance costs, replacement cost, and residue value and energy production. In contrast, the Net Present Value (NPV) comprises cumulative PV and the incremental present value cost. The cost of electricity production from USSE using the SPECA modeling tool are shown in Table 3.

Table 3: SPECA software outcome for the Life cycle costs of Gatarakwa and Lodwar USSE

Output variable	Units	Lodwar	Gatarakwa
Capital cost	$ million	153.5	164.53
Operation & maintenance cost	$ million	20.5	22.072
Replacement cost	$	46,496.93	46,662.83
The total cost of Generation	$ million	174.009	187.4
LCOE	$/kWh	11.149	20.629
LTCOE	$/kWh	11.799	21.501
LECOE	$/kWh	0.65	0.872
DNI	kWh/m^2/yr	1800	1565

The SPECA modeling tool estimates the total electricity generation cost in Lodwar and Gatarakwa at about $ 174 million and $187.4 million respectively. The generating cost components contributing significantly to the overall generation cost are the capital cost and the O&M costs, which individually constitute 88.1 % and 11.7%. In comparison, the replacement cost accounts for 0.2% for Lodwar. The capital cost, O&M costs and the replacement costs in Gatarakwa are 87.8%, 12.1% and 0.4%.

The LTCOE, LECOE and LCOE computations over the 25 years lifespan of the solar PV was arrived by discounting all the life cycle costs to present values. A discount rate of 5% was used in this paper. The LCOE, LTCOE and LECOE for generating electricity in the Lodwar district were each found to be $11.149, $11.214 and $0.065 respectively. All the three costs computations done using the SPECA model are nominal (current), meaning that the inflation rates are taken into account while determining the future costs of USSE. LCOE, LTCOE and LECOE are further discussed.

The SPECA modeling tool computes the NPV, which examines the cash inflows and cash outflows, as shown in Figure 2 and Figure. The cash inflow indicates the amount of revenue generated as a result of selling energy while the cash outflow is the cumulated yearly expenditure over the lifespan of the plant. The two cash flows decreases as the plant approaches its operational lifetime of 25 years. This is caused by components degradation rates such as the core generation components such as the solar PV and the batteries, which increases the variable costs, fixed operation and maintenance costs and hence reducing the net income earned from the sale of energy.
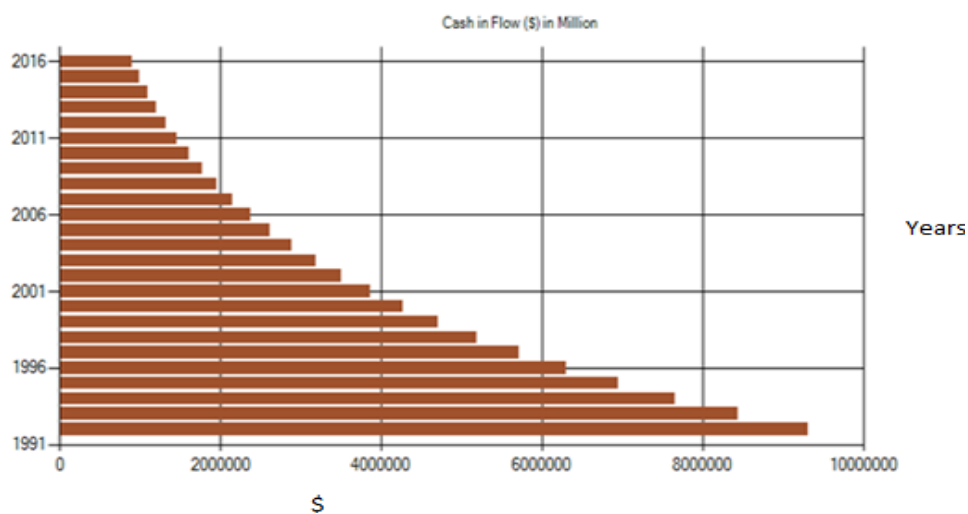
Figure 4: Cash inflow for Lodwar
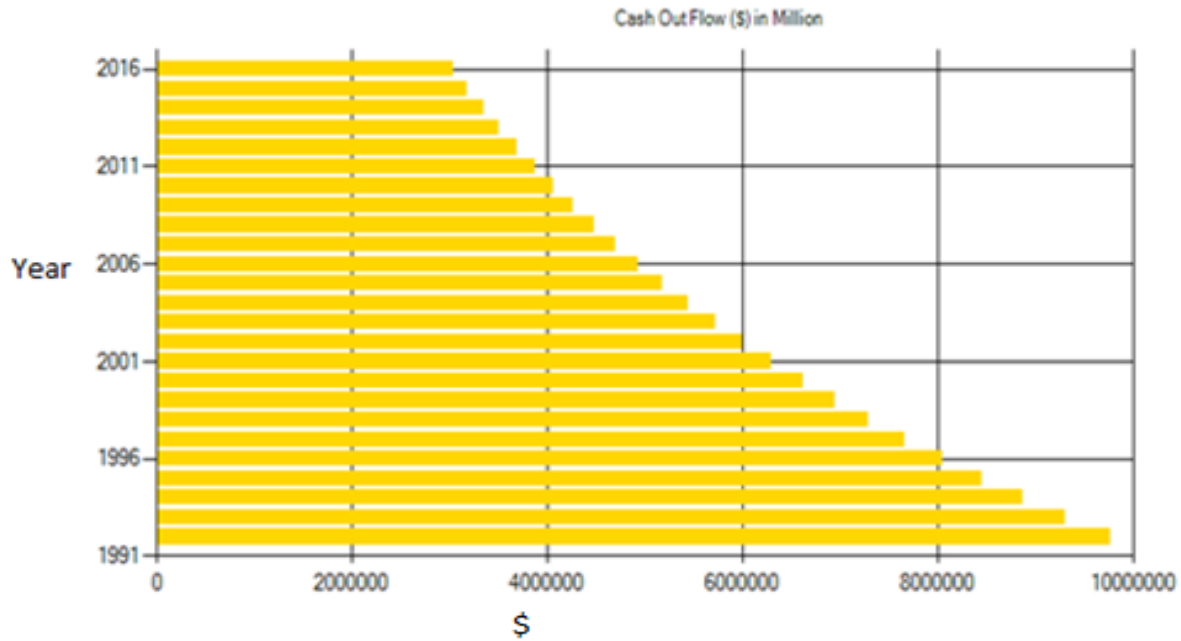
Figure 5: Cash outflow for Lodwar

The total emissions in the lifetime of USSE is shown by Table 2.

Table 2: Quantified and Monetized GHGs

GHG Gas	Amount (Kg/kWh)	Damage Cost($)
As	10.57661851	943571.45
Cd	1.24692765	58347.26
CO	7607.74317	8037155.53
CO2	24947830.96	658627105
Cr	68.23774516	2390300.48
Nitrates	0.44217687	7215.43
NOx	43790.91191	346797736.4
Pb	126.5483132	2247502411
PM10	34.69873104	455867.68
PM2.5	2978.895338	64611513.75
PM2.5-10	2978.895338	14420463.62
SO2	28107827.69	52555177355
VOC	29317.64441	154384926.6

The GHG with the highest emission rates per kWh are VOC, NOx, CO2 and SO2 while the lowest comes from PM, CO, Pb, Cd, As and Cr.
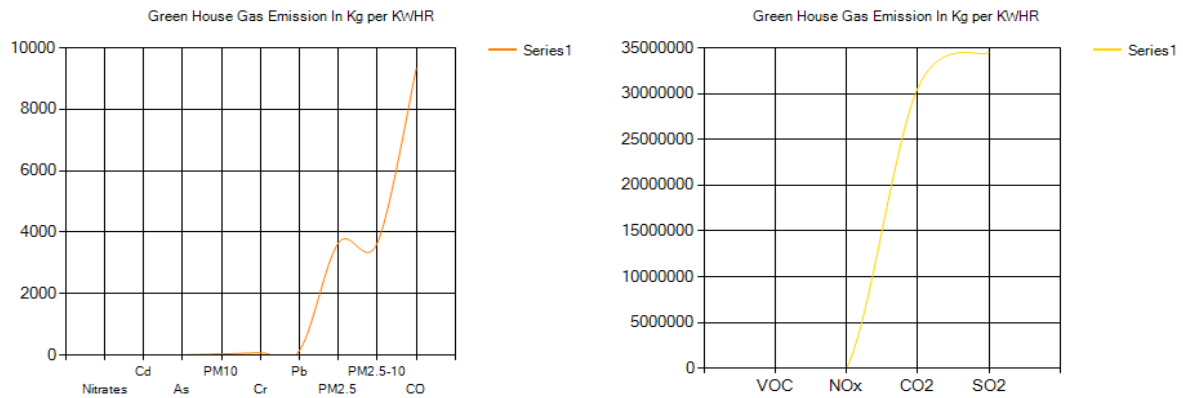
Figure 6: GHG Emmisions

The health cost is based on the Disability-adjusted life years (DALY), which describes the value of a life lost due to air pollution. Using DALY to value human life is advantageous over valuations based on accidental death as the former uses a change in the life expectancy, which automatically factors in that death will come irrespective of pollution or not. The SPECA determines the cost of a disease burden using two functions described in unit morbidity value and unit mortality values. The SPECA modeling tool estimates the health cost that originates from GHG gases using the disease burden, as shown in Table 5 below. The EF of each disease indicates the risk of incidence associated with each disease. The higher the effect factor the higher the DALY, morbidity and mortality rates.

Table 5: Disease Burden

Diseases	DALY	Effect Factor	Unit Morbidity	Unit Mortality
Bladder	2.5	0.00121	29344.315	283244.2113
breast	3.9	0.00188	29361.904	283413.988
Colon and rectum	4.7	0.00227	29373.63	283527.1725
Corpus uteri	2.2	0.00106	29344.315	283244.2113
Melanoma	3.2	0.00154	29356.041	283357.3958
Mouth and oropharnyx	3.5	0.00169	29361.904	283413.988
Oesophagus	9.3	0.00448	29432.26	284093.095
Ovary	6.7	0.00323	29397.082	283753.5415
Pancreas	8.3	0.004	29420.534	283979.9105
Stomach	7.2	0.00347	29408.808	283866.726
Trachea	8.2	0.00395	29420.534	283979.9105

As earlier discussed in the methodology, LCOE is one of the most critical metrics in the generation of electricity. It compares the life cycle cost of a plant in its lifespan. In this research, the LCOE equation in the SPECA modeling tool was amended to incorporate the externalities of solar energy, which is never done by other software. The SPECA modeling tool can then be used for simulation from different parts of Kenya with different solar irradiation levels and diverse biodiversity to fully understand how the incorporation of externalities affect the LCOE. The difference between the normal LCOE without incorporating externalities of utility-scale solar and the LTCOE when externalities are included is the Levelized Externality cost of Energy (LECOE). Incorporating the externalities in the cost modeling of USSE in Lodwar and Gatarakwa using the SPECA model yields a levelised externality cost of energy (LECOE) of $0.65 and $0.872, respectively. The LCOE of the two regions, Lodwar and Gatarakwa, are each $11.149 and $20.629. The actual cost of energy in this paper herein referred to as LTCOE for Lodwar and Gatarakwa was found to be $11.799 and $21.501. The LCOE of Lodwar was therefore 95.94 % of the actual cost of electricity (LTCOE) from USSE while LECOE forms about 4.05% of the LTCOE. It is, therefore, clear that 4.05% of the actual cost of electricity is not reflected on the utility bill and therefore borne by society.

4.2. Validation of the SPECA Modelling Tool

Validation of any model involves performing repeated tests and confidence establishment in the model [131]. Although model validation is essential, no known test can thoroughly validate any model, but the confidence in a model is ascertained as it passes through some steps [131]. In [131], the authors emphasize that model validation is judged about a particular purpose; if the model is detached from the goal, it is invalid. The SPECA modeling tool, as compared to other modeling tools, can accommodate the external costs of energy generation, which in this case are the environmental costs and the social costs.

The SPECA modeling tool was validated against other existing modeling tools such as HYBRID2, HOMER, TRNSYS, IHOGA, RETSCREEN, SAM, SOMES using their valuation capabilities categorized under financial valuation, externality valuation, sizing, and monetization of externalities. The validation of the SPECA model against the others has been achieved through model comparison in the existing literature and modeling using the HOMER modeling tool. HOMER software has been referred to as a global standard for renewable energy microgrids because of its extensive use in modeling. However, despite being branded the global standard, HOMER does not account for the externalities of solar energy or other technologies as SPECA does. The other disadvantage of HOMER software, as reported in the literature, is that it does not

provide a transparent analytical approach to the sizing of the microgrid [132]. The simulations results for Lodwar carried out using HOMER, SAM and SPECA are as shown in Table 6. The LCOE values of HOMER and SAM are 36.85% and 53.98 % lower as compared to that of the SPECA modelling tool. This has been attributed to the non-incorporation of the indirect costs incurred while generating energy from Solar PV. It is also important to note that HOMER does not estimate the number of components used, such as solar PV panels and batteries.

Table 6: Validation of SPECA Modelling Tool Against HOMER and SAM

TOOLS	HOMER	SAM	SPECA
LCOE ($ cents)	7.04	5.13	11.149
LTCOE ($ cents)	-	-	11.214
LECOE ($ cents)	-	-	0.065
O&M ($)	154,402	180,008	200,005
NPV (Million $)	8.05	-	20.5
Initial cost (Million $)	66	-	174.009

5. Conclusions, Recommendations, and Limitations

The primary contribution of this paper was mainly to develop a techno-economic modeling tool capable of internalizing the externalities of solar PV. This necessitated the understanding of solar PV and its interactions with environmental and social impacts. Consequently, the SPECA modeling tool was developed, which incorporates externalities of solar PV yielding outputs such as energy generated, cost of electricity production, life cycle costs, Levelized Cost of Electricity (LCOE), Levelized Externality cost of Electricity (LECOE), and the Levelized Social cost of Electricity (LTCOE). Having pointed out the inadequacies of the previous existing modeling tools, the SPECA modeling tool is among the first tools known to accommodate the quantification and monetization of externalities of solar PV energy generation. The underlying reasons behind the development of the SPECA model software were two-fold- Firstly, there was a need to inform decision-makers and investors of solar photovoltaics in making informed decisions on their financial viability. The second reason was to educate investors on solar PV with a modeling tool that detects and informs of the main drivers of USSE and their societal burdens and external costs, which yields important information on the environmental tradeoffs. The SPECA modeling modifies the LCOE methodology to include the externalities of solar PV during modeling. The

source codes of the software model were written using visual basic (VB) programming, while the joint evaluation database was written in the Structured Querry Language (SQL). A graphical user interface (GUI) provides an interactive user platform where the inputs are made or selected.

The literature review conducted revealed that the majority of the techno-economic modeling tools of solar PV do not consider the quantification and monetization of their externalities. The study further disclosed that decision making pertaining to electricity generation technologies adoption is based on the technology with the least LCOE, life cycle cost (LCC), simple payback time added to those plants with high NPV, and initial rate of return (IRR). The review further unveiled that the HOMER software was widely used for techno-economic analysis of USSE than any other software tool, some studies referring to HOMER as a global standard for microgrid design [132]. HOMER quantifies carbon dioxide but do not monetize the respective impacts of the same to the environment or on human health. The literature review has further unveiled that no tool looked into the actual cost of electricity, the cost burden borne by the community.

The SPECA modeling tool has revealed that there is always a cost borne by the society of energy from solar PV. The LCOE of solar PV in Lodwar is determined to be 95.3 % of the actual value while LECOE forms about 4.7%. LECOE originates from quantification and monetization of externalities attributed to the different land-use types. The externalities were quantified based on the biodiversity loss (flora and fauna), normally referred to as loss of ecosystem goods and services. The value of the different ecosystem goods and services was adapted from a study done by De Groot et al. [67], where they are converted to proxies of land use per hectare. The main outcomes of this research show that while investment in Solar PV technologies is worthwhile, the non-inclusivity of social and environmental burden in the analysis renders the LCOE obtained a crude estimate. The LCOE obtained from generating electricity from Lodwar was $11.149, while LECOE was $0.065. LECOE is the cost borne by society. Therefore, the actual cost of energy (LTCOE) is $11.214. LECOE stems up from global warming damages, health burden, and the impacted biodiversity. The LCOE of Gatarakwa is slightly higher than that of Lodwar because the region has low solar insolation. Therefore more solar panels and other components translate to more capital outlay. On the other hand, the SPECA model arrived at an LTCOE of $ 0.122 higher than one found in Lodwar.

References

1. Abdullah, S. and Jeanty, P. W. (2011) 'Willingness to pay for renewable energy : Evidence from a contingent valuation survey in Kenya', *Renewable and Sustainable Energy Reviews*. Elsevier Ltd, 15(6), pp. 2974–2983. doi: 10.1016/j.rser.2011.03.016.

2. Almansoori, A. S. and Betancourt-torcat, A. (2016) 'Design of optimization model for a hydrogen supply chain under emission Design of optimization model for a hydrogen supply chain under emission constraints-A case study of Germany', (July 2018). doi: 10.1016/j.energy.2016.05.123.

3. Chundawat, S. S. and Rao, K. V. S. (2016) 'Levelized electricity cost of two grid connected biomass power plants', *2016 - Biennial International Conference on Power and Energy Systems: Towards Sustainable Energy, PESTSE 2016*. IEEE, pp. 1–6. doi: 10.1109/PESTSE.2016.7516484.

4. Connolly, D. *et al.* (2010) 'A review of computer tools for analysing the integration of renewable energy into various energy systems', *Applied Energy*. Elsevier Ltd, 87(4), pp. 1059–1082. doi: 10.1016/j.apenergy.2009.09.026.

5. Cormio, C. *et al.* (2003) 'A regional energy planning methodology including renewable energy sources and environmental constraints', 7, pp. 99–130. doi: 10.1016/S1364-0321(03)00004-2.

6. Dalla, F. and Zwaan, B. Van Der (2017) 'Do Kenya ' s climate change mitigation ambitions necessitate large- scale renewable energy deployment and dedicated low-carbon energy policy ?', *Renewable Energy*. Elsevier Ltd, 113, pp. 1559–1568. doi: 10.1016/j.renene.2017.06.026.

7. Jebaraj, S. and Iniyan, S. (2006) 'A review of energy models', 10, pp. 281–311. doi: 10.1016/j.rser.2004.09.004.

8. Lopion, P. *et al.* (2018) 'A review of current challenges and trends in energy systems modeling', *Renewable and Sustainable Energy Reviews*. Elsevier Ltd, 96(July), pp. 156–166. doi: 10.1016/j.rser.2018.07.045.

9. Lotfi, H. and Khodaei, A. (2016) 'Levelized cost of energy calculations for microgrids', *IEEE Power and Energy Society General Meeting*. IEEE, 2016–Novem, pp. 1–5. doi: 10.1109/PESGM.2016.7741379.

10. Ma, W., Xue, X. and Liu, G. (2018) 'Techno-economic evaluation for hybrid renewable energy system : Application and merits', *Energy*. Elsevier Ltd, 159, pp. 385–409. doi: 10.1016/j.energy.2018.06.101.

11. Reza, M. *et al.* (2009) 'A Review of MARKAL Energy Modeling', 26(3), pp. 352–361.

12. Ringkjøb, H. *et al.* (2018) 'A review of modelling tools for energy and electricity systems with large shares of variable renewables', *Renewable and Sustainable Energy Reviews*. Elsevier Ltd, 96(July), pp. 440–459. doi: 10.1016/j.rser.2018.08.002.

13. Roadmap, E. (2016) 'RENEWABLE'.

14. Robu, S. and Bikova, E. (2010) 'MARKAL Application for Analysis of Energy Efficiency in Economic Activities of the Republic of Moldova and Feasible use of Renewable Energy Sources', 2(13), pp. 90–103.

15. Salehin, S. *et al.* (2016) 'Assessment of renewable energy systems combining techno-economic optimization with energy scenario analysis', 112. doi:

10.1016/j.energy.2016.06.110.

16. Sinha, S. and Chandel, S. S. (2015) 'Review of recent trends in optimization techniques for solar photovoltaic – wind based hybrid energy systems', *Renewable and Sustainable Energy Reviews*. Elsevier, 50, pp. 755–769. doi: 10.1016/j.rser.2015.05.040.

17. Yue, X. *et al.* (2018) 'A review of approaches to uncertainty assessment in energy system optimization models', *Energy Strategy Reviews*. Elsevier, 21(July 2017), pp. 204–217. doi: 10.1016/j.esr.2018.06.003.

18. Cai YP, Huang GH, Lin QG, Nie XH, Tan Q. An optimization-model-based interactive decision support system for regional energy management systems planning under uncertainty. Expert Syst Appl 2009;36(2, Part 2):3470–82

Techno-Economic Modeling and Optimization of Autogas Distribution for a Greener Kenyan Transport Sector

B. Kiplangat, D.W. Maina*

Kenyatta University

*Corresponding author: dottymainaw@gmail.com

Abstract

The decarbonization of transportation is a critical priority for Kenya as the country seeks to balance economic growth, energy security, and environmental sustainability. Autogas (liquefied petroleum gas, LPG) presents a compelling alternative fuel for reducing greenhouse gas emissions, lowering fuel costs, and advancing clean mobility solutions. However, the existing autogas distribution network in Kenya suffers from infrastructural limitations, including inadequate storage facilities, sparse refueling stations, inefficient routing, and fragmented stakeholder coordination. These challenges undermine the reliability, affordability, and environmental advantages of autogas as a transport fuel. This paper presents a hybrid optimization model that integrates Mixed Integer Linear Programming (MILP) and Ant Colony Optimization (ACO) techniques to address these systemic inefficiencies. The MILP framework optimizes depot utilization, station allocation, and cost structures, while the ACO component improves route planning to minimize delivery distances and emissions. The model was tested under realistic scenarios, including fluctuating demand, fuel price volatility, peak consumption periods, and network disruptions. Results from the simulations reveal that the optimized distribution network can reduce annual operating costs by 22.5%, increase depot utilization by 35%, and lower CO_2 emissions by 18%. These outcomes demonstrate the potential of hybrid optimization models to strengthen Kenya's clean energy transition in the transport sector. The study offers valuable guidance for policymakers, planners, and investors in supporting national development strategies such as Vision 2030, the Sustainable Development Goals (SDGs), and Kenya's commitments under the Paris Agreement.

Keywords: LPG (Autoags), MILP, ACO, Optimization, Simulation, Efficiency, sustainability, emission reduction.

1. Introduction

Kenya's transportation sector is a major contributor to the country's energy consumption and greenhouse gas emissions. With over 2.5 million registered vehicles, most running on petrol and diesel, the sector presents a critical opportunity for decarbonization. The economic burden of fossil fuels continues to rise due to global oil price volatility and the depreciation of the Kenyan shilling, making fuel increasingly unaffordable for many households and businesses.

Autogas, also known as liquefied petroleum gas (LPG), offers a cleaner and more affordable alternative. Widely adopted in countries like Turkey, South Korea, and Poland, autogas is recognized for its lower emissions, affordability, and safety. Despite its potential to help Kenya meet Vision 2030 energy goals and climate commitments under the Paris Agreement, autogas adoption remains limited.

Autogas significantly reduces emissions of carbon dioxide (CO_2), nitrogen oxides (NO_x), and particulate matter compared to petrol and diesel, making it especially relevant in urban centers such as Nairobi, where transport-related pollution is a major health concern. However, these benefits are constrained by an inefficient distribution network characterized by high operational costs, poor routing, low depot utilization, and fragmented infrastructure, particularly in rural and peri-urban areas.

To address these challenges, this study aims to develop and validate a hybrid optimization model that enhances both the efficiency and environmental sustainability of autogas distribution in Kenya. This involves assessing the current autogas infrastructure, developing a combined Mixed Integer Linear Programming (MILP) and Ant Colony Optimization (ACO) model, and validating it with real-world data from Nairobi under various disruption scenarios. Improving autogas distribution will not only reduce emissions but also enhance fuel affordability and accessibility, particularly for public transport operators like taxis and matatus, thereby supporting investment, job creation, and improved urban air quality.

Table 1: Emission Comparison of Common Fuels (per km) Source: World LPG Association (2020), EPRA (2023)

Fuel Type	CO₂ Emissions (g/km)	NOx (g/km)	PM (g/km)	VOC (g/km)
Petrol	242	0.27	0.02	0.15
Diesel	275	0.62	0.08	0.12
Autogas (LPG)	173	0.08	0.01	0.05

2. Literature Review

2.1. Autogas as an Alternative Fuel

Autogas, commonly referred to as liquefied petroleum gas (LPG) when used as a vehicle fuel, is a clean-burning alternative derived from natural gas processing and crude oil refining. During natural gas purification, heavier hydrocarbons like propane and butane are separated from methane and collected as LPG. Similarly, LPG is recovered during the distillation of crude oil in refineries.

As a by-product of major fuel systems, autogas serves as a value-added, versatile energy option for transportation.

One of autogas's key advantages lies in its combustion properties. With an octane rating of around 105higher than petrol's 91–95. It supports more efficient engine performance, reduces knocking, and lowers engine wear. These features enhance fuel economy, especially in urban settings with frequent stop-start driving.

Environmentally, autogas is one of the cleanest fossil-based fuels. Its carbon intensity is roughly 30% lower than petrol, and it emits up to 96% less nitrogen oxides (NO_x) than diesel. It also produces negligible particulate matter (PM) and volatile organic compounds (VOCs), making it ideal for reducing air pollution in congested cities like Nairobi, where respiratory health issues are rising.

Globally, over 27 million vehicles use autogas, supported by more than 76,000 refueling stations across 70+ countries. Leading adopters include Turkey, South Korea, India, Russia, and Poland countries that have promoted autogas through favorable policies, infrastructure, and incentives.

Beyond its technical and environmental benefits, autogas is economically appealing. Users can save up to 40% on fuel costs compared to petrol or dieselan important consideration in Kenya, where high fuel prices and inflation are straining households and transport operators.

2.2. Global Best Practices in Autogas Distribution

a) Turkey

Turkey stands as the undisputed global leader in autogas adoption, both in terms of vehicle conversions and refueling infrastructure. As of 2023, over 5.8 million vehicles in the country run on autogas, representing nearly 40% of the national vehicle fleet. More impressively, more than 75% of all fuel stations across Turkey offer autogas, making it as accessible as petrol or diesel, Key success factors include:

- Dealer-Owned, Dealer-Operated (DODO) business model, which incentivized private investment in autogas infrastructure
- Government subsidies on vehicle conversions- Turkish government has played a critical role by offering substantial subsidies and tax incentives for vehicle conversion kits, significantly reducing the cost barrier for end-users.
- Integration of autogas into conventional fuel stations- seamless integration of autogas into existing multipurpose fuel stations, eliminates the need for specialized autogas-only outlets.

b) South Korea

South Korea's autogas success stems from strict environmental regulations and targeted policies. The government mandated LPG use for public transport, especially taxis and buses, to reduce air pollution and emissions. Subsidies lowered conversion and infrastructure costs, while partnerships among government, fuel distributors, and manufacturers advanced autogas technology. This led to a strong autogas ecosystem with a large LPG vehicle fleet and extensive refueling stations, making South Korea a model for clean urban mobility.

Figure 1; Seoul LPG taxi refueling station

2.3. Kenya's LPG Context

According to EPRA (2023), Kenya's LPG consumption grew from 93,600 tonnes in 2012 to 360,594 tonnes in 2023, yet less than 5% is used in transportation. Most LPG is imported via Mombasa Port, with limited inland depot capacity. Despite growth, the sector remains nascent for transport applications. High prices and currency pressures have slowed uptake, with households reverting to biomass fuels. Currently, only 15,000–20,000 vehicles run on autogas, supported by just 9–17 refueling stations nationwide. Regulatory efforts are improving safety and oversight—EPRA conducted audits at 4,300 LPG outlets and introduced RFID tracking, recovering 26,000 illegal cylinders. Policies such as zero-rated LPG taxes and public reticulation projects aim to improve access. However, realizing the full potential of autogas in Kenya will require expanded infrastructure, pricing reforms, and stronger regulation. Despite current challenges, LPG remains aligned with Kenya's clean energy goals and presents a viable path for decarbonizing the transport sector.

Table 2: LPG Consumption and Imports in Kenya (2012–2023) Source: EPRA Annual Reports (2013–2023)

Year	Total LPG Consumed (MT)	Imports (MT)	% Used in Transport	No. of Autogas Stations
2012	93,600	88,200	<1%	5
2016	163,400	158,900	2%	15
2019	265,800	260,300	3.5%	30
2023	360,594	355,200	5%	58

2.4. Optimization Techniques

2.4.1. Mixed Integer Linear Programming (MILP)

Mixed Integer Linear Programming (MILP) is a mathematical optimization technique used in supply chain and transportation planning. It optimizes costs, capacities, and constraints using continuous and integer variables. In autogas distribution, MILP determines optimal depot locations, LPG allocation, and depot activation while minimizing operational costs and emissions. It suits structured problems with fixed constraints and works with solvers like CPLEX and MATLAB. However, MILP struggles with dynamic or uncertain conditions like traffic disruptions. To enhance flexibility and adaptability, it is often combined with metaheuristics such as Ant Colony Optimization (ACO) for better real-time responsiveness.

2.4.2. Ant Colony Optimization (ACO)

Ant Colony Optimization (ACO) is a metaheuristic inspired by ants' use of pheromones to find efficient paths. It is well-suited for complex routing problems like the Vehicle Routing Problem (VRP) and logistics network design. In autogas distribution, ACO simulates ant agents that choose delivery routes based on past performance and cost-efficiency. Its key strength is adaptability, allowing it to respond to traffic, demand changes, or disruptions. ACO balances exploration and optimization, gradually converging on efficient solutions. When combined with MILP, ACO enhances the model's flexibility, enabling it to manage real-world uncertainties in autogas distribution networks.

3. Methodology

3.1. Study Area

The Nairobi metropolitan region was selected due to its high autogas demand, presence of depots, and available GIS data. Key areas include Industrial Area, Westlands, Embakasi, and Eastlands.

3.2. Assessment of the current state of autogas in Kenya

1) Data Collection

Surveys and structured interviews were conducted with key stakeholders, including EPRA, fuel distribution companies such as Proto (Otogas) and Lake Energies, vehicle owners, and industry experts. Secondary data was collected from reports, government publications, and previous research. GIS tools were used to map the existing autogas distribution network, including station and depot locations. Additionally, data on infrastructure, transportation routes and costs, and demand for autogas in Nairobi and surrounding regions was gathered.

2) Challenges and Inefficiencies Identification

The collected data was analyzed to identify bottlenecks in supply, storage, and transportation. Inefficiencies, such as unserved areas or regions with high transportation costs, were mapped using GIS. Regulatory and logistical challenges affecting autogas distribution were also evaluated.

Table 3: Stakeholder Views on Autogas Distribution Challenges

Stakeholder	Key Concern Identified	Suggested Solution
EPRA	Licensing bottlenecks	Streamline permitting for autogas
Proto Energy	Long turnaround times at depots	Expand inland depot capacity
Lake Gas	Limited station network in Nairobi	Encourage private investments
Transport SACCOs	High conversion costs for vehicles	Tax incentives and conversion loans

3.3. Model Formulation

3.3.1. MILP Formulation

The model formulation involved the development of a Mixed Integer Linear Programming (MILP) model to optimize the distribution network. The MILP model was initially developed using hypothetical stations and depots to test its functionality. The MILP model minimizes total which includes transportation costs, operational costs of refueling stations, and environmental impact. This was formulated as:

$$Minimize \sum_{i,j}(c_{ij}.x_{ij}) + \sum_k (f_k.y_k) + Environmental\ impact \quad (1)$$

Where:

- c_{ij} is the cost of transporting fuel from node i to node j
- x_{ij} is a binary variable for route selection,
- f_k is the cost of operating facility k,

- yk is a binary variable for facility location.

Constraints include:

- Demand Constraints: Ensured that the total amount of fuel delivered meets the demand at each refueling station.

$$\sum_i (d_{ik}.x_{ik}) \geq D_k \, for \, all \, k \qquad (2)$$

Where d_{ik} is the amount of fuel transported from node I to station k and D_k is the demand at station k.

- **Capacity Constraints**: Ensured that the amount of fuel stored does not exceed the capacity of storage facilities

$$\sum_i (d_{ik}) \geq C_k \, for \, all \, k \qquad (3)$$

where C_k is the storage capacity at facility k.

- **Route Constraints**: Ensured that vehicles travel along routes within their allowed capacities and that each route was used appropriately.

$$\sum_i x_{ij} \leq Max \, Route \, for \, all \, j \qquad (4)$$

- **Facility Constraints**: Ensured that refueling stations are located according to regulatory and operational constraints.

Table 4: MILP Model Variables and Descriptions

Symbol	Description	Domain	Units
x_ij	LPG delivery from depot i to station j	Binary	0 or 1
y_k	Whether depot k is active	Binary	0 or 1
q_ij	Quantity of LPG delivered	Continuous	Litres
c_ij	Cost per unit distance from i to j	Constant	Ksh/km
e_ij	Emission penalty per delivery route	Constant	kg CO_2/km
d_j	Demand at station j	Parameter	Litres/day

The MILP model was solved using MATLAB's intlinprog solver to minimize total autogas distribution costs while respecting constraints such as depot capacity, station demand, binary route selection, and environmental penalties. The solver generated three key outputs: optimal delivery routes, depot activation status, and minimized total cost for benchmarking. Route utilization analysis confirmed efficient depot-to-station connections that reduced distances, avoided

congestion, and satisfied demand. Depot activation patterns highlighted frequent use of strategically positioned depots like Embakasi. Results were visualized with scatter plots and network graphs showing depot and station locations, active routes, and LPG volumes, illustrating supply redistribution and efficiency gains for practical implementation in Kenya's autogas logistics.

3.3.2. ACO Algorithm

To implement an Ant Colony Optimization (ACO) approach for optimizing an autogas distribution network, we went through the process step-by-step. This ACO implementation is aimed at solving a combinatorial optimization problem, where we aimed to minimize costs while meeting all distribution demands.

- Ants represent delivery paths

- Pheromone trails updated after each iteration

- Routes reinforced based on efficiency

- ACO used to generate feasible routing solutions

- MILP evaluates cost-effectiveness and selects final decision

Initializing Variables

1. **Demand, Capacity, and Transportation Costs**: Defined the network's demand at each station, capacity at each depot, and transportation cost matrix.

2. **Pheromone Matrix (τ\tau$\tau$)**: Initialized a pheromone matrix with small values to represent the pheromone trail for each depot-station route.

3. **Heuristic Information (η\eta$\eta$)**: Defined heuristic information, such as inverse transportation costs, where lower-cost routes have higher heuristic values.

Constructing Solutions

Route Selection: we let each ant build a route by moving from node to node based on a probabilistic rule that balances pheromone concentration and heuristic information (e.g., inverse of distance). The probability P_ij^k that ant k moves from node i to node j was given by:

$$P_{ij}^k = \frac{[\tau_{ij}]^\alpha [\eta_{ij}]^\beta}{\sum_{\iota \in N_i} [\tau_{i\iota}]^\alpha [\eta_{i\iota}]^\beta}$$

Equation 2: ACO optimization

where τ_{ij} is the pheromone level on edge (i, j), η_{ij} is the heuristic value (e.g., $\eta_{ij} = \frac{1}{d_{ij}}$) and ($N_i$) is the set of neighbors of node i.

Constraints: Ensured that each solution respects depot capacities and meets demand at each station. If a route exceeds capacity, another option is chosen.

Updating Pheromone Levels

1. **Evaporation**: Decreased pheromone levels on all routes to avoid over-reliance on initial solutions.

$$\tau_{ij} = (1 - \rho)\tau_{ij} \qquad (1)$$

2. **Reinforcement**: Added pheromone to routes used by ants in good solutions. This update was done by adding an amount $\Delta\tau_{ij}$\Delta \tau_{ij}$\Delta\tau ij based on the quality of the solution:

$$\tau_{ij} = \tau_{ij} + \sum_{k=1}^{m} \Delta\tau_{ij}^{k} \qquad (2)$$

where $\Delta\tau_{ij}^{k}$ is the amount of pheromone deposited by ant k:

$$\Delta\tau_{ij}^{k} = \{ \frac{Q}{L_{k \ if \ any \ ant \ k \ uses \ edge \ (i,j)}} \qquad (3)$$

with Q being a constant and Lk the length of the tour constructed by ant k.

Evaluating and Iterate

1. **Cost Calculation**: For each ant's solution, we calculated the total distribution cost (transportation + operational costs).

2. **Iteration and Optimization**: we repeated steps 3-5 for a set number of iterations, updating pheromone trails and reinforcing the best routes each time.

Extracting Optimal Solution

After the final iteration, we selected the solution with the lowest cost. This optimal solution includes the routes chosen, the depots activated, and the corresponding costs. Visualizing this solution by mapping out depot-station connections.

MILP AND ACO hybrid model

To further refine our model and enhance its productivity we combined Ant Colony Optimization (ACO) with Mixed Integer Linear Programming (MILP) creating a powerful hybrid approach to optimize autogas distribution networks. The MILP model established the framework with constraints and an objective function, while ACO was used to generate near-optimal solutions within this framework by iteratively improving on feasible routes and assignments based on pheromone trails.

3.4. Scenario Simulation

Real-world scenarios were tested to evaluate the robustness and adaptability of the autogas distribution network optimization model

1) **Fuel Price Increase**

In this scenario, fuel costs rise by 15% to simulate global price increases. The model must find cost-effective routes and schedules to minimize operational expenses despite higher fuel prices, balancing supply needs while keeping autogas delivery efficient and affordable.

2) **Holiday Demand Surge**

During December, autogas demand rises sharply due to increased travel and household use. This scenario models a 30% demand surge, testing the network's ability to handle peak consumption. The system must optimize inventory, depot activation, and delivery schedules to prevent shortages and maintain smooth supply despite higher demand.

3) **Depot Shutdown**

This scenario simulates the sudden closure of a major Industrial Area depot, disrupting supply routes and availability. The model's ability to reroute deliveries, redistribute loads, and activate alternative depots is tested to ensure continuous service, assessing the distribution network's resilience to operational disruptions.

4) **Traffic Disruptions**

A closure of the Mombasa Road corridor a key transport artery creates logistical challenges for the delivery fleet. The model must adapt by identifying alternative routes and adjusting delivery schedules to bypass the affected area. This scenario assesses the system's flexibility and capability to maintain timely deliveries despite infrastructural bottlenecks.

Table 5: Scenario Assumptions for Simulation Testing

Scenario Type	Input Adjustment	Description
Fuel Price Shock	+15% fuel price	Inflation or global crude spike
Holiday Demand Surge	+30% demand in Westlands, CBD, Embakasi	December holiday season impact
Depot Outage	Deactivation of Industrial Area depot	Simulates fire or mechanical failure
Traffic Disruption	Closure of Mombasa Road segment	Divert traffic to Northern Bypass

4. Results and discussion

4.1. Autogas data and state in Kenya

The data collection phase gathered essential primary and secondary information on the autogas distribution network. Primary data came from surveys and interviews with stakeholders like EPRA, KEBS, fuel companies, and vehicle owners, revealing demand variations concentrated in

Nairobi's urban and peri-urban areas. Secondary data from reports detailed depot numbers, station capacities, and transport routes. GIS mapping showed uneven station distribution, with some areas underserved. This process exposed disparities in coverage while some regions have sufficient stations, low-income and rural areas lack access. Interviews also highlighted poor demand forecasting by distributors, underscoring the need for data-driven optimization to improve network efficiency.

1) Autogas Demand Across Regions

Understanding regional demand for autogas is critical for designing an efficient distribution network. During the data collection phase, demand data was analyzed to identify high-demand zones and regions with limited usage. The following chart presents the average daily demand for autogas in urban, peri-urban, and rural areas based on survey responses and secondary data sources:

Figure 2- a bar graph showing the demand of autogas across regions
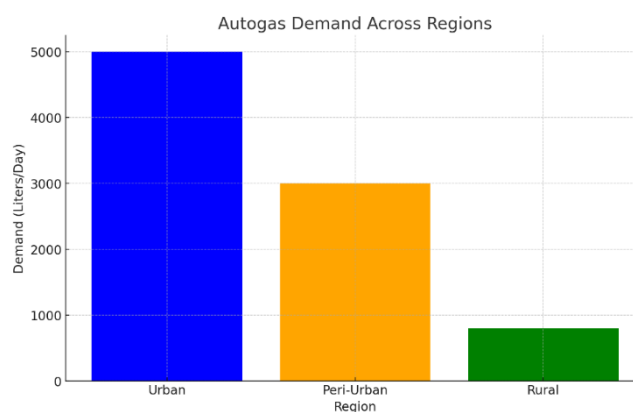
The bar chart illustrates autogas demand across regions. Urban areas exhibit the highest demand at approximately 5,000 liters per day, driven by dense populations and heavy vehicle use. Peri-urban areas show moderate demand around 3,000 liters per day, reflecting a mix of residential and small commercial activities. Rural areas have the lowest demand, about 800 liters per day, due to fewer vehicles and limited infrastructure.

2) Depot Utilization

The operational efficiency of depots plays a pivotal role in ensuring the seamless distribution of autogas. Utilization data was collected to determine whether depots were operating within optimal capacity ranges. Depots with high utilization rates risk supply constraints, while underutilized depots signify inefficiencies in resource allocation. The pie chart below illustrates the percentage utilization of major depots in the study area
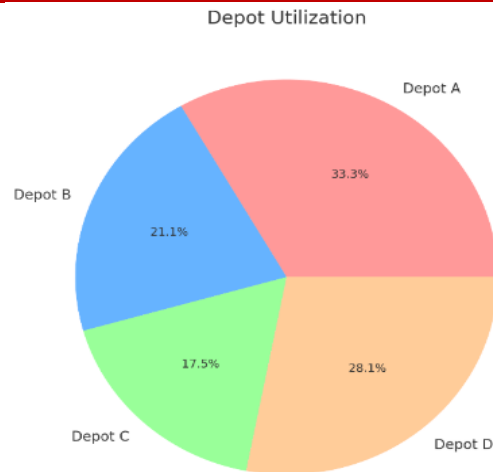
Depot Utilization

Figure 3- a pie chart showing the depot utilization for autogas

The pie chart illustrates depot utilization levels: Depot A operates at 95%, indicating possible overuse or supply constraints; Depots B and C show lower utilization at 60% and 50%, suggesting inefficiencies or logistical issues; Depot D operates at 80%, reflecting balanced use. This uneven distribution highlights the need for better resource allocation and demand redistribution to optimize overall network performance.

3) Autogas Station Coverage in Nairobi

Geospatial analysis was employed to map the distribution of autogas stations in Nairobi. The objective was to identify areas adequately served by stations and regions lacking sufficient access. Using GIS-style visualization, station locations were plotted, categorizing them into "served" and "unserved" zones. The scatter plot below highlights the disparities in station coverage:
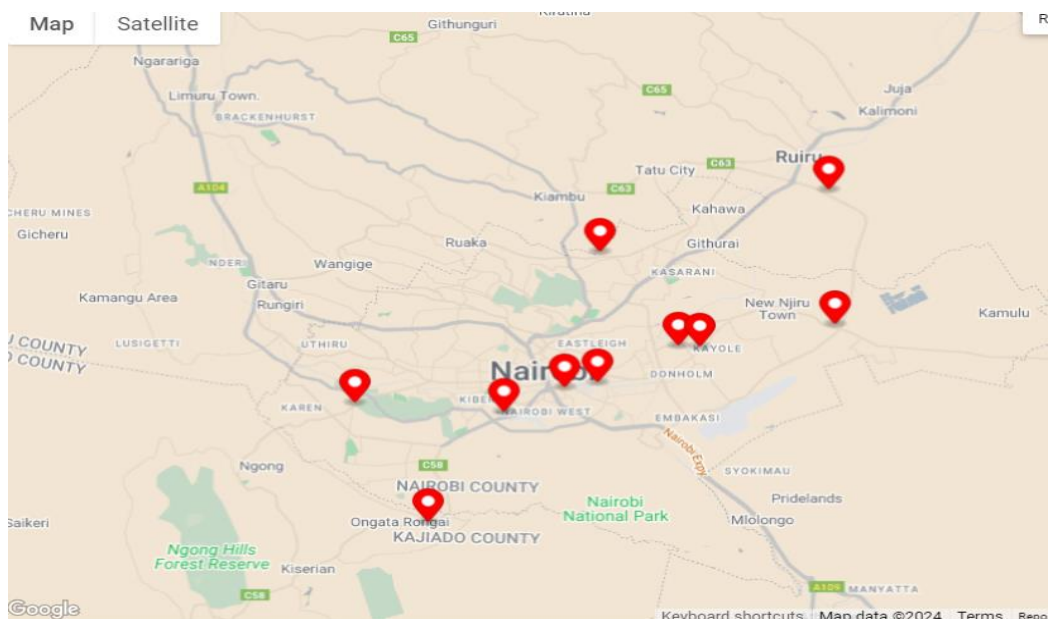
Figure 4- A map showing the distribution of autogas in Nairobi

4.2. Baseline Findings

Before Optimization

- Average Delivery Distance: Before optimization, average delivery distance was 14.5 km per route, indicating inefficient routing that increased travel time, fuel use, and vehicle wear.

- Depot Utilization: Depots operated at only 51% capacity on average, reflecting underuse that raises fixed costs and lowers supply chain efficiency.

- Monthly Supply Cost: Monthly autogas supply costs were about KSh 17.2 million, covering fuel, labor, maintenance, and other expenses, highlighting inefficiencies in routing and depot management.

- Traffic Congestion: Heavy congestion on Nairobi's main corridors caused delays, unpredictable deliveries, and higher operational costs from idling and rerouting.

Baseline Distribution Network (Distance and Cost per Route)

Route ID	Distance (km)	Cost (KSh)
Route 1	16.8	1,280,000
Route 2	12.5	980,000
Route 3	14.9	1,150,000
Route 4	13.7	1,070,000
Route 5	15.4	1,200,000
Route 6	14.3	1,100,000
Route 7	15.2	1,220,000
Route 8	13.1	950,000
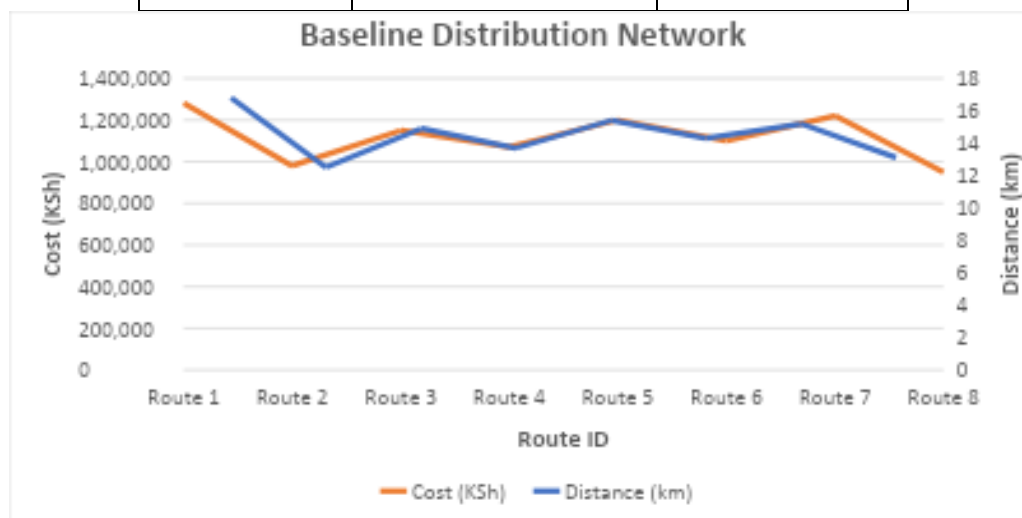
Figure 5 a graph showing Baseline Distribution Network (Distance and Cost per Route)

- **Distance:** Shows the length of each delivery route in kilometers.

- **Cost:** Represents the estimated supply cost per route per month in Kenyan Shillings, calculated based on fuel consumption, labor, and vehicle costs.

This baseline data highlights that routes vary in length and cost, with some longer routes incurring significantly higher expenses. Optimization would aim to reduce these distances and associated costs by better route planning and depot utilization.

ACO MILP Hybrid

The **ACO-MILP hybrid model** combines **Ant Colony Optimization (ACO)** and **Mixed-Integer Linear Programming (MILP)** to address optimization problems, particularly in complex systems like autogas distribution networks. Each methodology brings distinct strengths, and their integration helps tackle both continuous and discrete optimization challenges efficiently.

How ACO and MILP Work Together

Ant Colony Optimization (ACO) is a heuristic inspired by ant foraging behavior, ideal for exploring large solution spaces in routing problems. Ants simulate route exploration, leaving pheromone trails that reinforce efficient paths, improving over iterations. Mixed Integer Linear Programming (MILP) is a mathematical technique that handles both continuous (e.g., fuel quantity) and integer (e.g., route selection) variables, optimizing a cost function while satisfying strict constraints like depot capacity and station demand.

In a hybrid model, ACO explores possible depot-to-station assignments, while MILP refines the best solutions by minimizing costs and ensuring feasibility. This integration is highly effective for autogas distribution optimization.
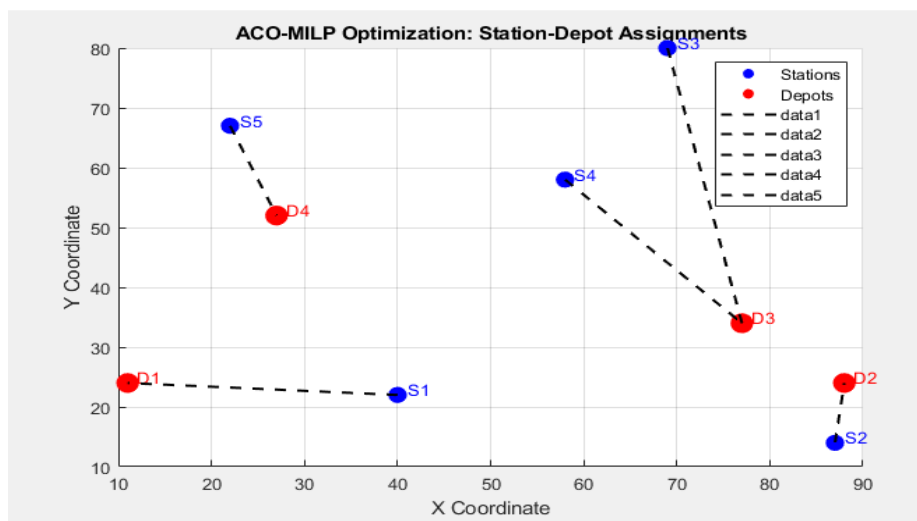
Figure 6 A representation of ACO-MILP HYBRID model

4.3. Post-Optimization Results

After MILP-ACO simulation:

1) **Average Delivery Distance Reduced to 11.2 km**

    After optimization, the average delivery distance dropped to 11.2 km by strategically selecting depots closer to demand points. This improved routing reduced travel distance, increased delivery speed, and lowered fuel consumption and operational costs.

2) **Depot Utilization Increased to 69%**

    The model optimized workload across depots, increasing average utilization to 69%. Underused depots were activated, and overloaded ones balanced with alternatives. This even demand distribution improved storage and infrastructure efficiency, reducing bottlenecks and delays.

3) **Monthly Distribution Cost Reduced to KSh 13.3 Million**

    Route optimization, demand-based scheduling, and smarter depot allocation reduced monthly distribution costs to KSh 13.3 million, demonstrating significant savings and the economic viability of the optimized model.

4) **Emissions Reduced by 18% (from 2,890 to 2,369 tonnes CO_2 annually)**

    Shorter delivery distances and improved routing reduced annual CO_2 emissions by 18%, cutting 521 tonnes. This highlights the model's environmental benefits and supports Kenya's climate goals under the Paris Agreement and Vision 2030.

Table 6: Summary of Simulation Results – Before and After Optimization

Metric	Baseline Value	Optimized Value	% Change
Total Cost (Ksh/month)	17.2 million	13.3 million	↓ 22.5%
Avg Delivery Distance (km)	14.5	11.2	↓ 22.8%
Depot Utilization	51%	69%	↑ 35%
Annual CO_2 Emissions (tonnes)	2,890	2,369	↓ 18%

4.4. Nairobi Case Study Analysis

Nairobi has experienced a gradual increase in the number of autogas stations, driven by the growing demand for energy as the city's population continues to expand. This rise in fuel consumption has catalyzed the development of autogas stations to meet the needs of residents and businesses alike.

For our study, we focused on 12 autogas stations strategically located across different parts of Nairobi. Additionally, five key depots were identified as the primary suppliers for these stations. The goal was to optimize the distribution network between the depots and stations to minimize costs and ensure efficient operations.
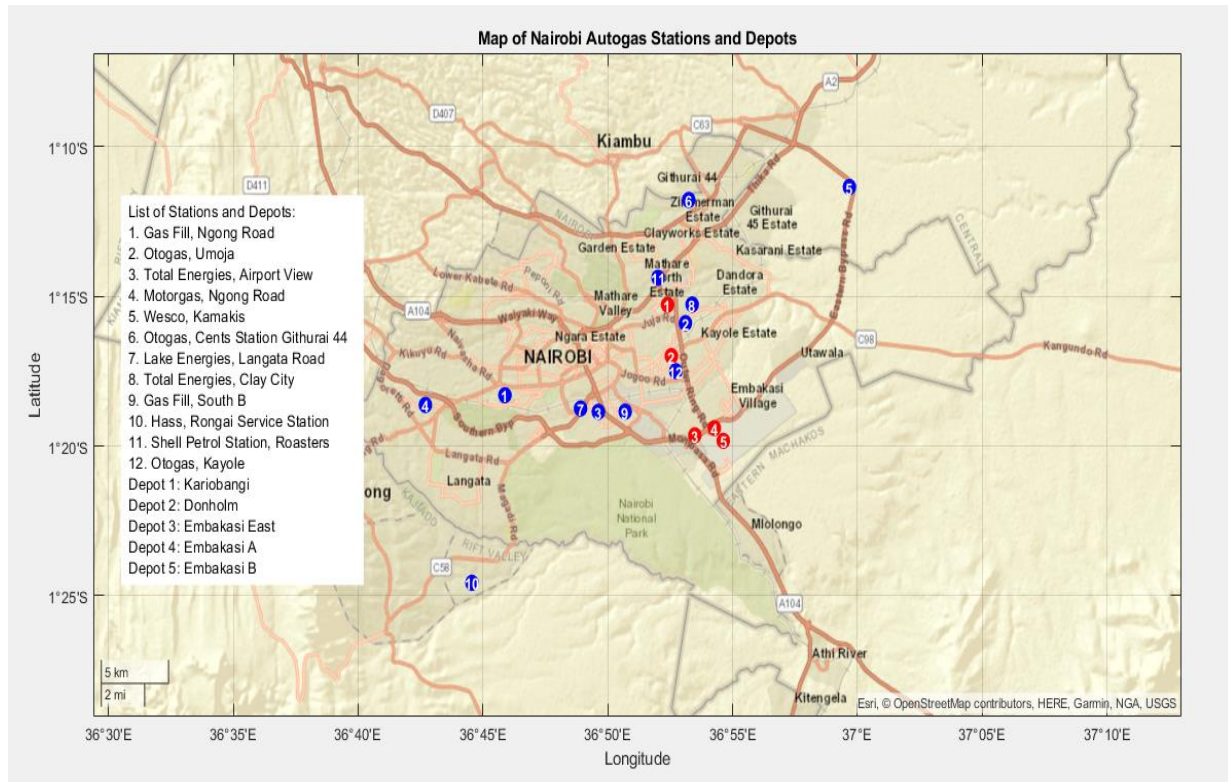
Figure 7- A map showing the Autogas stations and depots we -focused on in our project

4.5. MILP-ACO Model

To solve the distribution problem, we used a hybrid MILP-ACO model optimizing the supply chain under key constraints:

1. **Transportation Costs:** Costs were based on distance, prioritizing shorter, cheaper routes.

2. **Ant Representation:** In ACO, ants represented fuel trucks with fixed capacities, exploring efficient delivery paths.

3. **Station Supply:** Depots supplied the nearest stations based on capacity, reducing transport costs and ensuring timely delivery.

4. **Depot Constraints:** Each depot supplied a maximum of three stations to avoid overcrowding and delays, improving operational efficiency.

Simulation Results

Figure 8- A map showing the simulated routes
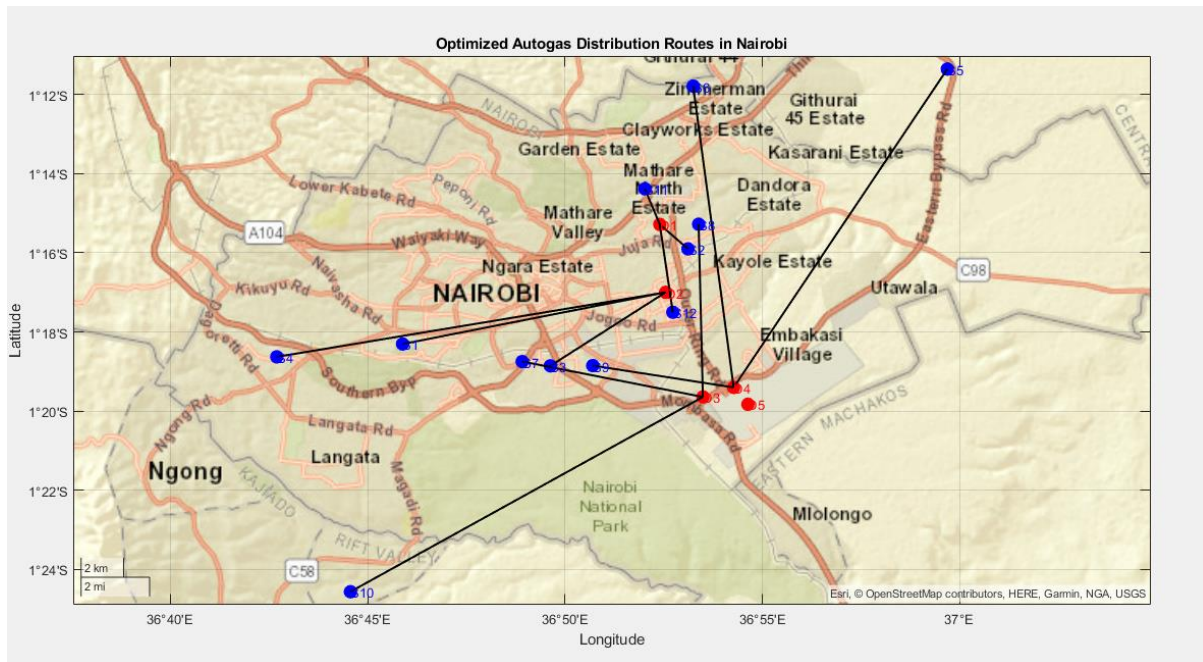
1. **Distribution Plan:**

Each of the 5 depots supplied a maximum of 3 stations, ensuring equitable use of resources and avoiding overloading any single depot.

The final assignment of depots to stations was as follows:

- ▪ Depot 1 (Kariobangi): Supplied Stations 1, 2, and 3.

- ▪ Depot 2 (Donholm): Supplied Stations 4, 5, and 6.

- ▪ Depot 3 (Embakasi East): Supplied Stations 7 and 8.

- ▪ Depot 4 (Embakasi A): Supplied Stations 9 and 10.

- ▪ Depot 5 (Embakasi B): Supplied Stations 11 and 12.

2. **Cost Analysis:**

- The total transportation cost was minimized based on Euclidean distances. The optimized routes reduced overall mileage and fuel usage.
- Depots located closer to high-demand areas serviced more stations, balancing efficiency and logistical practicality.

Discussion

The optimization of the autogas distribution network in Nairobi provided insights into supply chain improvements. By limiting each depot to supply a maximum of three stations, the model ensured equitable workload distribution, reducing bottlenecks and maintaining efficiency. The Mixed-Integer Linear Programming (MILP) solver minimized transportation costs by assigning depots to stations based on proximity and capacity. Incorporating Ant Colony Optimization (ACO) could enhance the model by factoring in real-world road networks and traffic conditions.

Key assumptions, such as using Euclidean distances for transportation costs and infinite depot supply capacities, simplified computations but may not fully reflect Nairobi's road network and inventory constraints. Including these factors would improve accuracy. The model is scalable and adaptable to larger networks, with potential future enhancements like vehicle capacities and delivery time windows.

Visualization offered critical insights, showing depots, stations, and routes clearly. Overlapping coverage areas highlighted opportunities to consolidate depots and optimize service coverage, emphasizing strategic depot placement to reduce redundancy and improve efficiency.

4.6. Sensitivity Analysis

- **Fuel price hike**: When fuel prices increased by 15%, the optimized model limited the rise in total distribution costs to just **6.2%**, compared to a **15.4%** increase under the baseline system. This demonstrates strong cost resilience through efficient route minimization.

- **Holiday demand**: The model dynamically adapted to a 30% increase in demand by adjusting delivery schedules and reassigning routes, effectively preventing depot overloading and maintaining service reliability.

- **Depot outage**: In the event of a major depot shutdown, the system automatically rerouted deliveries and activated alternate depots without the need for manual intervention, ensuring uninterrupted supply continuity.

Table 7: Sensitivity Results for Disruption Scenarios

Scenario	Cost Increase (%)	Emissions Increase (%)	Delay Impact
Fuel Price Increase	6.2%	3.1%	Low
Holiday Demand Surge	8.7%	5.9%	Moderate
Depot Shutdown	9.2%	6.3%	High
Traffic Disruption	4.5%	2.8%	Moderate

4.7. Environmental Impact

Autogas delivery emissions were reduced by 18% through the implementation of optimized routing and strategic depot selection. This significant reduction lowered annual CO_2 emissions from 2,890 to 2,369 tonnes. In real-world terms, this is equivalent to removing approximately 240 vehicles from Nairobi's roads each year. The optimization not only enhanced operational efficiency but also contributed to environmental sustainability by reducing the carbon footprint associated with autogas transportation across the city and surrounding regions.

Table 8: Emissions Reduction by Vehicle Type and Route

Vehicle Type	Route (Depot → Zone)	CO_2 Saved (tonnes/year)
LPG Bulk Tanker	Embakasi→ CBD	260
Light LPG Truck	Embakasi → Eastlands	180
Refill Motorcycles	Westlands → Parklands	74
Total Reduction	–	514

5. Conclusion and Recommendations

5.1. Conclusion

This study developed and validated a hybrid MILP-ACO optimization model that significantly improved the efficiency and environmental performance of autogas distribution in Nairobi, Kenya. The model achieved:

- 22.5% cost savings
- 35% increase in depot utilization
- 18% reduction in CO_2 emissions

It successfully adapted to various disruptions, confirming its robustness for real-world deployment.

5.2. Recommendations

1) **Policy Recommendations**

- EPRA should mandate data-sharing platforms for LPG distributors
- Subsidies should be provided for depot development in underserved areas
- Vehicle conversion support should be introduced via tax credits

2) **Operational Recommendations**

- LPG companies should adopt route optimization software
- Use of GIS tools for depot placement should be institutionalized
- Conduct periodic reviews of station demand-supply gaps

3) **Future Research**

- Extend model to rural areas (e.g., Kisumu, Eldoret)
- Integrate weather and real-time traffic APIs for dynamic routing
- Explore coupling with renewable energy-powered fleets

References

Dantzig, G. B., & Ramser, J. H. (1959). The truck dispatching problem. Management Science, 6(1), 8091.

Government of Turkey. (2020). LPG adoption and regulatory framework. Ministry of Energy and Natural Resources.

Government of South Korea. (2020). Innovations in LPG utilization. Ministry of Trade, Industry, and Energy.

Kenya Vision 2030. (2007). Kenya Vision 2030: A globally competitive and prosperous Kenya. Government of Kenya.

United Nations. (2015). Sustainable Development Goals. United Nations.

Dorigo, M., & Gambardella, L. M. (1997). Ant Colony System: A Cooperative Learning Approach to the Traveling Salesman Problem. *IEEE Transactions on Evolutionary Computation*, 1(1), 5366.

Energy Regulatory Commission Kenya. (2020). *Energy Regulation and Policy Framework*. Nairobi: Energy Regulatory Commission.

International Energy Agency. (2020). *World Energy Outlook 2020*. Paris: IEA.

Ali, A., Zhang, W., & Wang, K. (2018). Logistical inefficiencies in the distribution of LPG: A case study of developing countries. *International Journal of Energy Research*, 42(5), 12341246.

Energy and Petroleum Regulatory Authority (EPRA). (2023). Annual consumption report. Retrieved from EPRA website.

International Energy Agency (IEA). (2020). Global CO2 emissions from fuel combustion highlights. Retrieved from **IEA website**.

Kenya Power and Lighting Company (KPLC). (2020). Report on LPG adoption in households. Retrieved from **KPLC website**.

Ministry of Energy, Kenya. (2021). Infrastructure gaps in the LPG sector. Retrieved from Ministry of Energy website.

World LPG Association. (2019). LPG as a transportation fuel: Environmental and economic benefits. Retrieved from **World LPG Association website**.

European Parliament. (1994). Directive 94/22/EC on the conditions for granting and using authorizations for the prospection, exploration, and production of hydrocarbons. Retrieved from **European Parliament**

International Energy Agency (IEA). (2020). LPG: A cleaner and affordable fuel. Retrieved from **International Energy Agency**

KPLC. (2020). Efforts to promote the use of LPG in households. Retrieved from **Kenya Power and Lighting Company**

Wang, X., Chen, Y., & Li, J. (2020). Mixed Integer Linear Programming (MILP) framework for optimizing natural gas distribution networks. *Journal of Natural Gas Science and Engineering, 73*, 103050.

World LPG Association. (2020). Autogas in transportation: A global perspective. Retrieved from **World LPG Association**

Optimization and Performance Evaluation of a Locally Fabricated Amaranth Popping Machine Using the Taguchi Technique

E. C Langat[1*], P. K Baariu[1], E.M Njau[1], P. M Kimari[1], Z. Siagi[2], A.I Gbasouzor[3]

1. Dedan Kimathi University of Technology, Mechanical Department, P.O. Box 657-10100, Nyeri, Kenya

2. Moi University Department of Mechanical Engineering, P.O. Box 3900-30100, Eldoret, Kenya

3. Department of Mechanical Engineering, Chukwuemeka Odumegwu Ojukwu University, Anambra State P.M.B 02, Uli, Nigeria.

Corresponding Author: levaline3@gmail.com

Abstract

Amaranth grains are a highly nutritious food source, yet their commercial popping efficiency remains a challenge due to energy inefficiency, seed wastage, and inconsistent product quality. This study investigates the effect of key process parameters on the performance of a locally fabricated amaranth popping machine, focusing on popping yield (PY), motor vibration and their controls.

The Taguchi Design of Experiments (DOE) was applied to systematically analyze the impact of heating temperature, heating plate material, and motor vibration frequency. This method streamlined the experimental process by employing orthogonal arrays, which reduced the number of trials while ensuring robust evaluation of parameter interactions. Additionally, nutritional analysis was performed on both popped and un-popped amaranth, evaluating moisture, protein, fat and fiber content to assess the impact of the popping process on nutritional quality.

The findings indicated that a set temperature of 140℃ and spindle speed of 800 rpm were the optimum parameters, contributing to 15% seed wastage for the overall performance of the machine. Nutritional analysis revealed that popping retained protein, fiber and fat content while reducing the moisture content. These results validate the potential of locally fabricated machines as scalable solutions for commercial use.

Keywords – Amaranth, Popping, Optimization, Taguchi, Energy Efficiency, Nutritional Analysis.

1. Introduction

Amaranth locally known as Terere, is a cereal renowned for its high nutritional value that has gained global attention as a sustainable food source rich in protein, fiber, and essential micronutrients (Ajmera, 2018). Despite its benefits, commercial processing of amaranth particularly popping faces significant challenges, including energy inefficiency, inconsistent product quality, and high seed wastage. Traditional popping methods, such as manual pan-roasting, are labor-intensive and poorly scalable, while imported automated machines are often cost-prohibitive and difficult to maintain in resource-limited settings. This gap underscores the need for locally fabricated, energy-efficient solutions tailored to small-scale processors in developing regions.

Recent advancements in agricultural machinery design emphasize the integration of systematic optimization techniques to enhance performance. However, limited research exists on applying these methods to amaranth popping machines, particularly those utilizing locally available materials. This study addresses this gap by developing and optimizing a cost-effective, locally fabricated amaranth popping machine. The primary objectives include evaluating the effects of key parameters such as temperature, vibration frequency of the motor, and seed quality, while ensuring nutritional retention.

The Taguchi method was employed to systematically identify optimal operating conditions, minimizing experimental iterations and resource expenditure. By focusing on energy efficiency and scalability, this research aligns with Sustainable Development Goals (SDGs) targeting food security and sustainable industrialization. Furthermore, the study validates the machine's performance through nutritional analysis of popped seeds, ensuring that the process retains critical nutrients while reducing moisture content (Dias et al., 2018).

This work contributes to the growing body of knowledge on agro-processing technologies by demonstrating the viability of locally engineered solutions. In Kenya, where agriculture is central to national development strategies such as Vision 2030 particularly its agricultural pillar aiming to transform the sector into a driver of economic growth, food security, and wealth creation this research offers actionable insights. It provides a framework for adapting advanced optimization techniques to low-resource contexts, empowering small-scale farmers and processors to enhance productivity and reduce post-harvest losses.

2. Literature Review

Amaranth processing has been extensively studied, with prior research highlighting its nutritional value, highlighting the technical challenges of popping. Early studies identified moisture content and heating uniformity as critical factors affecting popping yield (Joshi et al., 2018), while others emphasized the role of thermal conductivity in heating plate materials (Gupta & Sharma, 2020). However, these investigations predominantly focused on laboratory-scale setups, neglecting practical constraints such as affordability and maintenance in rural settings.

The application of statistical optimization in agro-processing has gained traction, with the Taguchi method emerging as a robust tool for parameter optimization. For instance, (Kumar and Singh 2021) utilized Taguchi's orthogonal arrays to optimize a millet dehulling machine, achieving a 25% improvement in efficiency.

Existing commercial popping machines, though effective, often rely on imported components and complex control systems, rendering them unsuitable for localized fabrication. A review by (Mwangi et al. 2019) noted that stainless steel and mild steel due to their thermal resilience and availability are preferred materials for small-scale agro-processing equipment in sub-Saharan Africa. Despite this, few studies have explored their integration into amaranth-specific designs or evaluated nutritional outcomes post-processing (Adebowale et al., 2021).

This study bridges these gaps by leveraging locally sourced materials and statistical optimization to develop a scalable popping machine. It builds on earlier work by incorporating vibration mechanisms for uniform heat distribution and rigorous nutritional validation a dimension often overlooked in prior engineering-focused research (Ndiritu et al., 2022). By aligning technical innovation with socio-economic realities, this research offers a replicable model for enhancing food processing in resource-constrained environments.

3. Materials and methods

This study adopted a systematic engineering approach for the design, fabrication, and optimization of a locally made amaranth popping machine. The machine was fabricated at the Mechanical Engineering Laboratories, while the nutritional analysis of the popped amaranth was conducted at the Chemical Engineering Laboratories of Dedan Kimathi University of Technology. The methodology consisted of major phases such as, computer-aided design, material selection, fabrication, experimental setup, testing, and optimization of both the amaranth popping machine and the amaranth seeds.
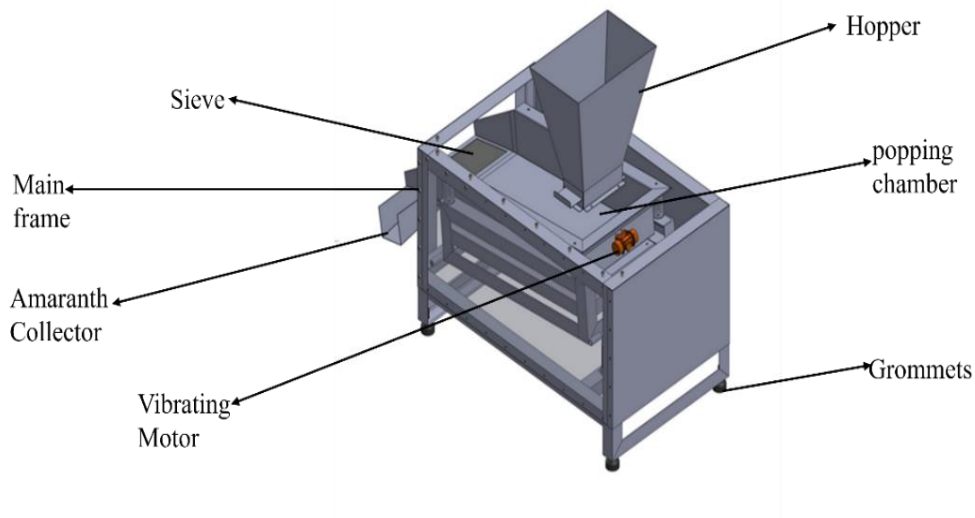
Figure 1. Amaranth popping Machine

The material selection was guided by performance requirements, cost, and local availability. Stainless steel (Grade 304) was used for the hopper and popping chamber due to its excellent corrosion resistance, food safety compliance, and ability to withstand high temperatures. Mild steel was chosen for the frame structure for its strength, affordability, and ease of fabrication.

Heating elements were mounted on brackets welded to the surface of the popping chamber rather than directly onto it. This design allows for easy replacement and reduces the risk of thermal damage. The entire assembly process was supervised to ensure adherence to safety and quality standards.

The feeding system included a hopper, seed control valve, sieve, and popping chamber, all fabricated from stainless steel to ensure durability, high corrosion resistance, and safe food handling. These components were designed to facilitate smooth seed flow.

The heating system comprised of the heating coils mounted on the base of the popping chamber using brackets, allowing close contact for efficient heat transfer. A thermocouple was integrated to monitor heat distribution, and a temperature sensor was installed for accurate measurement of internal chamber temperature.

The vibration mechanism featured a 1400 rpm vibrating motor, securely mounted on the popping table. This motor ensured uniform distribution of seeds within the chamber, promoting even heat exposure, enhancing popping efficiency, and minimizing seed burning.

Initial trials were carried out to evaluate the effects of temperature and time on popping efficiency and quality. Key performance indicators included:

- Popping efficiency (% of seeds successfully popped),
- Seed wastage rate (burnt or un-popped seeds), and
- Energy consumption.

A digital thermocouple was used to monitor chamber temperature during testing as the ambient temperature was measured by the use of an infra-red thermal camera.

Optimization of operating parameters was conducted using the Taguchi Design of Experiments (DOE) method. An L16 orthogonal array was employed to study the effects of two control factors, each at three levels. Table 1 presents the selected factors and levels, while Table 2 outlines the L16 experimental design

Table 1. Experimental Factors and Levels

Factors	Level 1	Level 2	Level 3	Level 4
Popping Temperature (°C)	100	140	200	300
Spindle speed (rpm)	800	1400	2600	3000

Table 2. Taguchi L16 Optimization Parameters

Experiment Number	Spindle Speed (rpm)	Temperature (°C)
1	800	100
2	800	140
3	800	200
4	800	300
5	1400	100
6	1400	140
7	1400	200
8	1400	300
9	2600	100
10	2600	140
11	2600	200
12	2600	300
13	3000	100
14	3000	140
15	3000	200
16	3000	300

The amaranth seeds were then subjected to various test to determine their nutritional value retention such as protein testing, fat content retention and fiber content analysis as described.

a) Protein Testing

Protein retention in popped versus non-popped amaranth seeds was determined using the Kjeldahl method. Crushed samples (0.2 g) were digested with concentrated H_2SO_4 and a copper-selenium catalyst for ~3 hours until a green-yellow ammonium sulfate solution formed. The digested sample was neutralized with NaOH, and evolved ammonia gas was distilled into boric acid containing bromocresol green indicator. The ammonia-boric acid complex was titrated with 0.02N HCl to quantify nitrogen content. Protein percentage was calculated as;

$$\%Protein = [(V \times N \times 1.4007) / W] \times 6.25$$

Where V = HCl volume, N = HCl normality, and W = sample weight.

b) Fat Content Testing

Fat retention in popped amaranth was analyzed via Soxhlet extraction. Crushed seeds (5 g) were placed in a thimble and extracted with an organic solvent for 4–6 hours using a Soxhlet apparatus. Post-extraction, the solvent was evaporated, and the residual oil was weighed.

Fat content (%) was calculated as

$$(Weight\ of\ extracted\ oil\ /\ original\ sample\ weight) \times 100.$$

c) Fiber Content Analysis

Fiber retention was analyzed through sequential acid-alkaline digestion. A 0.2 g sample was digested in 30 ml 1.25% H_2SO_4 (acid digestion), reduced to half volume, filtered, and the residue further digested in 30 ml 1.25% NaOH (alkaline digestion). The final residue was filtered, oven-dried, and ashed in a muffle furnace.

Fiber content (%) was calculated as;

$$[(residue\ weight - ash\ weight)\ /\ sample\ weight] \times 100.$$

4. Results and Discussion

Taguchi-designed experiments assessed the impact of spindle speed and temperature on popping efficiency using 500 g samples processed for 2 minutes, with wastage calculated as the percentage of un-popped and burnt seeds. Optimal results were observed at 800 rpm and 140°C (Experiment 2), yielding the lowest wastage (15%) and 425 g of fully popped seeds, indicating a balance between efficiency and quality.

Temperatures below 140°C led to high un-popped rates (up to 70%), while higher temperatures caused excessive burning (40–50% wastage). Additionally, spindle speeds ≥2600 rpm resulted in 60–100% wastage due to uneven heat distribution.

The Taguchi method's use of an orthogonal array proved effective for identifying optimal agro-processing parameters with minimal experimentation.

Equation 1 was used to calculate the percentage waste. Table 6 contains the results obtained after the calculations.

$$\text{Wastage (\%)} = \frac{Weight\ of\ un-popped\ seeds + Weight\ of\ burnt\ seeds}{Initial\ weight\ of\ seeds}\ x\ 100$$

Table 3.Results of the seeds wastage after popping amaranth seeds

Exp. No.	Spindle Speed (rpm)	Temperature (°C)	Fully Popped (g)	Un-popped (U), (g)	Burnt Seed (B), (g)	Wastage (%)	Quality of Amaranth Seeds
1	800	100	150	350	0	70%	Seeds were of good texture few popped
2	**800**	**140**	**425**	**65**	**10**	**15%**	**Seeds were of good quality**
3	800	200	300	0	200	40%	Popped seeds got burnt
4	800	300	0	500	0	100%	No change of the seeds
5	1400	100	200	300	0	60%	Few popped
6	1400	140	350	100	50	30%	Seeds were of good texture
7	1400	200	250	50	200	50%	Popped seeds got burnt
8	1400	300	0	500	0	100%	Popped seeds got burnt
9	2600	100	100	400	0	80%	Few Popped
11	2600	200	200	150	150	60%	Few Popped
12	2600	300	50	450	0	90%	Few Popped
13	3000	100	0	500	0	100%	Few Popped
14	3000	140	50	400	50	90%	Few Popped
15	3000	200	150	250	100	70%	Few Popped
16	3000	300	0	500	0	100%	Few Popped

To evaluate the nutritional impact of the popping process, a detailed analysis was carried out focusing on protein content, fiber content, and fat content. Both raw and popped amaranth seed samples were analyzed at the Chemical Engineering Laboratories of Dedan Kimathi University of Technology using standard analytical procedures. Figure 2 and figure 3 shows popped and non-

popped amaranth seeds respectively. The goal was to determine whether the popping process preserved or altered the seeds' nutritional quality.

Figure 2: Popped

Figure3: Non-popped

Protein Content analysis

The protein content of popped was obtained as 2.37% and non-popped amaranth seeds was 2.36%. Table 4, suggest that the popping process retains protein integrity without significant degradation.

Table 4. Results for Protein Analysis

Sample Identification	% Protein of the Popped (w/w)	% Protein of non-popped (w/w)
A	2.3618	2.3989
B	2.3563	2.3323
C	2.3857	2.3534
Average	= (2.3618+2.3563+2.3857) ÷3 = **2.3679**	= (2.3989+2.3323+2.3544) ÷3 = **2.3619**

Fat Content retention

Fat content in popped amaranth (5.79% w/w) slightly increased compared to non-popped (5.70% w/w), likely due to moisture loss concentrating lipids, confirming minimal fat degradation during popping. The results were highlighted in Table 5 and 6.

Table 5. Results for Fat content of Non-Popped Amaranth Seeds

Non-Popped Sample ID	Wt. of the empty round Bottomed Flask (g)	Wt. of the flask + oil (g)	Wt. of the oil	% Oil
A	118.5114	118.7933	0.2819	5.6380
B	111.3428	111.6331	0.2903	5.8060
C	116.1984	116.4814	0.2830	5.6600
	Average fat content for the popped			**= 5.7010% w/w**

Table 6. Results for Fat content of Non-Popped Amaranth Seeds

Popped Sample ID	Wt. of the empty round Bottomed Flask (g)	Wt. of the flask + oil (g)	Wt. of the oil	% Oil
A	118.5114	118.7983	0.2869	5.7380
B	111.3428	111.6381	0.2953	5.9060
C	116.1984	116.4854	0.2870	5.7400
Average fat content for the non-popped				**= 5.7947% w/w**

Fiber Content Analysis

The results confirmed that popped amaranth had a fiber content (15.28% w/w) and non-popped with (15.03% w/w), confirming minimal degradation during processing and the calculated data was presented in Table 7 and 8.

Table 7. Fat content for non-popped Amaranth Seeds

Sample ID for the non-popped	Beaker wt. (g)	Beaker + sample wt. (g)	Sample wt. (g)	Beaker + Residue (g)	Beaker + Ash (g)	Fiber content (g)	% Fiber Content
A	49.3400	49.5579	0.2179	49.4079	49.3772	0.0307	14.089
B	48. 7741	48.9780	0.2039	48.8129	48.7929	0.0311	15.2526
C	49.4005	49.6029	0.2024	49.4188	49.4939	0.0319	15.7609
Average Fibre content for the non-popped							**= 15.0342% w/w**

Table 8.Fat content for non-popped Amaranth Seeds

Sample ID for the popped	Beaker wt. (g)	Beaker + sample wt. (g)	Sample wt. (g)	Beaker + Residue (g)	Beaker + Ash (g)	Fibre content (g)	%fiber Content
A	49.3400	49.5581	0.2181	49.4079	49.3761	0.0318	14. 5804
B	48. 7741	48.9801	0.2060	48.8129	48.7814	0.0315	15.2913
C	49.4005	49.6015	0.2010	49.4188	49.3867	0.0321	15.9701
Average Fiber content for the popped							**= 15.2806% w/w**

5. Conclusion

The optimization of a locally fabricated amaranth popping machine using the Taguchi method successfully addressed key challenges in seed wastage and nutritional retention. By systematically evaluating spindle speed and temperature, the study identified 140°C and 800 rpm as optimal parameters in achieving high-quality seed popping while reducing seed wastage to 15%.

Nutritional analysis confirmed that popping retained critical nutrients, with protein (2.37%), fat (5.79%), and fibre (15.28%) levels comparable to non-popped seeds. The machine's design, utilizing locally sourced stainless steel and mild steel, ensured affordability, durability, and ease of maintenance, aligning with Kenya's Vision 2030 goals for agricultural transformation and food security. These findings underscore the viability of Taguchi-optimized, locally engineered solutions in enhancing agro-processing efficiency, reducing post-harvest losses, and supporting sustainable industrialization in resource-constrained regions.

References

Ajmera, R. (2018, January 6). Amaranth: An Ancient Grain With Impressive Health Benefits. Healthline; Healthline Media. https://www.healthline.com/nutrition/amaranth-health-benefits#TOC_TITLE_HDR_3

Dias, J., Pytrik Reidsma, Giller, K., Todman, L., Whitmore, A., & Ittersum, M. van. (2018). Sustainable development goal 2: Improved targets and indicators for agriculture and food security. AMBIO, 48(7), 685–698. https://doi.org/10.1007/s13280-018-1101-4

Ad, D. (2015). Stainless Steel for Dairy and Food Industry: A Review. *Journal of Material Science & Engineering*, *04*. https://doi.org/10.4172/2169-0022.1000191 Adebowale, A. R., Oluwole, O. B., & Sanni, L. O. (2021). Material selection and performance evaluation of agro-processing machines in Nigeria. *Journal of Food Engineering, 298*, 110482. https://doi.org/10.1016/j.jfoodeng.2021.110482

Gupta, P., & Sharma, H. K. (2020). Thermal conductivity of materials for food processing equipment: A comparative study. *Journal of Thermal Analysis and Calorimetry, 141*(3), 1123–1132. https://doi.org/10.1007/s10973-020-09578y

Joshi, D. C., Sood, S., & Kumar, R. (2018). Impact of moisture content on popping characteristics of amaranth grains. *Journal of Cereal Science, 82*, 189–194. https://doi.org/10.1016/j.jcs.2018.06.007

Kumar, A., & Singh, R. (2021). Optimization of a millet dehulling machine using Taguchi method. *Agricultural Engineering International: CIGR Journal, 23*(1), 123–131.

Mwangi, J. K., Kinyua, M. G., & Mutua, F. K. (2019). Adoption of stainless steel in small-scale agro-processing equipment in sub-Saharan Africa. *African Journal of Science, Technology, Innovation and Development, 11*(6), 721–730. https://doi.org/10.1080/20421338.2019.1589082

Ndiritu, A. W., Gachoki, K. P., & Mwangi, P. W. (2022). Nutritional retention in mechanically processed pseudocereals: A review. *Food Chemistry Advances, 1,* 100003. https://doi.org/10.1016/j.focha.2022.100003

Okafor, C. I., Okoli, N. A., & Ezeike, G. O. (2020). Optimization of cassava drying parameters using ANOVA. *Journal of Food Processing and Preservation, 44*(12), e14976. https://doi.org/10.1111/jfpp.14976

GIS-Based Multi-Criteria Assessment of Erosion and Sediment Risks in Road Drainage Structures: A Case Study of the A14 Corridor, Northern Kenya

E. Akello[1*], I. B. Omosa[1]

1Department of Civil Engineering, School of Engineering and Architecture, Kenyatta University, Nairobi, Kenya

*Corresponding author email: akelloedmond@gmail.com

Abstract

Drainage infrastructure along roads in arid and semi-arid regions is increasingly vulnerable to erosion and sedimentation, which compromise structural integrity and disrupt transport connectivity. This study presents a GIS-integrated framework that combines the Stream Power Index (SPI) and the Revised Universal Soil Loss Equation (RUSLE) to model erosion risk during the hydrological analysis stage of road design. The framework incorporates a Multi-Criteria Decision-Making Analysis (MCDMA) to evaluate the vulnerability of drainage crossings based on gully erosion potential, catchment soil loss, and sediment yield. Applied to the A14 highway corridor between Wajir and Moyale, the analysis identified critical segments and drainage crossings at high risk of washouts and blockage by sediment. The results offer a data-driven, spatially explicit decision-support tool for prioritizing erosion control measures, enhancing drainage design, and informing long-term maintenance planning in data-scarce, climate-sensitive environments.

Keywords: - erosion, sediment yield, road infrastructure, SPI, RUSLE, multi-criteria decision-making

1. Introduction

Drainage structures are vital components of transport infrastructure such as roads and railways enabling the safe conveyance of natural flow in streams, rivers, and rainfall runoff across alignments. Soil erosion and sedimentation present significant challenges to the integrity and functionality of these structures, especially in arid and semi-arid regions like Northern Kenya, where these structures often face intense erosion due to minimal vegetative cover, and erodible soil types (COWI, 2018). This significantly undermines the operational lifespan of drainage structures on roads. Road washouts in recent memory have caused several road closures including the Nairobi – Garissa Road which was impassable for a short period in April 2024 due to damaged sections from floods (KBC Digital, 2024).

While the latest road design manuals in Kenya and common practise have identified erosion as a major climatic threat to road infrastructure (Ministry of Roads and Transport, 2025), there is very limited local guidance on the vulnerability analysis of road alignments and drainage crossings to washouts and sediment deposition. Moreover, government investment in opening Northern Kenya through road development necessitates a proactive approach to the integration of erosion risk assessments to avoid costly post-construction mitigation.

This study presents a practical erosion modelling framework that integrates the Stream Power Index (SPI) and the Revised Universal Soil Loss Equation (RUSLE) in a GIS workflow to support erosion assessment during the hydrological analysis phase of road design, prior to the sizing and detailed design of drainage structures. The SPI was also used independently to assess the vulnerability of the road alignment to washouts by identifying high-energy flow paths and gully-prone zones intersecting or running on the carriageway. In parallel, the outputs from SPI and RUSLE were integrated through a Multi-Criteria Decision-Making Analysis (MCDMA) to systematically rank the vulnerability of drainage crossings to sedimentation and hydraulic failure. The methodology was applied to the A14 highway corridor between Wajir and Moyale, offering spatially explicit insights for engineers to guide erosion mitigation, drainage design, and maintenance planning.

2. Study Area

This study was conducted along the A14 highway corridor, focusing on the section between Wajir and Moyale in northern Kenya. This segment of the road spans approximately 240 kilometres with a Gravel surface and it traverses Arid and Semi-Arid Lands (ASALs) characterized by low and erratic rainfall, high evapotranspiration rates, sparse vegetation, and fragile soils, factors that collectively contribute to high susceptibility to erosion. The terrain in the area varies with elevations of approximately 200 m in the Wajir lowlands to over 1,800 m in the Moyale highlands.

The road alignment generally follows a downslope gradient from Moyale to Wajir, cutting across ephemeral streams (laggas) that dominate the hydrological regime in this part of Kenya. The road often runs parallel or skewed to the direction of flow of these laggas, creating multiple interaction points with natural drainage paths. This increases the vulnerability of the alignment to flooding, sediment deposition, and washouts. Hydrologically, the study area falls within the Ewaso Ng'iro North Drainage Basin, specifically within sub-catchments 5EA and 5EB. These sub-catchments form part of a larger transboundary river system that originates in the Ethiopian Highlands and drains toward the Jubba floodplains in southern Somalia (Figure 1).
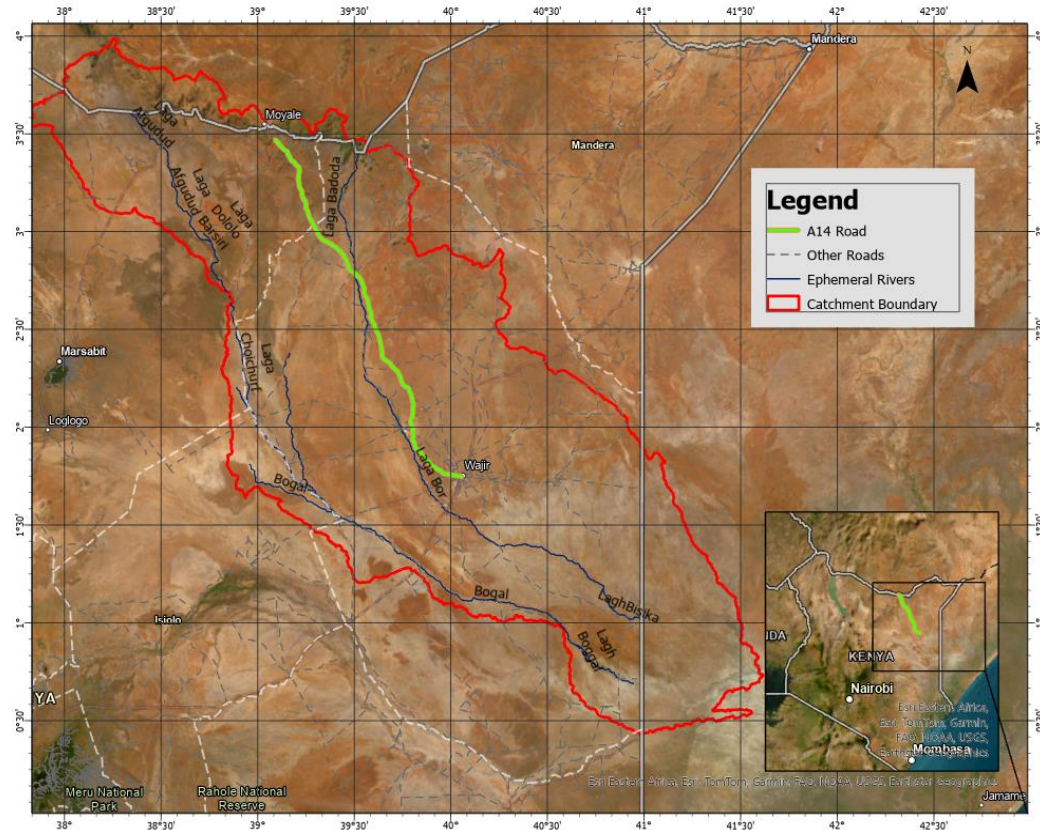
Figure 1: Wajir – Moyale A14 highway layout

Land cover in the area is dominated by shrubland, sparse grassland, and bare soils (Figure 2). Overgrazing and land degradation are common, further reducing ground cover and amplifying erosion risks.
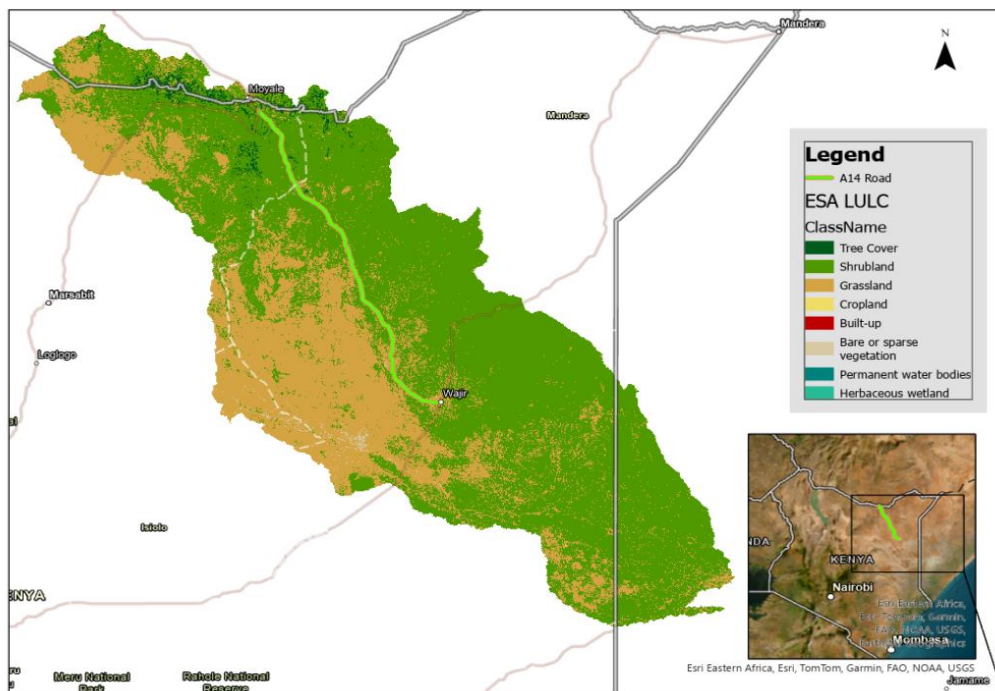
Figure 2: Land Cover of the study area (European Space Agency)

The area is also largely characterised by Sandy Clay Loam soils which have a moderately high runoff potential (Niels & Gicheru, 2004). This soil texture is particularly susceptible to erosion due to poor structure (Zhao, Wen, Wang, & Gao, 2013)

Rainfall typically peaks in April–May and October–November, with annual totals ranging from 360 mm to 610 mm (GIBB, 2016). These climatic and biophysical conditions create an ideal setting to evaluate erosion risk and sediment movement in relation to road drainage infrastructure.

3. Erosion and Sediment Estimation

Soil erosion by water action is the main contributor to siltation and blockage of drainage structures during rainfall events. This is often due to concentrated runoff, steep hydraulic gradients, and absence of protective vegetation (Morgan, 2005). Drainage infrastructure on the A14 road includes culverts and drifts and according to (GIBB, 2016), 50% of the pipe culverts on the road were silted, at the time of their investigations with a majority experiencing half to full siltation. The erosion impacts on sections of the road can be quite severe as shown in Table 1.

Table 1: Erosion impacts on the A14 road

Eroded A14 road section, before Moyale (GIBB, 2016)	Washed - out A14 road section (GIBB, 2016)
Washout around culverts on the A14	Siltation at box culvert entrance on the A14

According to a study by (Muste & Xu, 2017), three (3) major erosion types are critical in sediment production to drainage structures on roads. These are:

- Sheet and Rill Erosion characterised by the uniform detachment and removal of soil, or sediment particles, from the soil surface by overland flow or raindrop impact evenly distributed across a slope (Hairsine & Rose, 1992)
- Gully erosion characterised by the formation of gulleys when runoff from adjacent slopes forms concentrated flows in drainage ways.
- Streambank erosion characterized by widening and deepening of the stream channels.

To model these processes, the Stream Power Index (SPI) was used to identify terrain-driven flow concentration zones with high erosive energy, while the Revised Universal Soil Loss Equation (RUSLE) estimated average annual soil loss from hillslopes. The Sediment Delivery Ratio (SDR) was then applied to convert gross erosion into sediment yield likely to reach drainage structures. All components were integrated within a GIS workflow for spatial analysis and visualization.

3.1. Stream Power Index (SPI)

The Stream Power Index (SPI) is a widely used terrain-based metric that quantifies the erosive potential of overland and concentrated flow. It is derived from digital elevation models (DEMs) and integrates contributing area and slope gradient to estimate the potential energy of surface runoff to cause erosion. Originally proposed by Moore, Grayson, and Ladson (1991), SPI is expressed as:

$$SPI = A_s \cdot \tan \tan (\beta)$$

Where:

- A_s represents the upslope contributing area
- $\tan(\beta)$ is the local slope in radians

In hydrologic modelling, high SPI values are typically associated with steep slopes and large upslope contributing areas, conditions that are favourable for gully erosion, channel incision, and culvert washouts. Conversely, low SPI zones indicate diffuse flow with lower erosive energy. For enhanced visual interpretation, SPI values are often log-transformed, particularly in areas with high topographic variation (Wilson & Gallant, 2000).

3.2. Revised Universal Soil Loss Equation (RUSLE)

The Revised Universal Soil Loss Equation (RUSLE) is a process-based empirical model developed by the USDA Agricultural Research Service to predict long-term average annual soil loss resulting

from rill erosion caused by rainfall and surface runoff. It is an enhancement of the original USLE model, incorporating improved equations for slope, cover, and management practices (Muste & Xu, 2017). The RUSLE equation is formulated as:

$$A = R \cdot K \cdot LS \cdot C \cdot P$$

Where:

- **A** is the predicted average annual soil loss per unit area, expressed in tonnes per hectare per year. (t/ha/yr)
- **R** is the rainfall-runoff erosivity factor, indicating the combined effect of rainfall intensity and potential surface runoff in driving soil erosion. (MJ mm ha-1 h-1 yr-1)
- **K** is the soil erodibility factor, reflecting how easily soil particles can be detached and transported by rainfall and surface water. (t ha h ha^{-1} MJ^{-1} mm^{-1})
- **LS** is the slope length and steepness factor, capturing the influence of terrain gradient and slope extent on erosion risk. (dimensionless).
- **C** is the cover management factor, which adjusts soil loss estimates based on the type and density of vegetation or land cover relative to bare soil. (dimensionless).
- **P** is the support practice factor, accounting for erosion control measures such as contour farming, terracing, or strip cropping that reduce runoff velocity and soil displacement. (dimensionless).

3.3. Sediment Yield

While the Revised Universal Soil Loss Equation (RUSLE) estimates gross annual soil loss from hillslopes, not all eroded material reaches drainage structures. A portion is redeposited along the landscape before exiting the catchment (Walling, 1983).To account for this, a Sediment Delivery Ratio (SDR) is applied to estimate the Sediment Yield (SY), the actual volume of eroded soil that is transported to a specific point. The Sediment Yield is calculated as:

$$Sediment\ Yield(SY) = A \cdot SDR$$

Where:

- A is the gross soil loss from RUSLE (t/ha/yr)
- SDR is the sediment delivery ratio (unitless, typically between 0.05 and 0.6)
- SY is the sediment yield delivered to the drainage outlet (t/ha/yr)

The SDR varies with slope, drainage density, flow length, vegetative cover, and soil texture. Steeper slopes and shorter flow paths typically result in higher SDRs due to reduced opportunities

for deposition, dense vegetation reduces sediment delivery by trapping sediment (Ferro & Mario, 1995). In this study, an area-based model adopted from FAO (n.d.) was used. It relates the SDR inversely to catchment area and is computed as:

$$SDR = 0.565 \cdot A^{-0.125}$$

Where A is the area (km2)

Sediment yield was then converted to volumetric estimates using soil bulk density data to assess clogging risks, flow restrictions and maintenance burden at drainage points.

4. Multi-Criteria Decision-Making for Erosion and Drainage Risk Assessment

Given the complex interplay between topography, soil erosion, hydrologic processes, and infrastructure performance, Multi-Criteria Decision-Making Analysis (MCDMA) offers a robust framework for evaluating erosion-related risks in linear infrastructure systems. Unlike single-variable assessments, MCDMA allows for the integration of multiple geospatial and hydrological indicators, providing a more comprehensive basis for decision-making (Malczewski, 2006). While RUSLE quantifies potential sediment production based on catchment characteristics, and SPI highlights areas prone to concentrated flows and gully erosion (Moore, Grayson, & Ladson, 1991; Wilson & Gallant, 2000), each metric alone captures only part of the erosion risk landscape. Sediment yield, in turn, reflects the actual delivery of eroded material to drainage structures, influencing clogging and maintenance requirements (Walling, 1983; Ferro et al., 1995). Therefore, an integration of these three dimensions offers a more accurate and actionable understanding of risk, particularly for drainage infrastructure along vulnerable corridors.

Recent applications of this integrated approach have demonstrated its effectiveness in road vulnerability mapping (Muste & Xu, 2017). These studies commonly utilize weighted frameworks that reflect the influence of each metric on erosion dynamics, although specific scoring systems vary depending on context.

In this study, the MCDMA framework served as the analytical backbone for evaluating erosion and sedimentation risks at major drainage crossings with a site-specific, spatially explicit impact index that enabled prioritization of mitigation interventions across the A14 road corridor.

5. Methodology

GIS-based mapping was used to generate spatial rasters for each parameter using globally available datasets for the SPI and RUSLE computation (Table 2)

Table 2: Summary of Datasets used

Dataset	Function	Source
SOTWIS Soil Dataset	Soil texture assessment; Estimation of soil bulk density	International Soil Reference and Information Centre (ISRIC) – World Soil Information
TanDEM – X 30m Res DEM	Generation of slope; flow accumulation and drainage area in SPI computation; catchments, flow path and drainage crossing delineation; Estimation of RUSLE Slope Length and Steepness Factor	German Aerospace Center (DLR)
ESA WorldCover 2021 LULC	Land cover assessment; estimation of RUSLE Cover and Management Factors; Estimation of Support Practice factors	European Space Agency (ESA)
ESDAC Global R -Factor	Estimation of RUSLE rainfall erosivity factor	European Soil Data Centre (ESDAC)
ESDAC (GloSEM) Global K – Factor (Wischmeier)	Estimation of RUSLE soil erodibility factor	European Soil Data Centre (ESDAC)

5.1. Catchment Delineation and Flow Path Extraction

The DEM was used to delineate catchments and flow paths in ArcGIS using the standard hydrological tools: Fill, Flow Direction, Flow Accumulation, and Watershed. Major drainage crossings were digitized, and their contributing catchment areas delineated (Figure 3).
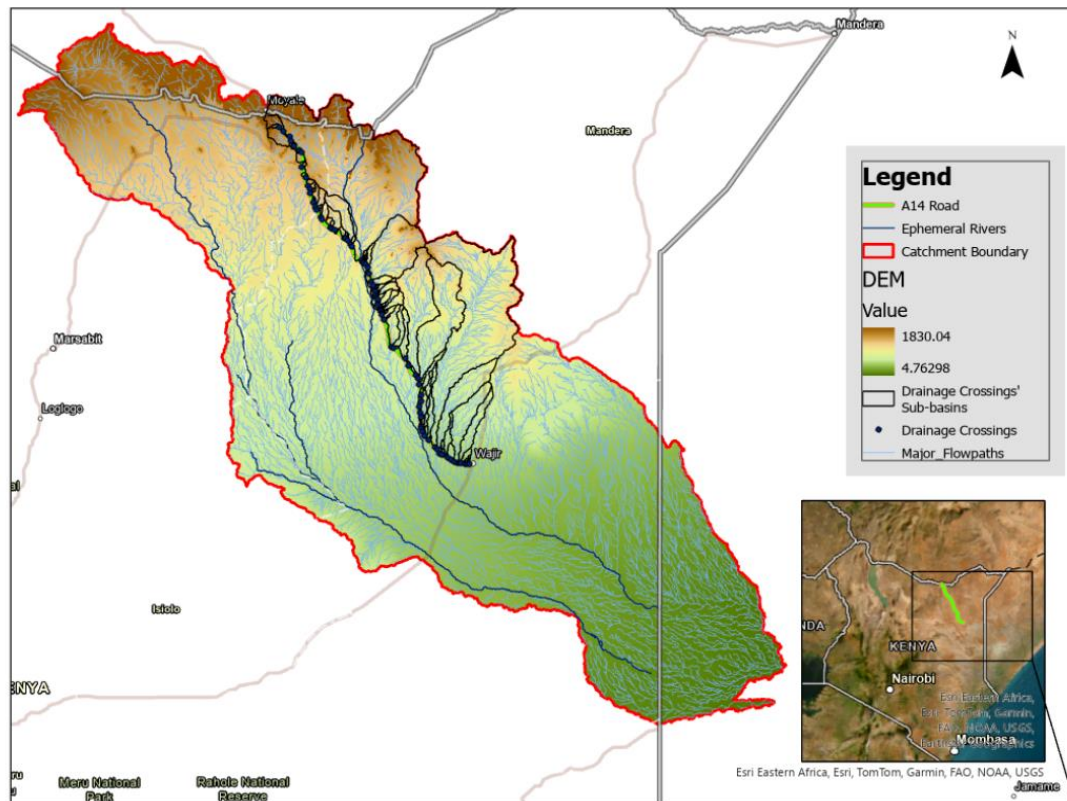
Figure 3: Catchment areas draining to the A14 road corridor

5.2. SPI Raster Generation

Flow accumulation raster, generated from the DEM was converted to a Drainage Area raster by multiplying by the cell size and then multiplied by a raster of the slope tangent to obtain the SPI (Figure 4).

$$SPI = As . Tan (B)$$
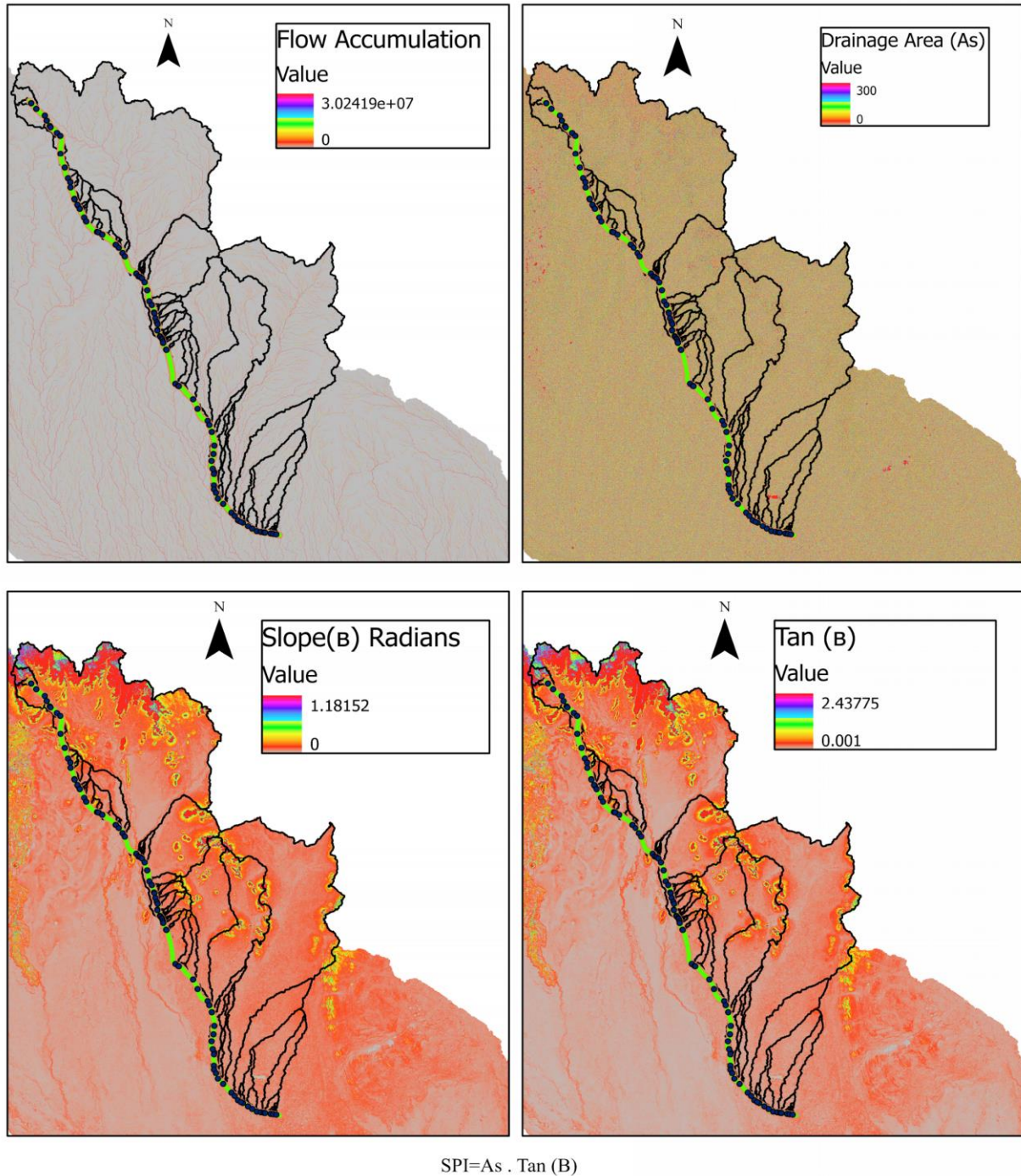
Figure 4: SPI inputs for the A14 road catchments

The Stream Power Index (SPI) values obtained were classified on severity levels based on the resulting ranges in natural logarithm (<0 to >10). Since no universal SPI classification exists, the thresholds were adapted from related literature (Table 3), drawing on general principles from erosion and topographic index studies.

Table 3: Literature informing A14 SPI classification scheme

Reference	Description
Moore et al. (1991)	The authors suggested that SPI values vary widely based on terrain, with higher values in steep, high-flow areas and proposed qualitative groupings (e.g., low to high erosion potential) without fixed thresholds, supporting the use of data-driven or context-specific classes like quantiles or ranges.
Wilson, J. P., & Gallant, J. C. (2000)	The authors recommended classifying terrain indices based on statistical distributions (e.g., quantiles) or physical thresholds tied to erosion processes. They noted SPI values increase logarithmically with flow concentration and slope.
Mitasova et al. (1996)	The authors suggested classifying SPI into risk categories based on terrain and flow characteristics, with higher SPI indicating channelized erosion.

The classification scheme for the SPI values used is shown in Table 4.

Table 4: Adopted Severity Classification for SPI

SPI Range	Erosion Severity Risk Classification
-6 to 0	Low
0 to 5	Moderate
5 to 10	High
>10	Severe

5.3. RUSLE Computation

5.3.1. Rainfall- Runoff Erosivity Factor (R)

The erosivity factor is the most sensitive parameter in RUSLE computation, influencing approximately 80% of the total soil loss (Watene, et al., 2021). It is typically computed based on the kinetic energy of rainfall drops and the maximum 30-minute rainfall intensity, in the EI30 method (Wischmeier & Smith, 1978). The method defines R as the sum of the product of total storm energy (E) and the maximum 30-minute rainfall intensity (I_{30}) for each erosive rainfall event in a year in the equation:

$$R = \sum_{k=1}^{n} (E_k . I_{30,k})$$

Where:

- R is the annual rainfall erosivity factor (MJ mm ha-1 h-1 yr-1)
- Ek is the total kinetic energy of a rainfall event k (MJ/ha)
- I30, k is the maximum 30-minute rainfall intensity for an event k (mm/hr)
- n is the number of erosive rainfall events in a year

This study adopted the global erosivity dataset by the European Soil Data Center (ESDAC), clipped to the study area (Figure 5), due to limited long term granular rainfall data in the area.
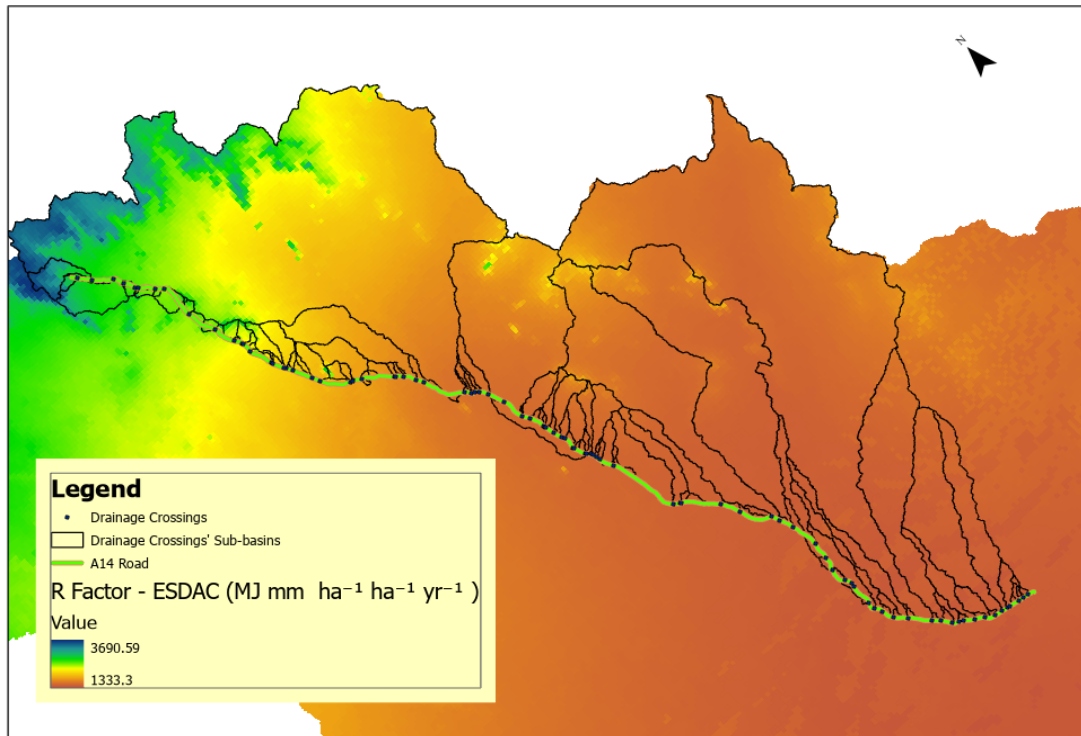
Figure 5: RUSLE R Factor raster for the A14 road study area

The erosivity ranged in the study area ranged from 1333 *MJ mm ha⁻¹ h⁻¹ yr⁻¹* to 3690.6 *MJ mm ha⁻¹ h⁻¹ yr⁻¹* with a mean erosivity of 1803.5 *MJ mm ha⁻¹ h⁻¹ yr⁻¹*.

5.3.2. Soil Erodibility Factor (K)

The soil erodibility factor in this study (Figure 6) was derived from ESDAC's global dataset estimated by the Wischmeier & Smith (1978) method. The method is based on on the soil texture, organic matter content and permeability represented by the equation.

$$K = \frac{0.1317 \times \left(2.1 \times 10^{-4} \times (M^{1.14}) \times (12 - a) + 3.25 \times (b - 2) + 2.5 \times (c - 3)\right)}{100}$$

Where:

- K is the Soil erodibility factor (t ha h ha⁻¹ MJ⁻¹ mm⁻¹)
- M is the product of the percentage of silt and very fine sand and the percentage of sand.
- a is the percentage of organic matter content.
- b is the soil structure code (assigned values from 1 to 4).
- c is the soil permeability code (assigned values from 1 to 6).

The ESDAC dataset was developed as part of the Global Soil Erosion Modelling (GloSEM) project using soil data from International Soil Reference and Information Centre (ISRIC) (Panagos P. , et al., 2014).
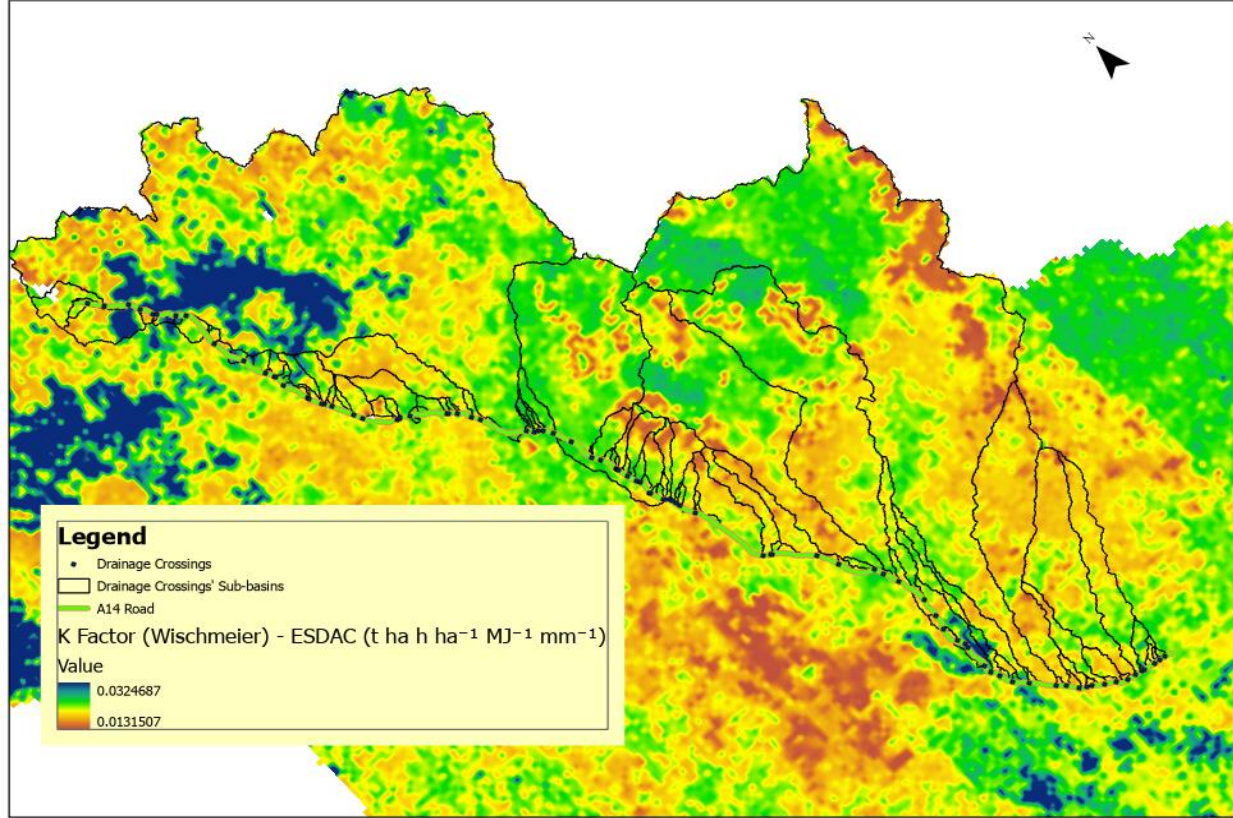
Figure 6: RUSLE K Factor raster for the A14 road study area

The soil erodibility values in the area ranged from 0.01 *t ha h ha⁻¹ MJ⁻¹ mm⁻¹*. to 0.03 *t ha h ha⁻¹ MJ⁻¹ mm⁻¹* with a mean of 0.02 *t ha h ha⁻¹ MJ⁻¹ mm⁻¹*.

5.3.3. Slope Length and Steepness Factor (LS)

The LS factor, representing the combined effect of slope length (L) and slope steepness (S) on soil erosion, was computed based on the Moore and Burch (1986) formulation represented by the following equation.

$$LS = \left(\frac{Flow\ Accumulation \cdot Cell\ Size}{22.13}\right)^m \cdot \left(\frac{sin\ sin\ (\theta)}{0.0896}\right)^n$$

Where:

- θ is the slope in radians.
- m is an index reflecting how erosion increases with slope length.
- n is an index controlling how sensitive the LS factor is to slope steepness (typically 1.3)

The m index (Figure 7) was computed based on the slope using a classification scheme informed by Renard et al. (1997) and McCool et al. (1987) which varies the m index with the percentage slope (Table 5).

Table 5: LS factor m-Index slope-based classification

Slope (%)	m-Index value
0 – 1%	0.2
1 – 3%	0.3
3 – 5%	0.4
5 – 10%	0.45
10 – 20%	0.5
20 – 30%	0.55
>30%	0.6
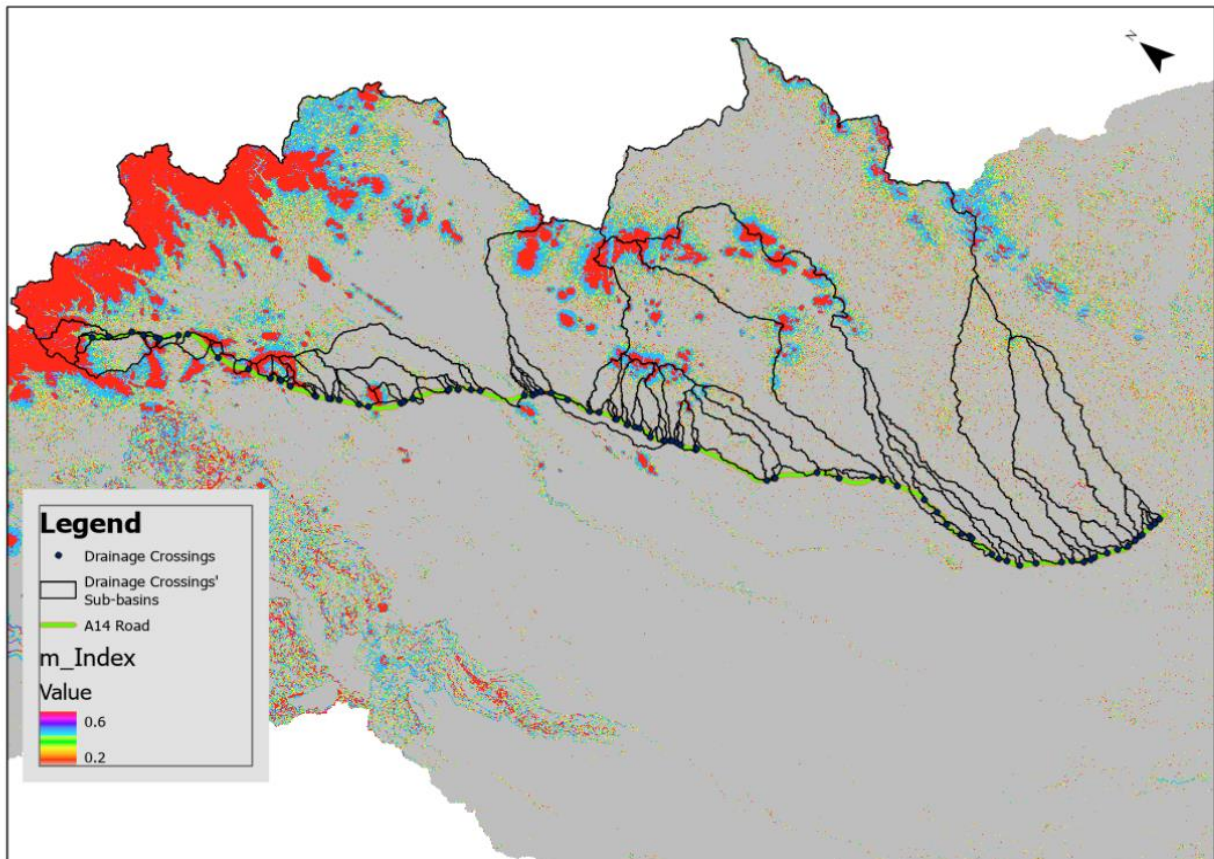
Figure 7: m- index raster for the A14 road study area

The LS factor raster computed is shown in Figure 8.
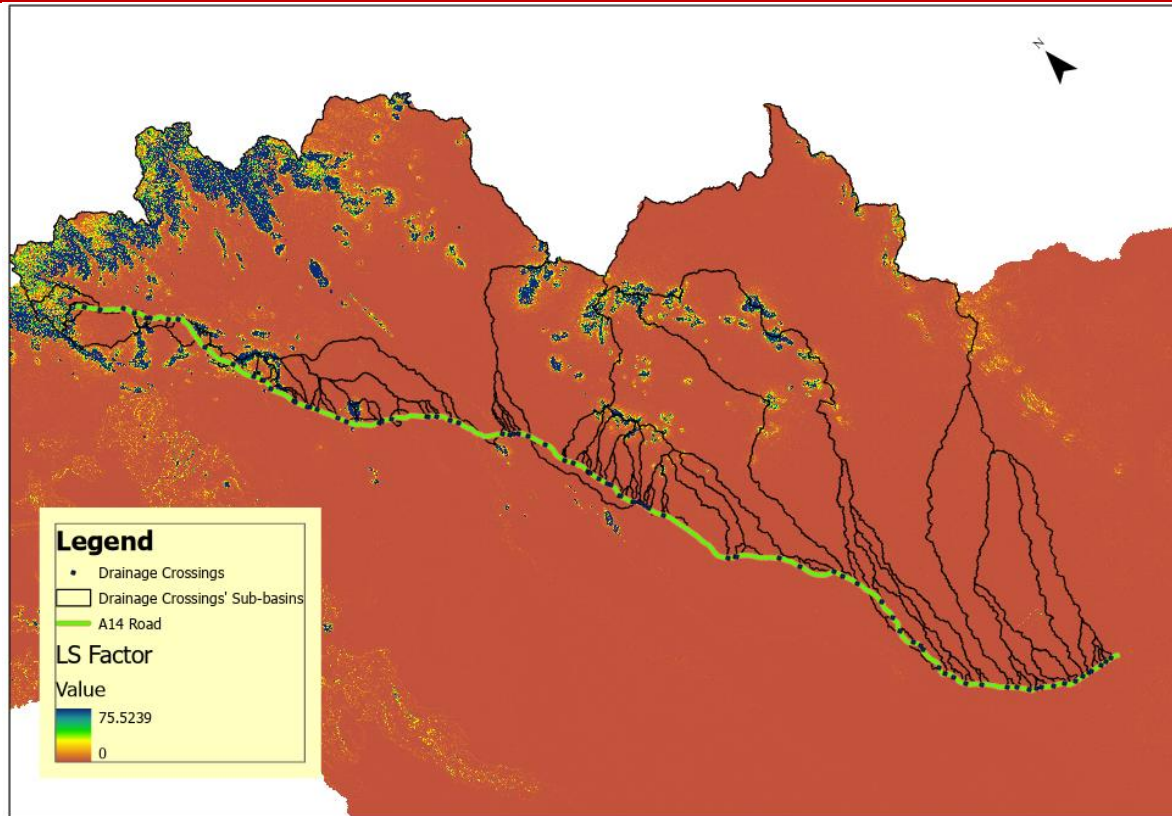
Figure 8: RUSLE LS Factor raster for the A14 road study area

The LS factor ranged from 0 to 75 with a mean of 0.3 across much of the study area

5.3.4. Cover and Management factor (C)

A cover and management factor raster for the area (Figure 9) was estimated based on the study area's land cover (Figure 2) using mean values from the classification scheme in Table 6.

Table 6: C Factor classification scheme based on the ESA World Cover dataset

ESA Code	LULC Class	Typical C-Factor	Reference
10	Tree Cover	0.001–0.05	Renard et al. (1997); Panagos et al. (2015); Wischmeier & Smith (1978)
20	Shrubland	0.01–0.05	Ganasri & Ramesh (2016); Panagos et al. (2015)
30	Grassland	0.01–0.15	Wischmeier & Smith (1978); Renard et al. (1997); Ganasri & Ramesh (2016)
40	Cropland	0.1–0.4	Wischmeier & Smith (1978); Renard et al. (1997)
50	Built-up Area	0.05–0.2	Panagos et al. (2015); Ganasri & Ramesh (2016)
60	Bare / Sparse Vegetation	0.4–0.6	Renard et al. (1997); Panagos et al. (2015); Ganasri & Ramesh (2016)
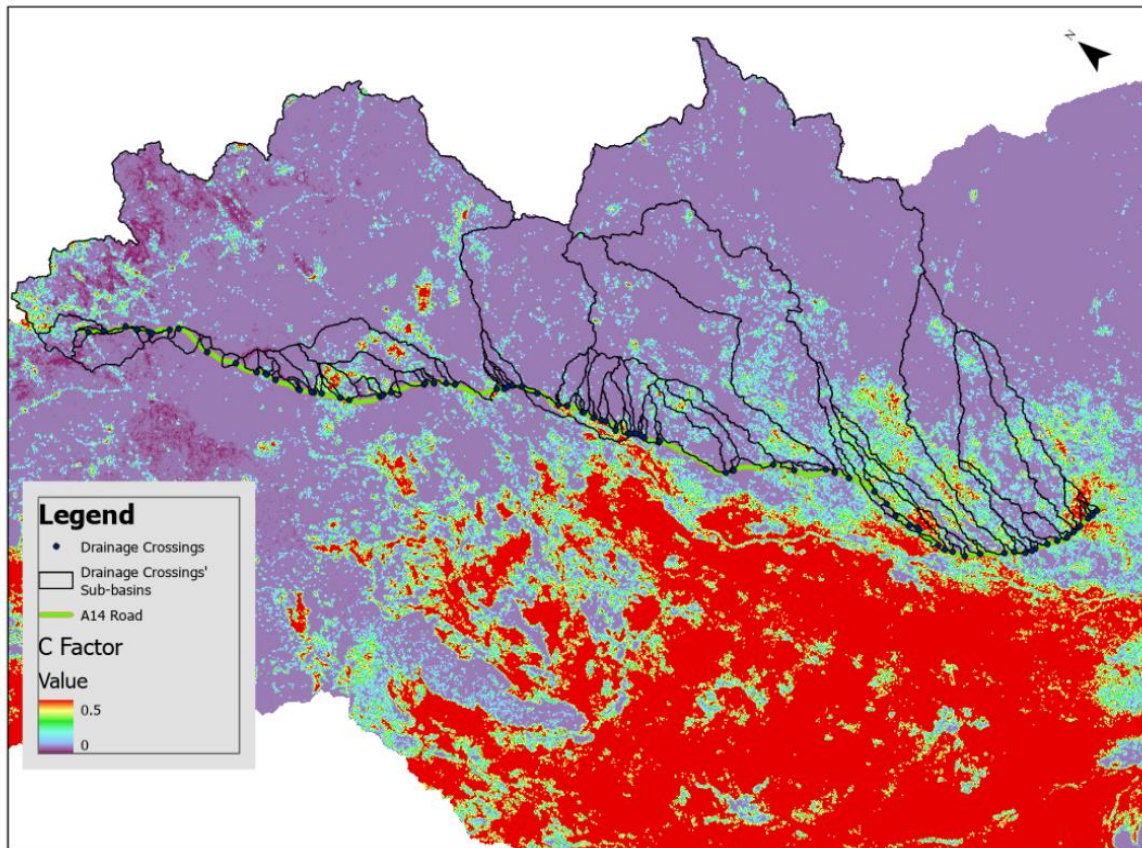
Figure 9: RUSLE C Factor raster for the A14 road study area

The C Factor values ranged from 0 to 0.5 with a mean of 0.04 across the catchments.

5.3.5. Support Practice Factor (P)

The study area dominated by pastoralism, rangelands, and some cropland, has limited to no formal conservation practices. Natural features such as vegetation patches, soil crusts were assumed to mimic support practices as shrubs and grass intercept falling raindrops limiting erosion in the immediate areas (Ludwig et al., 2005). The factor (Figure 10) was estimated on the study area's land cover (ESA dataset in Figure 2) using the classification scheme in Table 7 with the P values estimated for the land cover classes based on studies by Renard et al. (1997); Panagos et al. (2015); Wischmeier & Smith (1978) and Morgan, R. (2005).

Table 7: P Factor classification scheme based on the ESA World Cover dataset

	LULC Class	Estimated P Value	Description
10	Tree Cover	0.6	Dense canopy intercepts rainfall reduces runoff. Scattered woodlands in Moyale provide moderate protection.

20	Shrubland	0.8	Shrubs (common in Moyale) reduce splash erosion and runoff, but sparse cover limits effectiveness.
30	Grassland	0.9	Pastoral rangelands dominate Moyale; grass reduces runoff slightly, but grazing may degrade cover.
40	Cropland	0.7	Small-scale farming (e.g., sorghum) may use ridging or contouring, reducing erosion compared to bare soil.
50	Built-up Area	1.0	Impervious surfaces increase runoff; minimal in Moyale, assume no erosion control.
60	Bare / Sparse Vegetation	1.0	Exposed soil or rocky areas (common in degraded Moyale zones) offer no erosion protection.
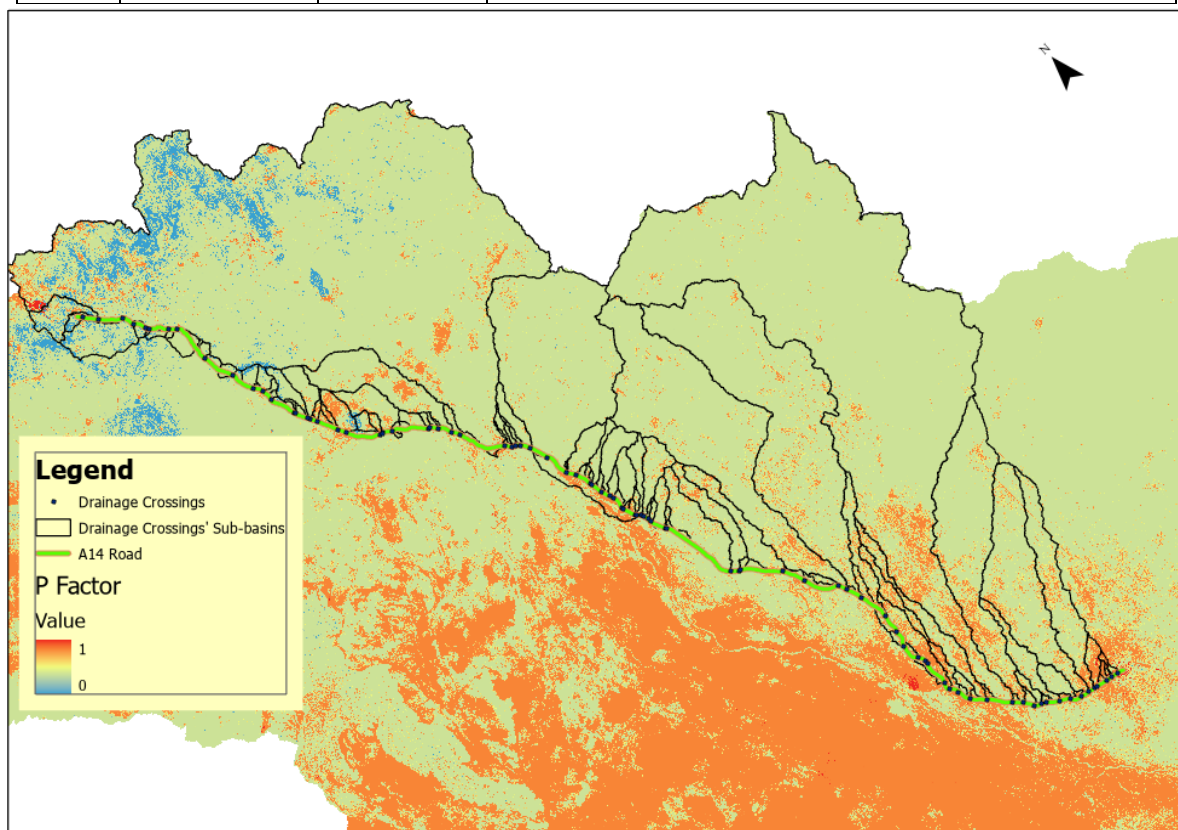
Figure 10: RUSLE P Factor raster for the A14 road study area

The mean P factor in the study area was 0.8 across the catchments, indicating slight impact of the vegetation cover on erosion.

5.3.6. Catchment Erosion Classification

To better interpret the severity of erosion risks, the RUSLE-derived annual soil loss rates were classified into six severity categories (Table 8). This scheme was adapted from Watene et al. (2021). The classification provided a nuanced scale that aligns well with observed erosion processes and their implications for road infrastructure:

Table 8: RUSLE Erosion severity classification

RUSLE erosion (t/ha/yr)	Erosion Severity Class
0 – 5	Slight
5 - 10	Moderate
10 - 20	High
20 - 40	Very High
>40	Severe

This framework allowed for prioritization of catchments for erosion control interventions, with "Very High" to "Very Severe" zones requiring urgent and possibly structural erosion mitigation measures especially where SPI or SDR values confirm high erosive energy or delivery potential.

5.3.7. Sediment Yield

The estimated catchment-wise annual erosion was multiplied by the SDR computed for the catchments to approximate the sediment reaching each identified drainage crossing. The sediment yield in tonnes was converted to mass in kilograms and used to estimate sediment volume at major drainage crossings based on bulk density from the SOTWIS dataset. The following equation was used:

$$Sediment\ Volume\ at\ drainage\ crossing(m3/y) = Mass(Kg/yr)/BulkDensity(kg/m3)$$

The impact of estimated annual sediment volumes on the performance of drainage structures was assessed using a classification scheme (Table 9) derived from hydrological engineering literature and international drainage design guidelines. This classification reflects the operational consequences of sediment deposition in culverts, relief drains, and channels, particularly under conditions typical of arid and semi-arid environments such as northern Kenya.

Table 9: Sediment Volume impact classification

Sediment Volume (m³/year)	Impact Level	Description	Reference
<1,000	Low	Small sediment volumes cause minimal deposition, maintaining culvert flow capacity. Low risk of blockages, structural damage, or environmental impact. Routine maintenance is sufficient.	USDA Forest Service (1997)

Sediment Volume (m³/year)	Impact Level	Description	Reference
1,000–5,000	Moderate	Moderate sediment volumes may cause partial blockages, reduce flow capacity and increase upstream ponding or downstream erosion. Regular monitoring and maintenance (e.g., sediment traps) are needed.	Ontario Ministry of Natural Resources (2019); Xu et al. (2019)
5,000–15,000	High	High sediment volumes significantly reduce flow capacity, increasing risks of flooding, scour, and crossing failure. Requires larger culverts, sediment traps, and frequent maintenance.	USDA Forest Service (1997)
>15,000	Severe	Very high sediment volumes lead to complete blockages, flooding, and potential culvert washout. Severe environmental impacts (e.g., habitat loss) necessitate oversized culverts or bridges and major redesign.	Food and Agriculture Organization (n.d.); Melbourne Water (2021)

This framework was developed to bridge modelled sediment yields with design and maintenance implications.

5.4. Multi-Criteria Decision-Making Framework

To objectively prioritize drainage crossings and potential hydrodynamic impact along the A14 corridor, a Multi-Criteria Decision-Making Analysis (MCDMA) framework was developed to integrate key erosion and hydraulic indicators from the SPI, estimated soil loss from RUSLE, and sediment yield to drainage crossing. This was also done to inform mitigation planning tailored to the impact levels.

The approach reflects a systems-based evaluation of sediment-related vulnerabilities, consistent with best practices in hydrological risk management (Malczewski, 2006). Assumptions made in the process were that SPI and RUSLE outputs are correlated but distinct contributors to impacts at drainage crossings and that site-specific parameters such as drainage structure size, slope, or land use are adjustable.

A weighting system was created with each metric assigned a weight reflecting its relative influence on hydrodynamic performance. The weights were informed by literature shown in Table 10 below.

Table 10: A14 MCDMA Weight classification

Metric	Weight	Description
SPI	0.4	Stream power directly affects hydraulic energy and erosion at drainage points. (Moore et al. (1991); FHWA (2006))
RUSLE Soil Loss	0.3	Catchment erosion represents sediment production in the catchment; influences long-term sediment supply but is less immediate than SPI in affecting crossing dynamics. (Wischmeier & Smith (1978); Renard et al. (1997))
Sediment Yield	0.3	Directly quantifies deposition risk and blockage at crossings, critical for assessing blockage and flow impacts. (Al Mamari et al. (2022); Iqbal & Bin Riaz, (2024))

The weights were normalized to sum to 1.0 to ensure a balanced composite score. Each input variable was discretized based on the severity classes used in their computations (Table 11).

Table 11: Summary Severity Classes for SPI, RUSLE and Sediment Yield impacts on drainage crossings

Severity Class	Description
1	Low/Slight
2	Moderate
3	High
4	Very High (RUSLE only)
5	Severe

A composite impact score was calculated using a weighted average:

$$Composite\ Score = (0.4 \times SPI\ Score) + (0.3 \times RUSLE\ Score) + (0.3 \times Sediment\ Yield\ Score)$$

The resulting composite scores were classified into hydrodynamic impact levels based on thresholds shown in Table 12 below:

Table 12: Hydrodynamic impact level classification and possible mitigation measures

Composite Score Range	Hydrodynamic Impact Level	Expected Impacts	Possible Mitigation Measures
1.0–2.0	Low	Minimal restriction or sedimentation; low risk of failure	Routine inspection and debris removal
2.1–3.0	Moderate	Partial flow restriction, minor scour, and local sediment buildup	Regular maintenance, sediment traps / check dams
3.1–4.0	High	Substantial sediment accumulation; possible blockage and flooding	Energy dissipators, sediment traps, upsized drainage structures and frequent monitoring
4.1–5.0	Severe	Blockage or overtopping likely; risk of culvert washout and severe downstream impact	Energy dissipators, upsized drainage structures, robust sediment control, upstream erosion control, frequent monitoring

6. Results

6.1. SPI Output

The resulting SPI raster obtained is shown in Figure 11 below.
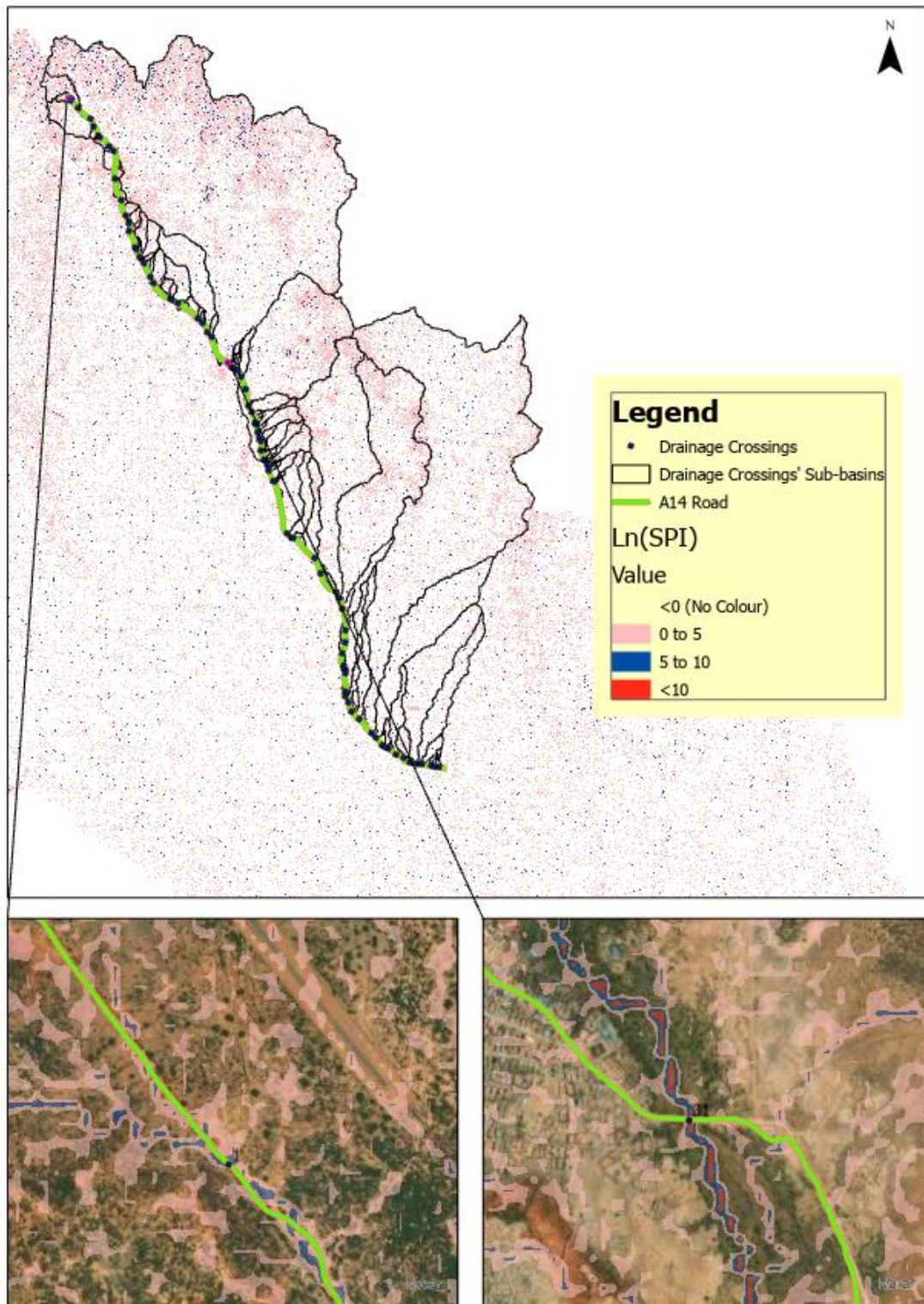
Figure 11: Computed SPI raster

The SPI values, classified by natural logarithm ranged from -6 to 15. Based on the SPI severity classification, 65 major drainage crossing points were identified to be situated in "High" risk gully erosion zones, 12 on "Severe", 6 on "Moderate" and 4 on "Low" risk erosion zones (Figure 12).
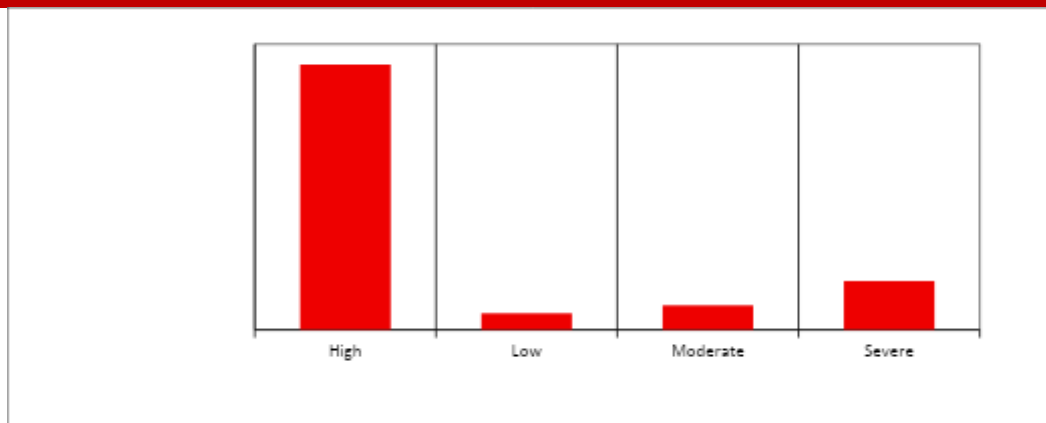
Figure 12: Gully Erosion Risk Severity profile of major drainage crossings on the A14 road

Very High SPI values coincided with steep terrain and converging major flow paths. These areas showed visible signs of head cutting and erosion.

6.1.1. Road Washout Risk Zones

Several segments (Table 13) on the road alignment were identified as exposed to elevated erosion and washout risks based on the SPI analysis. Notably, the stretches between Km 230+000 to Km 240+000 and Km 220+000 to Km 225+000 were intersected by concentrated flow paths classified as having high to very high erosion potential. In the absence of realignment, constructing a new embankment along the existing corridor would make the newly constructed sections significantly vulnerable. Moreover, drainage infrastructure in these zones would be likely to experience rapid sediment deposition, diminishing hydraulic capacity.

The segment from Km 210+000 to Km 220+000 was characterized by numerous perpendicular high-risk flow paths, associated with relatively short flow lengths and limited catchment areas. While the topography may not necessitate major drainage crossings, the reliance on small relief culverts in these areas could be problematic and without appropriate mitigation, such culverts would be prone to clogging. To maintain embankment durability, shoulder slope protection or structural reinforcement would be essential in these areas.

Additionally, the section between Km 105+000 and Km 145+000 had widespread flow concentration directly along the alignment, including multiple high-risk erosion pathways that are sharply skewed. These areas would require targeted erosion control and cross-drainage interventions.

Table 13: Washout risk road sections on the A14 road

SPI Risk Zones Overview	Satellite Image Overview
Km 230 +000 to Km 240+000	Km 220+000 to Km 225
Km 210+000 to Km 220+000	Km 105+000 to Km 145+000

6.2. RUSLE Output

The individual raster for RUSLE parameters were multiplied in GIS to obtain the potential annual erosion rates shown in Figure 13.
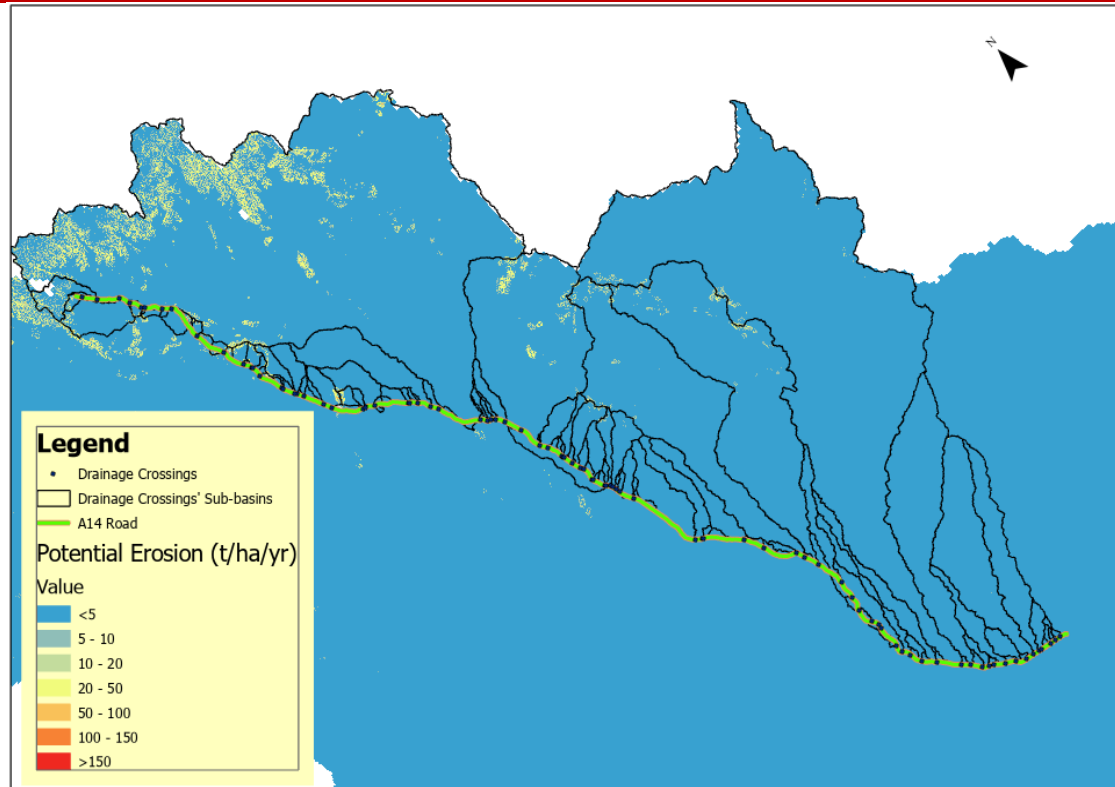
Figure 13: RUSLE Erosion raster for the A14 road study area

Estimated annual soil loss rates across the study area showed marked spatial variability, ranging from less than 5 t/ha/yr in areas with stable vegetation cover and gentle slopes, to more than 150 t/ha/yr in zones characterized by steep gradients and degraded land cover. The mean erosion rate was calculated at 9.78 t/ha/yr, indicating an overall moderate erosion potential across the entire area.

The Sediment Delivery Ratios (SDRs) varied between 0.2 and 0.5, suggesting moderate sediment connectivity between the hillslopes and downstream drainage points. These values reflected the influence of landscape features such as slope length, vegetation cover, and flow concentration, which facilitate partial transport of eroded materials to roadside structures. As such, sediment deposition at culverts and drainage channels is expected to be significant in several catchments, potentially increasing maintenance frequency or requiring structural intervention.

Analysis of the RUSLE outputs using the adopted classification scheme revealed a clear skew toward lower erosion severity across most catchments (Figure 14). Out of the total evaluated catchments, 67 were categorized as "Slight", indicating soil loss rates below 5 t/ha/yr and minimal concern for structural sedimentation. However, 4 catchments fell within the "High" erosion profile (10–20 t/ha/yr), and 10 were identified as "Very High" (20–40 t/ha/yr).
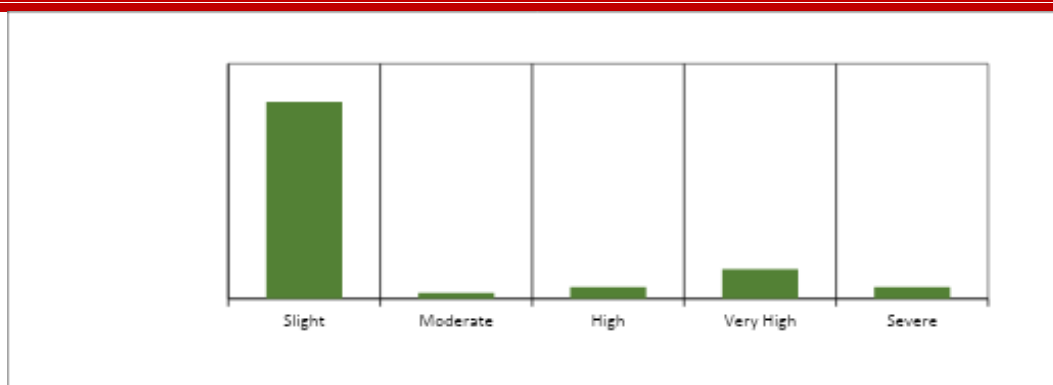
Figure 14: Catchment Erosion Risk profile for major drainage crossings on the A14 road

More critically, 4 catchments exhibited "Severe" erosion (40–80 t/ha/yr), and 2 were classified as "Moderate", while none exceeded the "Very Severe" threshold (>80 t/ha/yr). These areas represent priority zones for erosion control, where both structural (e.g., sediment traps, inlet protection) and non-structural (e.g., vegetation buffers, land use management) interventions may be required.

Sediment Volumes to the drainage crossings ranged from less than 1 m3/yr to 815,092 m3/yr, with an average normalized sediment volume per catchment of 160 m3/yr/km2. The expected impact of sediment volumes delivered to the drainage crossings was identified as "Severe" at 8 points, "High" at 8 points, "Moderate" at 16 crossings and "Low" at a majority 55 drainage crossings (Figure 15).
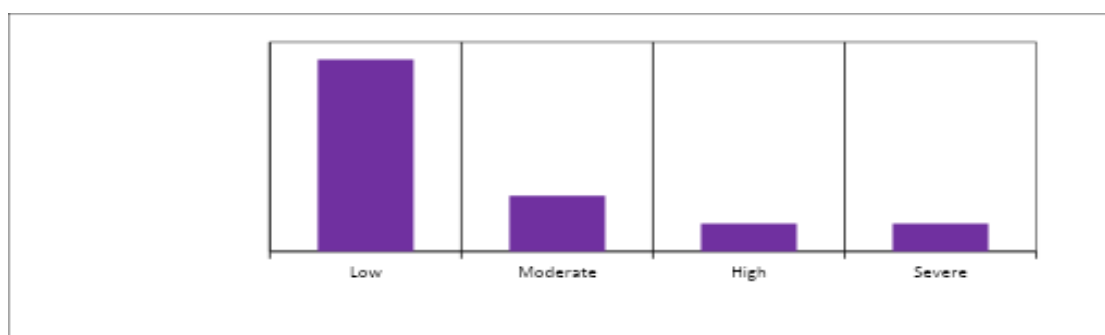
Figure 15: Drainage Impact profile due to sediment volumes for major drainage crossings on the A14 road

This statistical distribution underscores that while most of the alignment lies within areas of low to slight erosion hazard, targeted erosion control is crucial in specific hotspots to preserve drainage function and road durability when the road is eventually constructed to a tarmac pavement.

6.3. MCDMA Output

Fourteen (14) critical drainage crossings with "High" to "Severe" impacts were identified based on the composite scores from the MCDMA framework. Table 14 below, shows the critical drainage crossings based on the combined classified effects of catchment erosion potential from RUSLE, sediment volumes and the erosive potential from SPI.
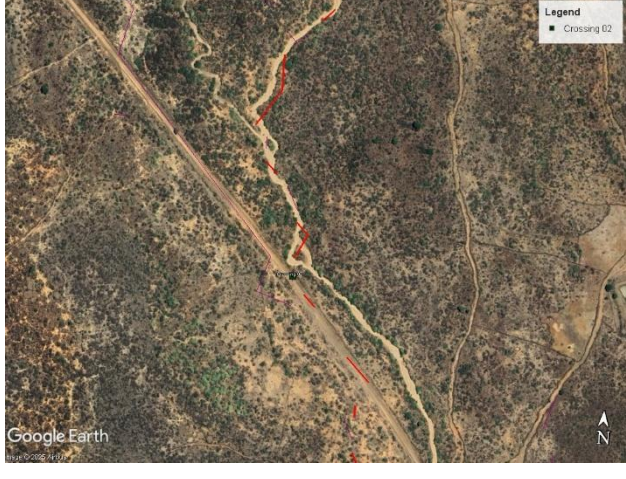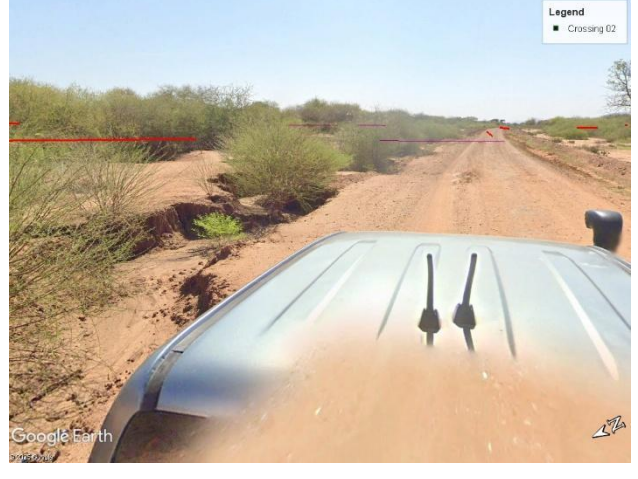
Table 14: Summary of identified critical drainage crossings on the A14 road
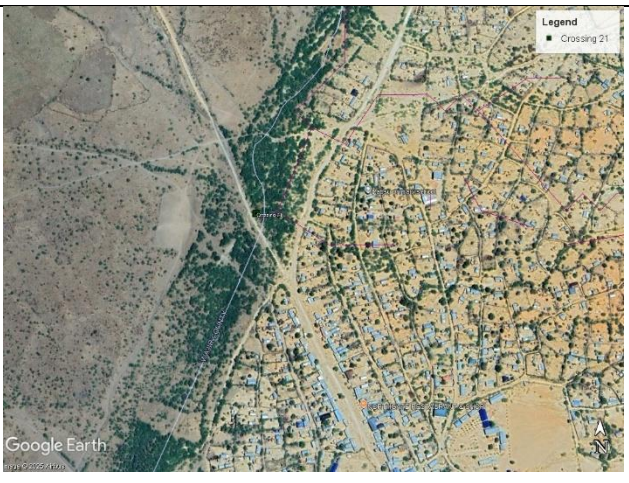
Crossing ID	RUSLE Score	SY Score	SPI Score	Composite Score	Overall Hydrodynamic Impacts
1	5	3	3	3.6	High
2	5	5	3	4.2	Severe
4	3	5	5	4.4	Severe
10	4	3	3	3.3	High
11	5	3	2	3.2	High
12	4	3	3	3.3	High
18	4	3	3	3.3	High
21	4	5	3	3.9	High
23	5	3	3	3.6	High
31	4	5	5	4.7	Severe
37	2	5	5	4.1	Severe
61	1	5	5	3.8	High
62	1	5	5	3.8	High
74	1	5	5	3.8	High
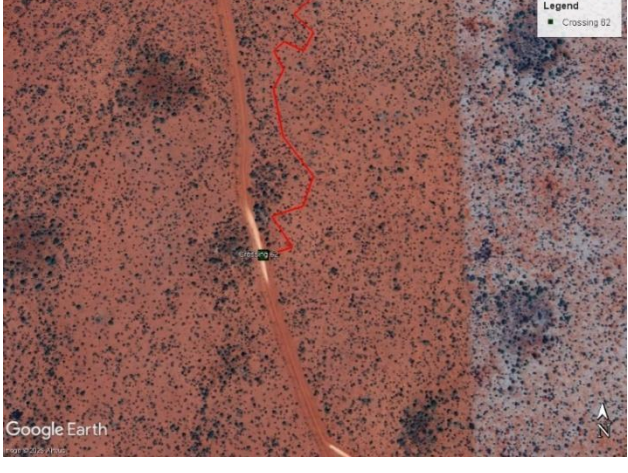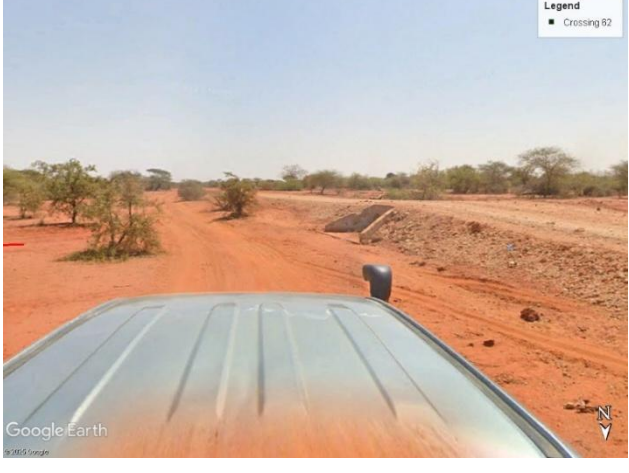
The impacts were compared to satellite imagery and ground pictures (based on Google Open Street Map) with very good correlation to the existing conditions on the road as shown in Table 15.

Table 15: Visualization of sampled critical drainage crossings on the A14 road

ID	Satellite Image Overview	Open Street Map Picture
1		

ID	Satellite Image Overview	Open Street Map Picture
2		
4		
11		

ID	Satellite Image Overview	Open Street Map Picture
12		
21		
23		

ID	Satellite Image Overview	Open Street Map Picture
31		
37		
62		

In addition, 22 drainage crossing points were classified as having "Moderate" hydrodynamic impacts and 51 as "Low" (Figure 16).
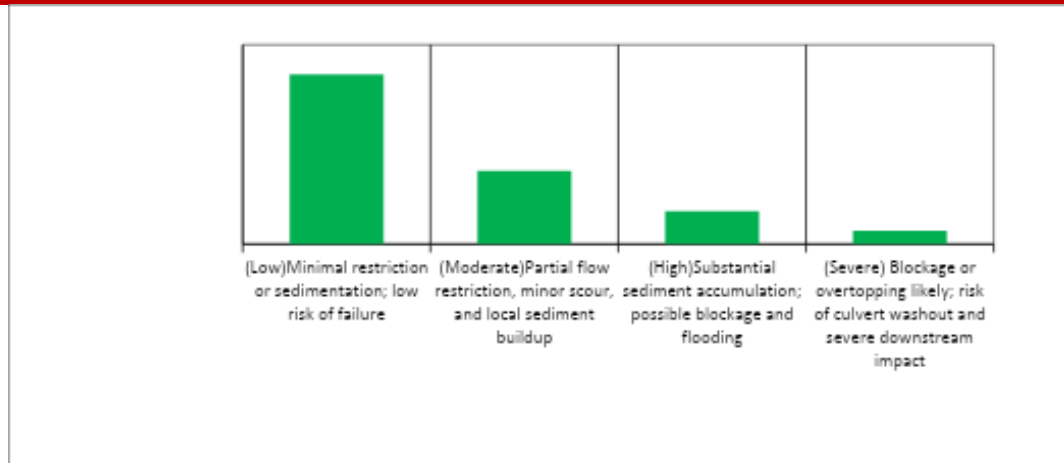
Figure 16: MCDMA Composite Hydrodynamic impacts on drainage crossings on the A14 road

Mitigating interventions, proposed in the MCDMA were assigned to all the drainage crossings based on the hydrodynamic impact levels (Figure 17).
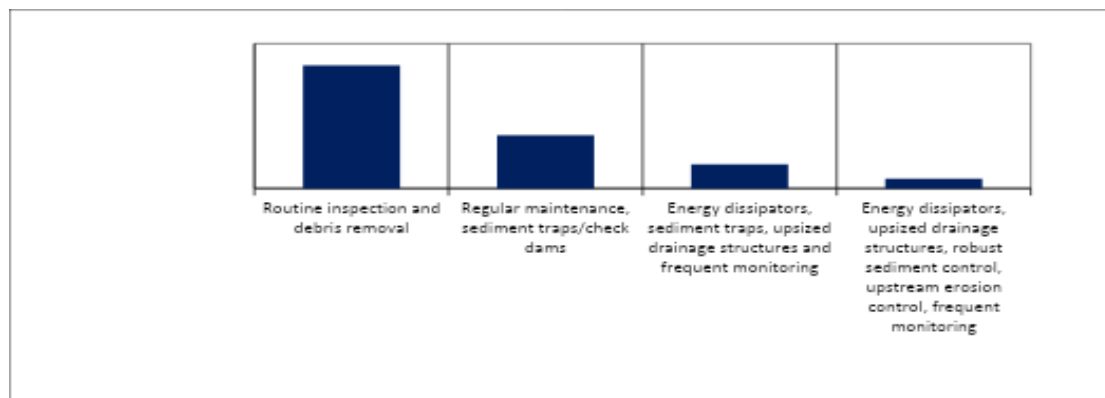
Figure 17: Priority assigned potential mitigation measures to drainage crossings

6.4. Limitations and Challenges

Several challenges were encountered during this study. Firstly, the datasets used originated from different sources and resolutions, requiring extensive preprocessing and resampling to achieve a uniform spatial resolution suitable for raster - based modelling. Secondly, key parameters such as the m-index in the LS factor, the cover management (C) and support practice (P) factors in RUSLE, and the rainfall-runoff erosivity (R) and soil erodibility (K) factors had to be estimated using classification schemes and literature-derived values due to the absence of locally calibrated data. This introduces uncertainty in model outputs and highlights the need for field - based validation in future studies.

Additionally, there is currently no local precedent in Kenya for applying the Multi-Criteria Decision-Making Analysis (MCDMA) approach in erosion modelling for road drainage. As such, the weighting and classification systems had to be adapted from international literature, requiring careful contextual interpretation. Similarly, sediment impact severity classes and SPI/RUSLE thresholds were developed for this

study in the absence of national benchmarks. These challenges underscore the importance of developing localized datasets, validation protocols, and institutional standards to strengthen the reliability and policy relevance of erosion modelling frameworks in infrastructure planning.

7. Conclusions

This study demonstrates the application of a GIS-based erosion assessment framework integrating SPI, RUSLE, and sediment yield estimation to support the hydrological analysis of road infrastructure in arid and semi-arid environments. Through the Multi-Criteria Decision-Making Analysis (MCDMA), critical drainage crossings and erosion-prone alignment segments were identified, allowing for objective prioritization of interventions. The results indicate that a significant proportion of the A14 highway corridor is subject to moderate to severe erosion risk, with localized hotspots requiring urgent structural and non-structural mitigation. The integrated approach bridges the gap between hydrological modelling and practical engineering design by introducing spatially-referenced erosion metrics early in the planning phase. It is scalable, adaptable, and particularly suitable for regions where ground data is limited but climate pressures on infrastructure are increasing.

8. Recommendations

Recommendations from this study include the development of locally calibrated parameters for all components of the RUSLE model, including the C, P, K, and SDR factors, through further field-based research tailored to the unique conditions of arid and semi-arid lands (ASALs) in Northern Kenya. There is also a need to integrate terrain- and hydrology-based erosion modelling tools, such as the Stream Power Index (SPI) and RUSLE, into standard hydrological modelling workflows used in the design phase of drainage infrastructure.

Further research is recommended to validate and refine the applicability of the Multi-Criteria Decision-Making Analysis (MCDMA) framework, particularly in its role in prioritizing drainage interventions and informing the formulation of long-term road maintenance and monitoring plans. Additionally, updates to national road design manuals should be considered, guided by this and future studies, to embed erosion and sedimentation risk metrics in the planning and design of resilient infrastructure, especially in vulnerable regions such as the ASALs of Northern Kenya and others with similar erosion risk profiles.

The study further recommends the use of high-resolution remote sensing tools and UAVs for real-time erosion monitoring and validation of model predictions in remote or insecure areas. Development of standardized erosion risk maps along critical road corridors, using the SPI-RUSLE framework, can enhance proactive route planning and environmental assessments. National and county-level infrastructure institutions should also establish data-sharing protocols among agencies dealing with roads, soils, hydrology, and climate to improve access to critical modelling inputs.

In addition, future research should explore the use of the Modified Universal Soil Loss Equation (MUSLE) as a complementary or alternative approach to RUSLE, particularly for modelling event-based erosion associated with specific design storms. Incorporating MUSLE into erosion assessment workflows may improve the accuracy of sediment yield estimates used in drainage structure sizing, especially where event-based design is preferred over long-term averages.

Lastly, future studies should incorporate downscaled climate change scenarios to evaluate how intensifying rainfall patterns might influence erosion risks, and integrate erosion vulnerability scores into feasibility, cost-benefit, and life-cycle analyses of road investments.

References

Al Mamari, M. M., Kantoush, S. A., Al-harrasi, T. M., & Al-Maktoumi, A. (2022). Assessment of sediment yield and deposition in a dry reservoir using field observations, RUSLE and remote sensing: Wadi Assarin, Oman. *Journal of Hydrology, 617*(1), 128982. doi:10.1016/j.jhydrol.2022.128982

Angima, S. D., Scott, D. E., O'Neill, M. K., Ong, C. K., & Weesies, G. A. (2003). Soil erosion prediction using RUSLE for central Kenyan highland conditions. *Agriculture, Ecosystems & Environment, 97*(1-3), 295-308. doi:10.1016/S0167-8809(03)00011-2

Borelli, P., Ballabio, C., Yang, J., Robinson, D., & Panagos, P. (2022). GloSEM: High-resolution global estimates of present and future soil displacement in croplands by water erosion. *Scientific Data, 9*(1), 406. doi:10.1038/s41597-022-01489-x

Borrelli, P., Panagos, P., Ballabio, C., Lugato, E., Weynants, M., & Montanarella, L. (2014). Towards a pan-European assessment of land susceptibility to wind erosion. *Land Degradation & Development, 27*(4), 1093-1105. doi:10.1002/ldr.2318

COWI. (2018). *Increasing climate resliency of Kenya's road network, Interim Report 2.* Nairobi: The World Bank.

Deutsches Zentrum für Luft- und Raumfahrt (DLR). (2016). *TanDEM-X 30m Edited Digital Elevation Model.* Retrieved from https://download.geoservice.dlr.de/TDM30_EDEM/

FAO. (n.d.). *Chapter 2: Pollution by sediments. In Pollution from agriculture — FAO drainage and water management.* Rome: Food and Agriculture Organization of the United Nations.

Ferro, V., & Mario, M. (1995). Sediment delivery processes at basin scale. *Hydrological Sciences Journal-Journal Des Sciences Hydrologiques, 40*(6), 703-717. doi:10.1080/02626669509491460

FHWA. (2006). *HEC 14: Hydraulic design of energy dissipators for culverts and channels.* Washington, DC: U.S. Department of Transportation.

Ganasri, B. P., & Ramesh, H. (2016). Assessment of soil erosion by RUSLE model using remote sensing and GIS - A case study of Nethravathi Basin. *Geoscience Frontiers, 7*(6), 953-961. doi:10.1016/j.gsf.2015.10.007

GIBB. (2016). *Consultancy services for preliminary and detailed engineering design for Wajir-Buna-Moyale Road, Volume 1: Engineering report 1C-Hydrological and drainage study final report.* Nairobi: KeNHA.

Hairsine, P. B., & Rose, C. W. (1992). Modeling water erosion due to overland flow using physical principles: 1. Sheet flow. *Water Resources Research, 28*(1), 237-243. doi:10.1029/91WR02380

International Development Association. (2020). *Horn of Africa Gateway Development Project, Report No: PAD2535.* Nairobi: The World Bank.

Iqbal, U., & Bin Riaz, Z. M. (2024). Blockage at cross-drainage hydraulic structures – Advances, challenges and opportunities. *Heliyon, 10*(16), e35786. doi:10.1016/j.heliyon.2024.e35786

KBC Digital. (2024, April 9). *Nairobi-Garissa road closed due to flooding.* Retrieved 6 01, 2025, from KBC: https://www.kbc.co.ke/nairobi-garissa-road-closed-due-to-flooding/

Ludwig, J. A., Wilcox, B. P., Breshears, D. D., Tongway, D., & Imeson, A. (2005). Vegetation patches and runoff-erosion as interacting ecohydrological processes in semiarid landscapes. *Ecology, 86*(2), 288-297. doi:10.1890/03-0569

Malczewski, J. (2006). GIS-based multicriteria decision analysis: A survey of the literature. *International Journal of Geographical Information Science, 20*(7), 703-726. doi:10.1080/13658810600661508

McCool, D. K., Brown, L. C., Foster, G. R., Mutchler, C. K., & Meyer, L. D. (1987). Revised slope steepness factor for the Universal Soil Loss Equation. *Transactions of the ASAE, 30*(5), 1387-1396. doi:10.13031/2013.30576

Melbourne Water. (2021, September 17). *Hydrologic and hydraulic design.* Retrieved 07 01, 2025, from Melbourne Water: https://www.melbournewater.com.au/building-and-works/

Ministry of Roads and Transport. (2025). *Road design manual, Volume 2: Hydrology and drainage design, Part 1: Hydrological surveys.* Nairobi: State Department for Roads.

Mitasova, H., Hofierka, J., Zlocha, M., & Iverson, L. R. (1996). Modelling topographic potential for erosion and deposition using GIS. *International journal of geographical information systems, 10*(5), 629-641. doi:10.1080/02693799608902101

Moore, I. D., Grayson, R. B., & Ladson, A. R. (1991). Digital terrain modelling: A review of hydrological, geomorphological, and biological applications. *Hydrological Processes, 5*(1), 3-30. doi:10.1002/hyp.3360050103

Morgan, R. (2005). *Soil erosion and conservation* (3rd ed.). Carlton: Blackwell Publishing Ltd.

Muste, M., & Xu, H. (2017). *Mitigation of sedimentation at muti-box culverts, TR-665.* Iowa City: Iowa Highway Research Board.

Mutua, B. M., & Klik, A. (2004). *Soil erosion management at a large catchment scale using the RUSLE-GIS: The case of Masinga catchment, Kenya.* Vienna: WIT Press.

Niels, H. B., & Gicheru, P. (2004). *Soil data derived from SOTER for studies of carbon stocks and change in Kenya (GEF-SOC Project; version 1.0), Technical Report 2004/01.* Wageningen: ISRIC− World Soil Information.

Ontario Ministry of Natural Resources. (2019, March 4). *Environmental guidelines for access roads and water crossings.* Retrieved from ontario.ca: https://www.ontario.ca/page/environmental-guidelines-access-roads-and-water-crossings

Panagos, P., Borrelli, D. A., Meusburger, K., Alewell, C., Lugato, E., & Montanarella, L. (2014). Soil erodibility in Europe: A high-resolution dataset based on LUCAS. *Science of The Total Environment, 479-480*, 189-200. doi:10.1016/j.scitotenv.2014.02.010

Panagos, P., Borrelli, P., Meusburger, K., Yu, B., Klik, A., Lim, K. J., . . . Ballabio, C. (2017). Global rainfall erosivity assessment based on high-temporal resolution rainfall records. *Scientific Reports, 7*(1), 4175. doi:10.1038/s41598-017-04282-8

Renard, K. G., Foster, G. R., Weesies, G. A., McCool, D. K., & Yoder, D. C. (1997). *Predicting soil erosion by water: A guide to conservation planning with the revised universal soil loss equation (RUSLE).* U.S. Department of Agriculture.

USDA Forest Service. (1997). *Methods for inventory and environmental risk assessment of road drainage crossings.* Washington, DC: U.S. Department of Agriculture.

Walling, D. E. (1983). The sediment delivery problem. *Journal of Hydrology, 65*(1-3), 209-237. doi:10.1016/0022-1694(83)90217-2

Watene, G., Lijun, Y., Nie, Y., Zhang, Z., Hategekimana, Y., Mutua, F., . . . Ayugi, B. (2021). Spatial-temporal variability of future rainfall erosivity and its impact on soil loss risk in Kenya. *Applied Sciences, 11*(21), 9903. doi:10.3390/app11219903

Wilson, J. P., & Gallant, J. C. (2000). *Terrain analysis: Principles and applications.* New York: John Wiley & Sons.

Wischmeier, W. H., & Smith, D. D. (1978). *Predicting rainfall erosion losses - A guide to conservation planning.* Washington DC: US Department of Agriculture, Science and Education Administration.

Xu, H., Koylu, C., Demir, I., & Muste, M. (2019). A web-based geovisual analytics platform for identifying potential contributors to culvert sedimentation. *Science of the Total Environment, 692*(1), 806-817. doi:10.1016/j.scitotenv.2019.07.157

Zanaga, D., Van De Kerchove, R., Daems, D., De Keersmaecker, W., Brockmann, C., Kirches, G., . . . Arino, O. (2022). *ESA WorldCover 10 m 2021 v200.* doi:10.5281/zenodo.7254221

Zhao, G., Wen, Z., Wang, F., & Gao, P. (2013). Soil erosion, conservation, and eco-environment changes in the Loess plateau of China. *Land Degradation & Development, 24*(5), 499-510. doi:10.1002/ldr.2246

Appendices

Appendix 1: A14 (Wajir- Moyale) Road Drainage Catchment RUSLE Matrix

Catchment ID	Area (km2)	RUSLE (t/ha/yr)	Potential Sediment (t/yr)	SDR	Sediment Yield (t/yr)	Sediment Yield (kg/yr)	Normalised Sediment Yield (kg/yr/km2)	Bulk Density (g/cm3)	Bulk Density (kg/m3)	Sediment Volume (m3/yr)	Normalised Sediment Volume (m3/km2/yr)	RUSLE Erosion Severity	Drainage Impacts due to Sediments
1	7.5771	52.63516499	39882.19087	0.32607042 8	13004.40303	13004403.03	1716277.076	1.273	1272.50	10219.57	1348.74	Severe	High
2	53.1929	46.38528683	246736.7924	0.25557453 7	63059.64136	63059641.36	1185489.818	1.276	1276.00	49419.78	929.07	Severe	Severe
3	6.9944	1.674260226	1171.044573	0.32934834 3	385.68158 91	385681.58 91	55141.48306	1.350	1350.00	285.69	40.85	Slight	Low
4	85.1964	14.14806233	120536.3978	0.24096093 2	29044.562 78	29044562. 78	340913.029	1.315	1314.76	22091.12	259.30	High	Severe
5	2.3624	4.067128972	960.8185484	0.37720731 9	362.42778 9	362427.78 9	153415.0817	1.400	1400.00	258.88	109.58	Slight	Low
6	5.1702	28.24697539	14604.25121	0.34202737 9	4995.0537 66	4995053.7 66	966123.8959	1.400	1400.00	3567.90	690.09	Very High	Moderate
7	5.3878	18.01628335	9706.813144	0.34026937	3302.9311 95	3302931.1 95	613038.9388	1.313	1313.33	2514.92	466.78	High	Moderate
8	22.2537	11.80418985	26268.68997	0.28498631 9	7486.2172 59	7486217.2 59	336403.2615	1.400	1400.00	5347.30	240.29	High	High
9	4.8135	26.48267296	12747.43463	0.34509738 5	4399.1063 56	4399106.3 56	913910.1186	1.400	1400.00	3142.22	652.79	Very High	Moderate
10	7.4789	29.97865628	22420.73725	0.32660255 3	7322.6700 14	7322670.0 14	979110.5663	1.303	1302.50	5622.01	751.72	Very High	High
11	10.7517	56.30007707	60532.15386	0.31211500 5	18892.993 51	18892993. 51	1757209.884	1.357	1356.67	13926.04	1295.24	Severe	High

Catchment ID	Area (km2)	RUSLE (t/ha/yr)	Potential Sediment (t/yr)	SDR	Sediment Yield (t/yr)	Sediment Yield (kg/yr)	Normalised Sediment Yield (kg/yr/km2)	Bulk Density (g/cm3)	Bulk Density (kg/m3)	Sediment Volume (m3/yr)	Normalised Sediment Volume (m3/km2/yr)	RUSLE Erosion Severity	Drainage Impacts due to Sediments
12	10.3175	33.71065078	34780.96395	0.31372742 2	10911.742 15	10911742. 15	1057595.556	1.335	1335.00	8173.59	792.21	Very High	High
13	3.3854	29.56956213	10010.47956	0.36061853 2	3609.9644 49	3609964.4 49	1066333.21	1.335	1335.00	2704.09	798.75	Very High	Moderate
14	1.9542	34.79365701	6799.376453	0.38625860 2	2626.3176 43	2626317.6 43	1343934.932	1.335	1335.00	1967.28	1006.69	Very High	Moderate
15	2.0306	17.12769879	3477.950516	0.38441138 6	1336.9637 78	1336963.7 78	658408.243	1.400	1400.00	954.97	470.29	High	Low
16	1.7303	23.43202919	4054.44401	0.39217880 1	1590.0669 91	1590066.9 91	918954.5112	1.400	1400.00	1135.76	656.40	Very High	Moderate
17	33.2596	0.730976762	2431.199472	0.27102519 3	658.91630 65	658916.30 65	19811.31182	1.400	1400.00	470.65	14.15	Slight	Low
18	23.8617	28.36067409	67673.3897	0.28251181 7	19118.532 26	19118532. 26	801222.5558	1.410	1410.00	13559.24	568.24	Very High	High
19	4.618	0.504960363	233.190695 8	0.34689061 4	80.891663 69	80891.663 69	17516.60106	1.420	1420.00	56.97	12.34	Slight	Low
20	5.1121	1.017299077	520.053461 1	0.34251088 1	178.12396 91	178123.96 91	34843.6003	1.363	1362.50	130.73	25.57	Slight	Low
21	30.5377	25.73696923	78594.7845 2	0.27393325	21529.724 75	21529724. 75	705021.1622	1.430	1429.60	15059.96	493.16	Very High	Severe
22	58.872	3.353235325	19741.167	0.25235429	4981.7681 78	4981768.1 78	84620.33188	1.372	1372.00	3631.03	61.68	Slight	Moderate
23	10.8347	44.22408608	47915.4705 4	0.31181512 6	14940.768 49	14940768. 49	1378973.898	1.420	1420.00	10521.67	971.11	Severe	High
24	6.0264	0.661331052	398.544545 1	0.33553825 8	133.72694 26	133726.94 26	22190.18694	1.480	1480.00	90.36	14.99	Slight	Low

Catchment ID	Area (km2)	RUSLE (t/ha/yr)	Potential Sediment (t/yr)	SDR	Sediment Yield (t/yr)	Sediment Yield (kg/yr)	Normalised Sediment Yield (kg/yr/km2)	Bulk Density (g/cm3)	Bulk Density (kg/m3)	Sediment Volume (m3/yr)	Normalised Sediment Volume (m3/km2/yr)	RUSLE Erosion Severity	Drainage Impacts due to Sediments
25	2.8956	0.412395951	119.4133717	0.36773246 2	43.91217318	43912.17318	15165.13786	1.430	1430.00	30.71	10.60	Slight	Low
26	12.5492	0.385476091	483.7416567	0.30614155 6	148.09342 35	148093.42 35	11801.02505	1.420	1420.00	104.29	8.31	Slight	Low
27	3.4513	0.228387958	78.8235361 1	0.35975053 7	28.356809 48	28356.809 48	8216.269082	1.407	1406.99	20.15	5.84	Slight	Low
28	2.638	0.186890565	49.3017311 1	0.37204026 2	18.342228 96	18342.228 96	6953.081486	1.300	1300.00	14.11	5.35	Slight	Low
29	172.8627	0.391126041	6761.11034 6	0.22056501 6	1491.2644 09	1491264.4 09	8626.872129	1.400	1400.00	1065.19	6.16	Slight	Moderate
30	8.5196	0.335206316	285.582372 7	0.32132675 6	91.765257 43	91765.257 43	10771.07581	1.410	1410.00	65.08	7.64	Slight	Low
31	3697.2078	21.22444398	7847117.98 5	0.15040596 4	1180253.3 46	118025334 6	319228.296	1.448	1448.00	815092.09	220.46	Very High	Severe
32	6.8147	0.128618176	87.6494283 9	0.33042161 4	28.961265 55	28961.265 55	4249.822524	1.460	1460.00	19.84	2.91	Slight	Low
33	3.7012	0.12542598	46.4226637 8	0.35662063 7	16.555279 92	16555.279 92	4472.949292	1.386	1386.47	11.94	3.23	Slight	Low
34	4.0542	0.117667816	47.7048860 6	0.35258281 8	16.819923 15	16819.923 15	4148.765021	1.398	1397.78	12.03	2.97	Slight	Low
35	27.8193	0.174872031	486.481749 9	0.27714434 1	134.82566 41	134825.66 41	4846.479391	1.480	1480.00	91.10	3.27	Slight	Low
36	4.451	0.234832769	104.524065 5	0.34849142 1	36.425740 1	36425.740 1	8183.720535	1.480	1480.00	24.61	5.53	Slight	Low
37	723.0915	9.038429229	653561.134 9	0.18443788 5	120541.43 34	120541433 .4	166702.877	1.402	1401.67	85998.64	118.93	Moderate	Severe

Catchment ID	Area (km2)	RUSLE (t/ha/yr)	Potential Sediment (t/yr)	SDR	Sediment Yield (t/yr)	Sediment Yield (kg/yr)	Normalised Sediment Yield (kg/yr/km2)	Bulk Density (g/cm3)	Bulk Density (kg/m3)	Sediment Volume (m3/yr)	Normalised Sediment Volume (m3/km2/yr)	RUSLE Erosion Severity	Drainage Impacts due to Sediments
38	38.5233	1.458859119	5620.006748	0.26609324 8	1495.445851	1495445.851	38819.25616	1.480	1480.00	1010.44	26.23	Slight	Moderate
39	2.7025	0.477082588	128.9315694	0.37091857 1	47.82311344	47823.11344	17695.87916	1.323	1322.61	36.16	13.38	Slight	Low
40	1.4977	0.276792149	41.45516009	0.39932011 4	16.55387926	16553.87926	11052.86724	1.480	1480.00	11.19	7.47	Slight	Low
41	17.6811	4.23267785	7483.840033	0.29329903 2	2195.003041	2195003.041	124144.0318	1.480	1480.00	1483.11	83.88	Slight	Moderate
42	3.1763	0.264422064	83.98838023	0.36350392 2	30.53010562	30530.10562	9611.845739	1.444	1444.00	21.14	6.66	Slight	Low
43	40.8369	9.241430145	37739.13587	0.26416038 8	9969.184791	9969184.791	244121.9777	1.480	1480.00	6735.94	164.95	Moderate	High
44	8.5239	0.32229927	274.724675	0.32130648 9	88.2708209	88270.8209	10355.68471	1.480	1480.00	59.64	7.00	Slight	Low
45	3.8328	0.269056979	103.1241591	0.35506655 8	36.61594025	36615.94025	9553.313569	1.421	1420.98	25.77	6.72	Slight	Low
46	29.7963	0.990318396	2950.782403	0.27477612 7	810.804561	810804.561	27211.58536	1.306	1305.83	620.91	20.84	Slight	Low
47	3.2435	0.546843309	177.3686272	0.36255387 6	64.30568328	64305.68328	19826.01612	1.480	1480.00	43.45	13.40	Slight	Low
48	4.5636	0.320848131	146.4222529	0.34740482 3	50.8677969	50867.7969	11146.41881	1.400	1400.00	36.33	7.96	Slight	Low
49	86.4375	2.500560052	21614.21595	0.24052571 6	5198.774763	5198774.763	60144.89964	1.480	1480.00	3512.69	40.64	Slight	Moderate
50	50.8196	3.343683211	16992.46433	0.25703684 7	4367.689453	4367689.453	85944.97897	1.412	1411.96	3093.35	60.87	Slight	Moderate

Catchment ID	Area (km2)	RUSLE (t/ha/yr)	Potential Sediment (t/yr)	SDR	Sediment Yield (t/yr)	Sediment Yield (kg/yr)	Normalised Sediment Yield (kg/yr/km2)	Bulk Density (g/cm3)	Bulk Density (kg/m3)	Sediment Volume (m3/yr)	Normalised Sediment Volume (m3/km2/yr)	RUSLE Erosion Severity	Drainage Impacts due to Sediments
51	2.3371	0.230260203	53.81411213	0.37771534 5	20.32641591	20326.41591	8697.281209	1.416	1416.25	14.35	6.14	Slight	Low
52	3.9423	0.244365679	96.33628166	0.35381853 6	34.08556218	34085.56218	8646.110691	1.480	1480.00	23.03	5.84	Slight	Low
53	21.7917	2.566501393	5592.84284	0.28573464 5	1598.068964	1598068.964	73333.83646	1.482	1481.79	1078.47	49.49	Slight	Moderate
54	2.896	0.296943828	85.99493264	0.36772611 3	31.62258229	31622.58229	10919.39996	1.550	1550.00	20.40	7.04	Slight	Low
55	104.7789	0.733314044	7683.583891	0.23480917 4	1804.175988	1804175.988	17218.88651	1.550	1550.00	1163.98	11.11	Slight	Moderate
56	67.9773	0.519601289	3532.10927	0.24785849 1	875.4632743	875463.2743	12878.75915	1.427	1426.98	613.51	9.03	Slight	Low
57	2.8063	0.29800285	83.62853979	0.36917520 8	30.87358358	30873.58358	11001.52642	1.417	1417.18	21.79	7.76	Slight	Low
58	81.6761	0.483023271	3945.145701	0.24223529 2	955.6535192	955653.5192	11700.5283	1.543	1543.33	619.21	7.58	Slight	Low
59	3.1543	0.290435595	91.6120997	0.36381987 1	33.33030232	33330.30232	10566.62408	1.550	1550.00	21.50	6.82	Slight	Low
60	6.2731	0.247103303	155.010373	0.33385971 2	51.75171845	51751.71845	8249.783752	1.550	1550.00	33.39	5.32	Slight	Low
61	753.3669	3.232097878	243495.5559	0.18349467 8	44680.1387	44680138.7	59307.27605	1.550	1550.00	28825.90	38.26	Slight	Severe
62	914.1079	3.971195581	363010.1253	0.17911196 9	65019.45823	65019458.23	71128.86589	1.417	1416.67	45896.09	50.21	Slight	Severe
63	0.0007	0.68942973	0.048260081	1.04138672 1	0.05025740 8	50.25740759	71796.29655	1.465	1465.38	0.03	48.99	Slight	Low

Catchment ID	Area (km2)	RUSLE (t/ha/yr)	Potential Sediment (t/yr)	SDR	Sediment Yield (t/yr)	Sediment Yield (kg/yr)	Normalised Sediment Yield (kg/yr/km2)	Bulk Density (g/cm3)	Bulk Density (kg/m3)	Sediment Volume (m3/yr)	Normalised Sediment Volume (m3/km2/yr)	RUSLE Erosion Severity	Drainage Impacts due to Sediments
64	64.4906	0.280612169	1809.684716	0.24949522 5	451.5076953	451507.6953	7001.139628	1.528	1527.78	295.53	4.58	Slight	Low
65	4.0258	0.228958456	92.17409533	0.35289277 4	32.52757222	32527.57222	8079.778483	1.510	1510.00	21.54	5.35	Slight	Low
66	0.3593	0.146671994	5.269924749	0.47732825	2.515483958	2515.483958	7001.068629	1.545	1545.35	1.63	4.53	Slight	Low
67	4.2536	0.211378844	89.91210529	0.35047311 6	31.51177568	31511.77568	7408.260223	1.550	1550.00	20.33	4.78	Slight	Low
68	2.334	0.175099832	40.86830086	0.37777801 8	15.4391457	15439.1457	6614.886762	1.548	1547.79	9.97	4.27	Slight	Low
69	4.2052	0.269455435	113.3113993	0.35097481 9	39.76944784	39769.44784	9457.207229	1.550	1550.00	25.66	6.10	Slight	Low
70	55.6038	0.400416922	2226.470245	0.25416235 8	565.8849279	565884.9279	10177.09092	1.550	1550.00	365.09	6.57	Slight	Low
71	53.5193	0.351500535	1881.206258	0.25537918	480.4209106	480420.9106	8976.591821	1.550	1550.00	309.95	5.79	Slight	Low
72	8.5074	0.185512321	157.8227518	0.32138432	50.72175773	50721.75773	5962.075103	1.550	1550.00	32.72	3.85	Slight	Low
73	88.9049	0.289607658	2574.753991	0.23968098 4	617.119569	617119.569	6941.344841	1.550	1550.00	398.14	4.48	Slight	Low
74	2683.2239	1.430556237	383850.2686	0.15655508 4	60093.71113	60093711.13	22396.08522	1.550	1550.00	38770.14	14.45	Slight	Severe
75	444.5178	0.323588104	14384.0672	0.19600319 3	2819.323096	2819323.096	6342.430149	1.550	1550.00	1818.92	4.09	Slight	Moderate
76	5.5308	0.228437132	126.3440089	0.33915700 9	42.85045612	42850.45612	7747.605432	1.545	1545.35	27.73	5.01	Slight	Low
77	1.9321	0.200654511	38.76845805	0.38680812 7	14.99595465	14995.95465	7761.479555	1.514	1513.64	9.91	5.13	Slight	Low

Catchment ID	Area (km2)	RUSLE (t/ha/yr)	Potential Sediment (t/yr)	SDR	Sediment Yield (t/yr)	Sediment Yield (kg/yr)	Normalised Sediment Yield (kg/yr/km2)	Bulk Density (g/cm3)	Bulk Density (kg/m3)	Sediment Volume (m3/yr)	Normalised Sediment Volume (m3/km2/yr)	RUSLE Erosion Severity	Drainage Impacts due to Sediments
78	10.8105	0.18898358	204.3006992	0.31190229 3	63.72185656	63721.856 56	5894.441197	1.550	1550.00	41.11	3.80	Slight	Low
79	55.2463	0.22766 4132	1257.760092	0.254 36736 5	319.933120 2	319933.12 02	5791.032525	1.550	1550.00	206.41	3.74	Slight	Low
80	26.8345	0.19236 1309	516.1919542	0.278 39575 1	143.70564 65	143705.64 65	5355.257096	1.550	1550.00	92.71	3.46	Slight	Low
81	1.9583	0.33224 1054	65.0627656 5	0.386 15742 3	25.124469 91	25124.469 91	12829.73493	1.550	1550.00	16.21	8.28	Slight	Low
82	335.3 077	0.36119 7192	12111.2199 9	0.203 03403 7	2458.9898 84	2458989.8 84	7333.532408	1.550	1550.00	1586.45	4.73	Slight	Moderate
83	175.5 653	0.29687 8939	5212.16400 5	0.220 13771 5	1147.3938 76	1147393.8 76	6535.425146	1.550	1550.00	740.25	4.22	Slight	Low
84	21.30 16	0.51652 5798	1100.28259 5	0.286 54825 1	315.28405 32	315284.05 32	14800.95642	1.550	1550.00	203.41	9.55	Slight	Low
85	3.234 2	0.54674 348	176.827776 4	0.362 68402 9	64.132610 35	64132.610 35	19829.51281	1.550	1550.00	41.38	12.79	Slight	Low
86	1.987 6	0.40196 6902	79.8949414 4	0.385 44122 9	30.794804 38	30794.804 38	15493.46165	1.550	1550.00	19.87	10.00	Slight	Low
87	4.560 2	0.44258 8519	201.829216 4	0.347 43719	70.122975 83	70122.975 83	15377.17114	1.550	1550.00	45.24	9.92	Slight	Low

Appendix 2: A14 (Wajir- Moyale) Road Drainage Crossing SPI Matrix

Drainage Crossing ID	Drainage Crossing Coordinates (EPSG32637)		SPI Value	Ln (SPI) Range	Gully Erosion Susceptibility
	Easting (X)	Northing (Y)			
1	511200.5573	382744.0214	7.849	5 to 10	High
2	513401.2830	380265.3044	9.102	5 to 10	High
3	517054.7127	377321.792	9.791	5 to 10	High
4	517869.7795	375103.6657	10.508	>10	Severe
5	519193.9918	372750.8248	9.708	5 to 10	High
6	519521.1132	372190.2362	9.194	5 to 10	High
7	522274.4703	369694.6279	7.227	5 to 10	High
8	523662.2070	368406.6447	9.088	5 to 10	High
9	523744.9742	360579.3297	7.996	5 to 10	High
10	525608.4367	354408.7546	8.423	5 to 10	High
11	527030.9917	349755.1041	4.343	0 to 5	Moderate
12	527974.7048	348080.9371	8.760	5 to 10	High
13	527995.7658	347991.1349	7.833	5 to 10	High
14	528068.4360	345724.0511	5.133	5 to 10	High
15	529762.6044	340742.4362	5.651	5 to 10	High
16	529847.2236	340499.1615	7.089	5 to 10	High
17	531223.4579	337804.4374	8.418	5 to 10	High
18	531002.1505	338194.1847	8.298	5 to 10	High
19	532042.7131	336384.9863	6.562	5 to 10	High
20	533944.9388	332571.1975	7.006	5 to 10	High
21	534807.7126	330882.5368	9.281	5 to 10	High
22	540179.0399	326105.7922	9.545	5 to 10	High
23	539466.9667	326318.4288	6.239	5 to 10	High
24	539961.4694	326145.6966	6.474	5 to 10	High
25	541713.8186	325131.1206	6.958	5 to 10	High
26	547418.1917	320719.331	6.717	5 to 10	High
27	547602.9156	320653.8307	6.047	5 to 10	High
28	548808.7323	319372.1671	5.547	5 to 10	High
29	550376.0765	317090.4228	9.430	5 to 10	High
30	551362.3459	315609.5143	10.458	>10	Severe
31	556286.1358	308095.3601	14.051	>10	Severe
32	557185.5347	306936.7049	6.723	5 to 10	High
33	557955.7975	306669.4078	7.932	5 to 10	High
34	558731.0353	306061.1297	7.020	5 to 10	High
35	559852.8749	304333.3257	9.353	5 to 10	High
36	560971.1464	300820.9011	8.758	5 to 10	High
37	561899.8138	296006.3584	11.714	>10	Severe
38	562954.1161	294415.4295	9.085	5 to 10	High
39	563875.8334	291141.1859	6.026	5 to 10	High
40	563975.1948	290796.9524	-2.092	-6 to 0	Low
41	564021.7024	290739.4865	7.577	5 to 10	High
42	564457.2331	288593.2151	4.636	0 to 5	Moderate
43	565104.2910	286920.3975	7.189	5 to 10	High
44	565488.4852	285992.2717	-6.908	-6 to 0	Low
45	565356.3034	283407.3303	6.879	5 to 10	High
46	565381.6016	283225.6953	8.702	5 to 10	High
47	566434.2443	280751.7388	4.655	0 to 5	Moderate
48	566640.5550	280514.0749	5.691	5 to 10	High
49	567226.3663	279827.7619	11.008	>10	Severe
50	567457.6183	279408.1254	9.121	5 to 10	High
51	567753.0724	278444.1065	6.706	5 to 10	High
52	567838.9059	277647.0246	5.543	5 to 10	High

Drainage Crossing ID	Drainage Crossing Coordinates (EPSG32637)		SPI Value	Ln (SPI) Range	Gully Erosion Susceptibility
	Easting (X)	Northing (Y)			
53	569105.7643	274735.3377	8.952	5 to 10	High
54	569228.8395	274592.2139	6.493	5 to 10	High
55	573085.0884	259775.2303	10.975	>10	Severe
56	574342.5109	258823.2227	9.096	5 to 10	High
57	574532.8491	258733.7857	7.053	5 to 10	High
58	580652.5223	253003.9176	10.473	>10	Severe
59	582618.8016	248806.4988	5.713	5 to 10	High
60	586951.9781	243562.1198	6.039	5 to 10	High
61	587634.1872	241747.7544	11.976	>10	Severe
62	588715.2647	238700.2606	11.901	>10	Severe
63	589785.2416	232733.185	-6.908	-6 to 0	Low
64	589437.8708	229062.8579	9.381	5 to 10	High
65	588600.0161	226016.7242	6.001	5 to 10	High
66	589803.9717	221076.0762	6.650	5 to 10	High
67	589112.3225	222560.4769	6.809	5 to 10	High
68	589661.6792	220302.4066	4.885	0 to 5	Moderate
69	589630.2827	215292.0865	5.270	5 to 10	High
70	589659.8164	213615.8254	9.518	5 to 10	High
71	590490.6681	212067.7522	9.098	5 to 10	High
72	591360.6102	209522.3637	8.093	5 to 10	High
73	593604.4039	207208.4344	9.903	5 to 10	High
74	597151.8208	203367.1353	12.368	>10	Severe
75	598558.1099	201960.2046	9.878	5 to 10	High
76	599957.1421	200039.2522	7.215	5 to 10	High
77	602047.1466	198886.4447	4.135	0 to 5	Moderate
78	601154.6602	199294.9338	6.360	5 to 10	High
79	604255.2595	197370.1393	-6.908	-6 to 0	Low
80	606056.0184	196262.2108	7.323	5 to 10	High
81	608025.7989	195081.1408	4.463	0 to 5	Moderate
82	609794.8432	194777.0935	10.291	>10	Severe
83	611073.3391	194571.2762	11.004	>10	Severe
84	611596.5659	194487.3754	8.130	5 to 10	High
85	614000.0196	194114.7374	7.188	5 to 10	High
86	615041.9864	193936.1065	6.461	5 to 10	High
87	616375.9871	193742.0625	7.299	5 to 10	High

Appendix 3: A14 (Wajir- Moyale) Road Drainage MCMDA Matrix

Drainage Crossing	Drainage Crossing Coordinates (EPSG32637)		RUSLE Erosion Severity	Sediment Yield Drainage Impacts	SPI erosion	RUSLE Score	Sediment Yield Score	SPI Score	Composite Score	Hydrodynamic Impact Level	Expected Impacts	Possible Mitigation
	Easting (X)	Northing (Y)										
1	511200.5573	382744.0214	Severe	High	High	5	3	3	3.6	High	Substantial sediment accumulation; possible blockage and flooding	Energy dissipators, sediment traps, upsized drainage structures and frequent monitoring
2	513401.2830	380265.3044	Severe	Severe	High	5	5	3	4.2	Severe	Blockage or overtopping likely; risk of culvert washout and severe downstream impact	Energy dissipators, upsized drainage structures, robust sediment control, upstream erosion control, frequent monitoring
3	517054.7127	377321.792	Slight	Low	High	1	1	3	1.8	Low	Minimal restriction or sedimentation; low risk of failure	Routine inspection and debris removal
4	517869.7795	375103.6657	High	Severe	Severe	3	5	5	4.4	Severe	Blockage or overtopping likely; risk of culvert washout and severe downstream impact	Energy dissipators, upsized drainage structures, robust sediment control, upstream erosion control, frequent monitoring
5	519193.9918	372750.8248	Slight	Low	High	1	1	3	1.8	Low	Minimal restriction or sedimentation; low risk of failure	Routine inspection and debris removal
6	519521.1132	372190.2362	Very High	Moderate	High	4	2	3	3	Moderate	Partial flow restriction, minor scour, and local sediment buildup	Regular maintenance, sediment traps/check dams
7	522274.4703	369694.6279	High	Moderate	High	3	2	3	2.7	Moderate	Partial flow restriction, minor scour, and local sediment buildup	Regular maintenance, sediment traps/check dams
8	523662.2070	368406.6447	High	High	High	3	3	3	3	Moderate	Partial flow restriction, minor scour, and local sediment buildup	Regular maintenance, sediment traps/check dams
9	523744.9742	360579.3297	Very High	Moderate	High	4	2	3	3	Moderate	Partial flow restriction, minor scour, and local sediment buildup	Regular maintenance, sediment traps/check dams
10	525608.4367	354408.7546	Very High	High	High	4	3	3	3.3	High	Substantial sediment accumulation; possible blockage and flooding	Energy dissipators, sediment traps, upsized drainage structures and frequent monitoring
11	527030.9917	349755.1041	Severe	High	Moderate	5	3	2	3.2	High	Substantial sediment accumulation; possible blockage and flooding	Energy dissipators, sediment traps, upsized drainage structures and frequent monitoring
12	527974.7048	348080.9371	Very High	High	High	4	3	3	3.3	High	Substantial sediment accumulation; possible blockage and flooding	Energy dissipators, sediment traps, upsized drainage structures and frequent monitoring
13	527995.7658	347991.1349	Very High	Moderate	High	4	2	3	3	Moderate	Partial flow restriction, minor scour, and local sediment buildup	Regular maintenance, sediment traps/check dams
14	528068.4360	345724.0511	Very High	Moderate	High	4	2	3	3	Moderate	Partial flow restriction, minor scour, and local sediment buildup	Regular maintenance, sediment traps/check dams
15	529762.6044	340742.4362	High	Low	High	3	1	3	2.4	Moderate	Partial flow restriction, minor scour, and local sediment buildup	Regular maintenance, sediment traps/check dams
16	529847.2236	340499.1615	Very High	Moderate	High	4	2	3	3	Moderate	Partial flow restriction, minor scour, and local sediment buildup	Regular maintenance, sediment traps/check dams
17	531223.4579	337804.4374	Slight	Low	High	1	1	3	1.8	Low	Minimal restriction or sedimentation; low risk of failure	Routine inspection and debris removal
18	531002.1505	338194.1847	Very High	High	High	4	3	3	3.3	High	Substantial sediment accumulation; possible blockage and flooding	Energy dissipators, sediment traps, upsized drainage structures and frequent monitoring
19	532042.7131	336384.9863	Slight	Low	High	1	1	3	1.8	Low	Minimal restriction or sedimentation; low risk of failure	Routine inspection and debris removal

Drainage Crossing	Drainage Crossing Coordinates (EPSG32637)		RUSLE Erosion Severity	Sediment Yield Drainage Impacts	SPI erosion	RUSLE Score	Sediment Yield Score	SPI Score	Composite Score	Hydrodynamic Impact Level	Expected Impacts	Possible Mitigation
	Easting (X)	Northing (Y)										
20	533944.9388	332571.1975	Slight	Low	High	1	1	3	1.8	Low	Minimal restriction or sedimentation; low risk of failure	Routine inspection and debris removal
21	534807.7126	330882.5368	Very High	Severe	High	4	5	3	3.9	High	Substantial sediment accumulation; possible blockage and flooding	Energy dissipators, sediment traps, upsized drainage structures and frequent monitoring
22	540179.0399	326105.7922	Slight	Moderate	High	1	2	3	2.1	Moderate	Partial flow restriction, minor scour, and local sediment buildup	Regular maintenance, sediment traps/check dams
23	539466.9667	326318.4288	Severe	High	High	5	3	3	3.6	High	Substantial sediment accumulation; possible blockage and flooding	Energy dissipators, sediment traps, upsized drainage structures and frequent monitoring
24	539961.4694	326145.6966	Slight	Low	High	1	1	3	1.8	Low	Minimal restriction or sedimentation; low risk of failure	Routine inspection and debris removal
25	541713.8186	325131.1206	Slight	Low	High	1	1	3	1.8	Low	Minimal restriction or sedimentation; low risk of failure	Routine inspection and debris removal
26	547418.1917	320719.331	Slight	Low	High	1	1	3	1.8	Low	Minimal restriction or sedimentation; low risk of failure	Routine inspection and debris removal
27	547602.9156	320653.8307	Slight	Low	High	1	1	3	1.8	Low	Minimal restriction or sedimentation; low risk of failure	Routine inspection and debris removal
28	548808.7323	319372.1671	Slight	Low	High	1	1	3	1.8	Low	Minimal restriction or sedimentation; low risk of failure	Routine inspection and debris removal
29	550376.0765	317090.4228	Slight	Moderate	High	1	2	3	2.1	Moderate	Partial flow restriction, minor scour, and local sediment buildup	Regular maintenance, sediment traps/check dams
30	551362.3459	315609.5143	Slight	Low	Severe	1	1	5	2.6	Moderate	Partial flow restriction, minor scour, and local sediment buildup	Regular maintenance, sediment traps/check dams
31	556286.1358	308095.3601	Very High	Severe	Severe	4	5	5	4.7	Severe	Blockage or overtopping likely; risk of culvert washout and severe downstream impact	Energy dissipators, upsized drainage structures, robust sediment control, upstream erosion control, frequent monitoring
32	557185.5347	306936.7049	Slight	Low	High	1	1	3	1.8	Low	Minimal restriction or sedimentation; low risk of failure	Routine inspection and debris removal
33	557955.7975	306669.4078	Slight	Low	High	1	1	3	1.8	Low	Minimal restriction or sedimentation; low risk of failure	Routine inspection and debris removal
34	558731.0353	306061.1297	Slight	Low	High	1	1	3	1.8	Low	Minimal restriction or sedimentation; low risk of failure	Routine inspection and debris removal
35	559852.8749	304333.3257	Slight	Low	High	1	1	3	1.8	Low	Minimal restriction or sedimentation; low risk of failure	Routine inspection and debris removal
36	560971.1464	300820.9011	Slight	Low	High	1	1	3	1.8	Low	Minimal restriction or sedimentation; low risk of failure	Routine inspection and debris removal
37	561899.8138	296006.3584	Moderate	Severe	Severe	2	5	5	4.1	Severe	Blockage or overtopping likely; risk of culvert washout and severe downstream impact	Energy dissipators, upsized drainage structures, robust sediment control, upstream erosion control, frequent monitoring
38	562954.1161	294415.4295	Slight	Moderate	High	1	2	3	2.1	Moderate	Partial flow restriction, minor scour, and local sediment buildup	Regular maintenance, sediment traps/check dams
39	563875.8334	291141.1859	Slight	Low	High	1	1	3	1.8	Low	Minimal restriction or sedimentation; low risk of failure	Routine inspection and debris removal

Drainage Crossing	Drainage Crossing Coordinates (EPSG32637)		RUSLE Erosion Severity	Sediment Yield Drainage Impacts	SPI erosion	RUSLE Score	Sediment Yield Score	SPI Score	Composite Score	Hydrodynamic Impact Level	Expected Impacts	Possible Mitigation
	Easting (X)	Northing (Y)										
40	563975.1948	290796.9524	Slight	Low	Low	1	1	1	1	Low	Minimal restriction or sedimentation; low risk of failure	Routine inspection and debris removal
41	564021.7024	290739.4865	Slight	Moderate	High	1	2	3	2.1	Moderate	Partial flow restriction, minor scour, and local sediment buildup	Regular maintenance, sediment traps/check dams
42	564457.2331	288593.2151	Slight	Low	Moderate	1	1	2	1.4	Low	Minimal restriction or sedimentation; low risk of failure	Routine inspection and debris removal
43	565104.2910	286920.3975	Moderate	High	High	2	3	3	2.7	Moderate	Partial flow restriction, minor scour, and local sediment buildup	Regular maintenance, sediment traps/check dams
44	565488.4852	285992.2717	Slight	Low	Low	1	1	1	1	Low	Minimal restriction or sedimentation; low risk of failure	Routine inspection and debris removal
45	565356.3034	283407.3303	Slight	Low	High	1	1	3	1.8	Low	Minimal restriction or sedimentation; low risk of failure	Routine inspection and debris removal
46	565381.6016	283225.6953	Slight	Low	High	1	1	3	1.8	Low	Minimal restriction or sedimentation; low risk of failure	Routine inspection and debris removal
47	566434.2443	280751.7388	Slight	Low	Moderate	1	1	2	1.4	Low	Minimal restriction or sedimentation; low risk of failure	Routine inspection and debris removal
48	566640.5550	280514.0749	Slight	Low	High	1	1	3	1.8	Low	Minimal restriction or sedimentation; low risk of failure	Routine inspection and debris removal
49	567226.3663	279827.7619	Slight	Moderate	Severe	1	2	5	2.9	Moderate	Partial flow restriction, minor scour, and local sediment buildup	Regular maintenance, sediment traps/check dams
50	567457.6183	279408.1254	Slight	Moderate	High	1	2	3	2.1	Moderate	Partial flow restriction, minor scour, and local sediment buildup	Regular maintenance, sediment traps/check dams
51	567753.0724	278444.1065	Slight	Low	High	1	1	3	1.8	Low	Minimal restriction or sedimentation; low risk of failure	Routine inspection and debris removal
52	567838.9059	277647.0246	Slight	Low	High	1	1	3	1.8	Low	Minimal restriction or sedimentation; low risk of failure	Routine inspection and debris removal
53	569105.7643	274735.3377	Slight	Moderate	High	1	2	3	2.1	Moderate	Partial flow restriction, minor scour, and local sediment buildup	Regular maintenance, sediment traps/check dams
54	569228.8395	274592.2139	Slight	Low	High	1	1	3	1.8	Low	Minimal restriction or sedimentation; low risk of failure	Routine inspection and debris removal
55	573085.0884	259775.2303	Slight	Moderate	Severe	1	2	5	2.9	Moderate	Partial flow restriction, minor scour, and local sediment buildup	Regular maintenance, sediment traps/check dams
56	574342.5109	258823.2227	Slight	Low	High	1	1	3	1.8	Low	Minimal restriction or sedimentation; low risk of failure	Routine inspection and debris removal
57	574532.8491	258733.7857	Slight	Low	High	1	1	3	1.8	Low	Minimal restriction or sedimentation; low risk of failure	Routine inspection and debris removal
58	580652.5223	253003.9176	Slight	Low	Severe	1	1	5	2.6	Moderate	Partial flow restriction, minor scour, and local sediment buildup	Regular maintenance, sediment traps/check dams
59	582618.8016	248806.4988	Slight	Low	High	1	1	3	1.8	Low	Minimal restriction or sedimentation; low risk of failure	Routine inspection and debris removal
60	586951.9781	243562.1198	Slight	Low	High	1	1	3	1.8	Low	Minimal restriction or sedimentation; low risk of failure	Routine inspection and debris removal

Drainage Crossing	Drainage Crossing Coordinates (EPSG32637)		RUSLE Erosion Severity	Sediment Yield Drainage Impacts	SPI erosion	RUSLE Score	Sediment Yield Score	SPI Score	Composite Score	Hydrodynamic Impact Level	Expected Impacts	Possible Mitigation
	Easting (X)	Northing (Y)										
61	587634.1872	241747.7544	Slight	Severe	Severe	1	5	5	3.8	High	Substantial sediment accumulation; possible blockage and flooding	Energy dissipators, sediment traps, upsized drainage structures and frequent monitoring
62	588715.2647	238700.2606	Slight	Severe	Severe	1	5	5	3.8	High	Substantial sediment accumulation; possible blockage and flooding	Energy dissipators, sediment traps, upsized drainage structures and frequent monitoring
63	589785.2416	232733.185	Slight	Low	Low	1	1	1	1	Low	Minimal restriction or sedimentation; low risk of failure	Routine inspection and debris removal
64	589437.8708	229062.8579	Slight	Low	High	1	1	3	1.8	Low	Minimal restriction or sedimentation; low risk of failure	Routine inspection and debris removal
65	588600.0161	226016.7242	Slight	Low	High	1	1	3	1.8	Low	Minimal restriction or sedimentation; low risk of failure	Routine inspection and debris removal
66	589803.9717	221076.0762	Slight	Low	High	1	1	3	1.8	Low	Minimal restriction or sedimentation; low risk of failure	Routine inspection and debris removal
67	589112.3225	222560.4769	Slight	Low	High	1	1	3	1.8	Low	Minimal restriction or sedimentation; low risk of failure	Routine inspection and debris removal
68	589661.6792	220302.4066	Slight	Low	Moderate	1	1	2	1.4	Low	Minimal restriction or sedimentation; low risk of failure	Routine inspection and debris removal
69	589630.2827	215292.0865	Slight	Low	High	1	1	3	1.8	Low	Minimal restriction or sedimentation; low risk of failure	Routine inspection and debris removal
70	589659.8164	213615.8254	Slight	Low	High	1	1	3	1.8	Low	Minimal restriction or sedimentation; low risk of failure	Routine inspection and debris removal
71	590490.6681	212067.7522	Slight	Low	High	1	1	3	1.8	Low	Minimal restriction or sedimentation; low risk of failure	Routine inspection and debris removal
72	591360.6102	209522.3637	Slight	Low	High	1	1	3	1.8	Low	Minimal restriction or sedimentation; low risk of failure	Routine inspection and debris removal
73	593604.4039	207208.4344	Slight	Low	High	1	1	3	1.8	Low	Minimal restriction or sedimentation; low risk of failure	Routine inspection and debris removal
74	597151.8208	203367.1353	Slight	Severe	Severe	1	5	5	3.8	High	Substantial sediment accumulation; possible blockage and flooding	Energy dissipators, sediment traps, upsized drainage structures and frequent monitoring
75	598558.1099	201960.2046	Slight	Moderate	High	1	2	3	2.1	Moderate	Partial flow restriction, minor scour, and local sediment buildup	Regular maintenance, sediment traps/check dams
76	599957.1421	200039.2522	Slight	Low	High	1	1	3	1.8	Low	Minimal restriction or sedimentation; low risk of failure	Routine inspection and debris removal
77	602047.1466	198886.4447	Slight	Low	Moderate	1	1	2	1.4	Low	Minimal restriction or sedimentation; low risk of failure	Routine inspection and debris removal
78	601154.6602	199294.9338	Slight	Low	High	1	1	3	1.8	Low	Minimal restriction or sedimentation; low risk of failure	Routine inspection and debris removal
79	604255.2595	197370.1393	Slight	Low	Low	1	1	1	1	Low	Minimal restriction or sedimentation; low risk of failure	Routine inspection and debris removal
80	606056.0184	196262.2108	Slight	Low	High	1	1	3	1.8	Low	Minimal restriction or sedimentation; low risk of failure	Routine inspection and debris removal
81	608025.7989	195081.1408	Slight	Low	Moderate	1	1	2	1.4	Low	Minimal restriction or sedimentation; low risk of failure	Routine inspection and debris removal

Drainage Crossing	Drainage Crossing Coordinates (EPSG32637)		RUSLE Erosion Severity	Sediment Yield Drainage Impacts	SPI erosion	RUSLE Score	Sediment Yield Score	SPI Score	Composite Score	Hydrodynamic Impact Level	Expected Impacts	Possible Mitigation
	Easting (X)	Northing (Y)										
82	609794.8432	194777.0935	Slight	Moderate	Severe	1	2	5	2.9	Moderate	Partial flow restriction, minor scour, and local sediment buildup	Regular maintenance, sediment traps/check dams
83	611073.3391	194571.2762	Slight	Low	Severe	1	1	5	2.6	Moderate	Partial flow restriction, minor scour, and local sediment buildup	Regular maintenance, sediment traps/check dams
84	611596.5659	194487.3754	Slight	Low	High	1	1	3	1.8	Low	Minimal restriction or sedimentation; low risk of failure	Routine inspection and debris removal
85	614000.0196	194114.7374	Slight	Low	High	1	1	3	1.8	Low	Minimal restriction or sedimentation; low risk of failure	Routine inspection and debris removal
86	615041.9864	193936.1065	Slight	Low	High	1	1	3	1.8	Low	Minimal restriction or sedimentation; low risk of failure	Routine inspection and debris removal
87	616375.9871	193742.0625	Slight	Low	High	1	1	3	1.8	Low	Minimal restriction or sedimentation; low risk of failure	Routine inspection and debris removal

Editorial Committee

INSTRUCTIONS TO CONTRIBUTORS

The editorial staff of the AJERI requests contributors of articles for publication to observe the following editorial policy and guidelines accessible at https://www.iekenya.org/ in order to improve communication and to facilitate the editorial process.

Criteria for Article Selection

Priority in the selection of articles for publication is that the articles:

a. Are written in the English language

b. Are relevant to the application relevant of engineering and technology research and Innovation

c. Have not been previously published elsewhere, or, if previously published are supported by a copyright permission

d. Deals with theoretical, practical and adoptable innovations applicable to engineering and technology

e. Have a 150 to 250 words abstract, preceding the main body of the article

f. The abstract should be followed by a list of 4 to 8 "key Words"

g. Manuscript should be single-spaced under 4,000 words (approximately equivalent to 5-6 pages of A4-size paper)

h. Are supported by authentic sources, references or bibliography

Rejected/Accepted Articles

a. As a rule, articles that are not chosen for AJERI publication are not returned unless writer (s) asks for their return and are covered with adequate postage stamps. At the earliest time possible, the writer (s) is advised whether the article is rejected or accepted.

b. When an article is accepted and requires revision/modification, the details will be indicated in the return reply from the AJERI Editor, in which case such revision/modification must be completed and returned to AJERI within three months from the date of receipt from the Editorial Staff.

c. Complementary copies: Following the publishing, three successive issues are sent to the author(s)

Procedure for Submission

a. Articles for publication must be sent to AJERI on the following address:

The Editor

African Journal of Engineering Research and Innovation

P.O Box 41346- 00100

City Square Nairobi Kenya

Tel: +254 (20) 2729326, 0721 729363, (020) 2716922

E-mail: editor@iekenya.org

b. The article must bear the writer (s) name, title/designation, office/organization, nationality and complete mailing address. In addition, contributors with e-mail addresses are requested to forward the same to the Editor for faster communication.

For any queries, authors are requested to contact by mail (editor@iekenya.org).

CONTENTS